The Pennsylvania State University
The Graduate School

METAMATERIAL-BASED ACOUSTIC DEVICES FOR AUDIO AND ULTRASOUND APPLICATIONS

A Dissertation in
Acoustics
by
Jun Ji

Submitted in Partial Fulfillment
of the Requirements
for the Degree of

Doctor of Philosophy

May 2024

The dissertation of Jun Ji was reviewed and approved by the following:

Yun Jing
Professor of Acoustics
Dissertation Advisor
Chair of Committee

Victor Sparrow
United Technologies Corporation Professor of Acoustics

Benjamin Beck
Associate Research Professor of Acoustics
Deputy Director and Head, Fluid Dynamics and Acoustics Office

Xingjie Ni
Associate Professor of Electrical Engineering

Andrew Barnard
Director of the Graduate Program in Acoustics

Abstract

Acoustic Metamaterials are artificially engineered materials or structures that exhibit exotic acoustic properties that are not found in nature. They have been a highly active research area to control the behavior of acoustic waves in recent years. Acoustic metasurfaces, as the 2D version of acoustic metamaterials, have opened up unprecedented possibilities for controlling acoustic waves at will, offering a solution of molding wave propagation within a thin sheet of structures.

While the majority of the research in acoustic metamaterials and metasurfaces are curiosity-driven and have shown promising progress in overcoming the fundamental physical limitations of acoustics, there has been a scarcity of acoustic metamaterials research that can have a direct and immediate impact on real-world applications. This thesis makes contributions to the fields of acoustic metamaterials by examining the challenges of some real-world applications at audio and ultrasound frequencies and putting forward novel metamaterial-based acoustic devices that overcome these limitations.

In this thesis, we start to tackle the ultra-low frequency (below 100 Hz) sound absorption problem, which is a long-standing issue in room acoustics, by designing a low-frequency broadband, high absorption, near-omnidirectional acoustic metasurface absorber at a deep subwavelenth thickness guided by the causality limit. Then we extend the sound absorption in room acoustics to HVAC system, fundamentally from a one-port system without acoustic transmission to a two-ports system with acoustic transmission. A near-perfect absorption (99% absorption) is demonstrated when the spatial period of monopole-dipole resonators is close to one working wavelength (95% of the wavelength). The condition for perfect absorption is to render degenerate monopole-dipole resonators critically coupled. Besides absorption, loudness enhancement of acoustic transducers is another challenging issue at low audio frequency band. By leveraging the resonant coupling effect between the transducer and metamaterial resonances, a 3–7 dB broadband sound pressure level (SPL) improvement of acoustic radiation in the bass range (50–700 Hz) can be achieved.

In addition to airborne acoustics at low audio frequency, enormous underwater applications at ultrasound frequency exist. One of the application challenges along this direction is the weak ultrasound transmission through a metallic wall due to the significant impedance mismatch between water and the wall, which impedes wireless ultrasonic power transfer and data transmission in aeronautic and aerospace engineering and nuclear engineering. We design a pillar-based acoustic metamaterial for wireless and contactless ultrasonic power transfer and data transmission through a metallic wall by leveraging the pillar's vertical elongation mode.

Table of Contents

List of Figures vii

List of Tables xv

Acknowledgments xvii

Chapter 1
Introduction 1
1.1 Acoustic metamaterials 1
1.2 Acoustic metasurfaces 5
1.3 Outlines and objectives 7

Chapter 2
Broadband Acoustic Absorbing Metasurfaces in One-port Systems 10
2.1 Background and Introduction 11
2.2 Theoretical model 13
2.2.1 Description of metasurface geometry 13
2.2.2 Theoretical model for a single resonant unit cell with the embedded neck 14
2.2.3 Theoretical model for supercell with different unit cells 15
2.2.4 Causal optimality in sound absorption 16
2.3 Results and discussions 16
2.3.1 Design for 50-63 Hz (one-third octave) absorption without optimization 16
2.3.2 Design for 50-63 Hz (one-third octave) absorption with optimization 19
2.3.3 The coupling through the evanescent wave and acoustic-structure interaction 24
2.3.4 Design for 50-100 Hz (one octave) absorption with optimization . 26
2.4 Methods 30
2.4.1 Sample fabrication and experimental setup 30
2.4.2 Numerical simulations 31
2.4.3 GA optimization for 50-63 Hz (one-third octave) 32
2.4.4 GA optimization for 50-100 Hz (one octave) 33
2.5 Conclusions 33

Chapter 3
Ultra-sparse Near-perfect Sound Absorbers in Two-port Systems **35**
3.1 Background and Introduction . . . 36
3.2 Schematic and design . . . 37
3.3 Results and discussions . . . 41
3.4 Conclusions . . . 42

Chapter 4
Broadband Acoustic Radiation Enhancement Using Acoustic Metamaterial **44**
4.1 Background and Introduction . . . 45
4.2 Structure Design of CAMM . . . 47
4.2.1 Schematic of a dipole audio module . . . 47
4.2.2 Simulations . . . 49
4.3 Results and discussions . . . 52
4.3.1 Measured Radiation Enhancement induced by CAMM in free field 52
4.3.2 Measured Radiation Enhancement induced by CAMM on HATS . 57
4.4 Methods . . . 58
4.4.1 Numerical Simulations . . . 58
4.4.2 Fabrication and assembly of the audio module . . . 59
4.4.3 Measurement of SPL in free field . . . 59
4.4.4 Measurement of Thiele-Small (TS) parameters, excursion, and electrical impedance . . . 60
4.4.5 Measurement of SPL on HATS . . . 60
4.4.6 THD measurements in free field and on HATS . . . 60
4.5 Conclusions . . . 61

Chapter 5
Metamaterial-enabled Wireless and Contactless Ultrasonic Power Transfer and Data Transmission Through a Metallic Wall **64**
5.1 Background and Introduction . . . 65
5.2 Pillar-based acoustic metamaterial . . . 66
5.3 Wireless and contactless ultrasonic power transfer . . . 72
5.4 Wireless and contactless ultrasonic data transmission . . . 75
5.5 Discussions . . . 77
5.5.1 The impact of loss factor of SUS316L on the power transmission rate in simulations . . . 77
5.5.2 The impact of the number of unit cells on the power transmission rate in simulations . . . 77
5.5.3 The impact of the incident angle on the power transmission rate in simulations . . . 78
5.5.4 Power transmission enhancement through $t = 1\,\text{mm}$ SUS316L wall in air around 50 kHz . . . 79

5.5.5 The impact of the fabrication errors on the resonance frequency and power transmission rate in simulations . . . 80
5.5.6 Characteristics of the transmitter . . . 81
5.5.7 The impact of the transmitter-sample distance on the power transmission rate in simulations . . . 82
5.5.8 The measurement of transmitted pressure field . . . 82
5.5.9 Characteristics of the receiver . . . 83
5.5.10 Design of the energy harvesting circuit . . . 85
5.6 Methods . . . 87
5.6.1 Numerical Simulations . . . 87
5.6.2 Sample Fabrications . . . 87
5.6.3 Experimental Measurements . . . 87
5.7 Conclusions . . . 88

Chapter 6
Conclusions and Future Directions **89**
6.1 Research Conclusions . . . 89
6.2 Future Work . . . 90

Bibliography **92**

List of Figures

1.1 An expanded range of mass density ρ and bulk modulus (stiffness) κ can be accessed with acoustic metamaterials. The upper-right quadrant, for which ρ and κ are positive, is the realm of conventional materials and metamaterial cloaking devices. The remaining three quadrants and their boundaries correspond only to metamaterials, some of whose applications are shown. Zero-index and slow-sound materials, respectively, have vanishing ρ and κ. The lower-left quadrant illustrates some properties of superlenses and hyperlenses, both of which, as described in the text, defeat the diffraction limit. The bending of acoustic rays by those lenses is governed by a negative index of refraction, which leads to the simultaneous focusing of propagating waves (red arrows) and magnification of evanescent waves (blue curve), which together mitigate the effects of diffraction. Reprinted from "Acoustic metamaterials." by Haberman, Michael R., and Matthew D. Guild, *Physics Today* 69.6, 2016. 2

1.2 Schematic illustration of generalized Snell's law and acoustic metasurface. Using an artificially engineered interface, an abrupt phase shift along the interface is introduced. The interface is located at $z = 0$. Reprinted from "Acoustic metasurfaces." by Assouar, Badreddine, et al., *Nature Reviews Materials* 3.12, 2018. 6

2.1 (a) Schematic of a metasurface absorber with 9 supercells. (b) The explosive view of one supercell with 4 different unit cells. The thickness of the front panel, T_{front}, the thicknesses of the necks' walls, T_{neck}, and the thicknesses of partitions, $T_{\text{partition}}$, are all set as 5 mm, according to our experimental trials, to mitigate the coupling effect between neighboring air domains through the shared partitions so that the assumption of acoustically rigid boundaries in the analytical and numerical models is genuinely valid. The thickness of the back panel, T_{back}, is 2 mm. The diameter of the neck is d, the length of the neck is $l_n = (l + T_{\text{front}})$, the lateral size of a unit cell is $S(C_w \times C_l)$, the length of the cavity is l_c, and the side length of a supercell is D. (c) The photograph of the experimental set-up for measuring absorption using the two microphones method. The lateral size of the impedance tube is 20 cm $\times$20 cm. 13

2.2 (a) The theoretical (red solid line), the first type of numerical (black circles) and experimental (blue crosses) absorption coefficient at normal incidence for the non-optimized metasurface absorber. (b)-(e) The theoretical and numerical absorption coefficient for the angles of incidence 10°, 30°, 50°, and 70°. (f) The theoretical and numerical average absorption coefficient over 50-63 Hz vs. angle of incidence. 17

2.3 (a) The theoretical absorption coefficient of the non-optimized supercell (red solid line) and individual unit cells (blue diamonds, green circles, magenta points and black crosses are for unit cell 1,2,3 and 4 respectively). The curve for "unit cell N" is an absorption spectrum for a metasurface in which only unit cell N can interact with the incident sound and all the other unit cells are blocked at the front panel. N=1,2,3,4. Sound intensity maps of the non-optimized supercell at (b) 53.6Hz and (d) 57.8Hz, respectively. The bottom-left unit cell of (b) and the bottom-right unit cell of (d) are enlarged, as shown in (c) and (e), respectively. The incident pressure is normalized to 1 Pa. Color bar (W/m^2): component of the sound intensity vector that are perpendicular to the supercell surface, i.e., I_z. Arrow: components of the sound intensity vector that are parallel to the supercell surface, i.e., I_x and I_y. The size of the arrows is proportional to the magnitude of the intensity. 20

2.4 (a) The theoretical (red solid line), the first type of numerical (black circles) and experimental (blue cross) absorption coefficient at normal incidence for the optimized metasurface absorber. (b)-(e) The theoretical and numerical absorption coefficient for the angles of incidence 10°, 30°, 50°, and 70°. (f) The theoretical and numerical average absorption coefficient over 50-63 Hz vs. angle of incidence. 21

2.5 (a) The theoretical absorption coefficient of the optimized supercell (red solid line) and individual unit cells (blue diamonds, green circles, magenta points and black crosses are for unit cell 1,2,3 and 4 respectively). The curve for "unit cell N" is an absorption spectrum for a metasurface in which only unit cell N can interact with the incident sound and all the other unit cells are blocked at the front panel. N=1,2,3,4. Sound intensity maps of the optimized supercell at (b) 54.4 Hz and (e) 57.8 Hz, respectively. The bottom-left unit cell and the bottom-right unit cell of (b) are enlarged, as shown in (c) and (d), respectively. The bottom-left unit cell and the bottom-right unit cell of (e) are enlarged, as shown in (f) and (g), respectively. The incident pressure is normalized to 1 Pa. Color bar (W/m^2): component of the sound intensity vector that are perpendicular to the supercell surface, i.e., I_z. Arrow: components of the sound intensity vector that are parallel to the supercell surface, i.e., I_x and I_y. The size of the arrows is proportional to the magnitude of the intensity. 22

2.6 (a) The theoretical (red solid line), the first type of numerical (black circles), the second type of numerical (green circles) and experimental (blue cross) absorption coefficient at normal incidence. (b) The theoretical and the two types of numerical absorption coefficient for the angle of incidence 70°,. (c) The theoretical and the two types of numerical average absorption coefficient over 50-63 Hz vs. angle of incidence. (a)-(c) and (d)-(f) are for the non-optimized and the optimized metasurface absorber. 26

2.7 (a) The absorption coefficient of the optimized supercell (red solid line) and individual unit cells (blue points lines) at normal incidence. (b)-(e) The theoretical absorption coefficients for the angles of incidence 10°, 30°, 50°, and 70°. (f) The theoretical average absorption coefficient over 50-100 Hz vs. angle of incidence. 27

2.8 The absorption coefficient of the optimized supercell (red solid line) and the ideal absorber (blue solid line) at normal incidence. The optimal thickness for the optimized design is 20 cm. The optimal thickness for the ideal design is 16.9 cm when the volume porosity is set as 1 and the achieved absorption spectrum exactly matches with the desired one (85% over 50-100 Hz) in Eq. 7. 30

3.1 (a) 3D schematic of an ultra-sparse near-perfect absorber array. (b) Cross-sectional geometry of each unit cell of the array, which is composed of a Helmholtz Resonator as a monopole resonator and a space-coiled open-open tube as a dipole resonator. The vertical dash-dotted line in gray is the plane of mirror symmetry. 37

3.2 (a) Numerical absorption coefficient as a function of geometry modulation Δl_{n} and Δw_{n} for monopole (left) and dipole (right) resonators when the other resonator is closed. (b) Numerical absorption coefficient of the optimal design (marked as black stars in (a)) in frequency domain when both monopole and dipole (black curve), only monopole (blue curve), and only dipole (red curve) resonator is functional. (c) Numerically computed distributions of acoustic pressure (color) and acoustic intensity (arrow) at 3000 Hz in a unit cell with Floquet periodic boundary condition along y direction, when both monopole and dipole (top), only monopole (middle), and only dipole (bottom) resonator is functional. Magnitude of acoustic intensity is proportional to the size of arrow. 38

3.3 Numerical eigenfrequency and loss ratio as a function of geometry modulation (a) $\Delta l_{\mathrm{n(m)}}$, (b) $\Delta w_{\mathrm{n(m)}}$, (c) $\Delta l_{\mathrm{n(d)}}$, and (d) $\Delta w_{\mathrm{n(d)}}$. (e) Absorption coefficient of the optimal design in 2D numerical simulation, 3D numerical simulation and the couple mode theory. (f) 3D numerically computed distributions of acoustic pressure (color) and acoustic intensity (arrow) at 3000 Hz, when our designed absorber is extended 3.5 cm along z direction and put inside a 3D unit cell with Floquet periodic boundary condition along y direction. Magnitude of acoustic intensity is proportional to the size of arrow. 39

3.4 Absorption coefficient as a function of frequency and the angle of incidence in 2D numerical simulations. 42

4.1 (a) A dipole audio module on a HMD (a VR device called Quest 2). (b) 3D, (c) 2D schematics of the dipole audio module with CAMM, (d) The normalized pressure distribution of the dipole configuration outside the audio module on the plane z =0. 47

4.2 (a) Block diagram of the audio module, only the front port with CAMM is included. (b) Numerical voltage sensitivity of the audio module, when coupled resonances, which are induced by CAMM at different partition distances d, are introduced into an empty waveguide with a thickness of $T = 5.0$ mm. (c) The improvement of voltage sensitivity compared with the empty waveguide at $T = 5.0$ mm. 49

4.3 Numerical results of the dipole response for WG50 (black), CAMM50_4mm (red), and CAMM50 (green). The voltage sensitivity at three locations: (a) at a distance of 0.5 cm from the front port, (b) at a distance of 0.5 cm from the rear port and, (c) LP. (d) shows the pressure phase difference between the front port and rear port. 54

4.4 Photograph of measuring (a) voltage sensitivity and (b) excursion and electrical impedance of the audio module in free field under 0.1 Vrms. Measurements (dash lines) and simulations (solid lines) of (c) voltage sensitivity at LP, (d) excursion at the center of the speaker diaphragm, (e) the real part of the electrical impedance, and (f) power sensitivity per 0.1 W at LP for WG50 (black) and CAMM50 (green). 55

4.5 (Caption on the next page.) 56

4.5 (a) Schematic of measuring the voltage sensitivity on HATS when (b) WG50/CAMM50 is mounted on the left/right ear under 0.1 Vrms excitation voltage. Measured digital signals for the voltage sensitivity using in-ear microphone when (c) male voice signals and (f) a music signal are played by WG50 (black) and CAMM50 (green). Improvement of the voltage sensitivity compared with WG50 for the male voice signals and the music signal are plotted in the figures right below the voltage sensitivity. For the male voice signals, the spectrogram of WG50 and CAMM50 are shown in (d) and (e) from 50 Hz to 2000 Hz using the same colormap (-140 dB to -97 dB). A close-up view with another colormap range (-130 dB to -107 dB) is plotted for WG50 and CAMM50 right below to show the enhancement from 50 Hz to 200 Hz. For the music signal, the spectrogram of WG50 and CAMM50 are shown in (g) and (h) from 50 Hz to 2000 Hz using the same colormap (-170 dB to -125 dB). A close-up view with another colormap range (-150 dB to -125 dB) is plotted for WG50 and CAMM50 right below to show the enhancement from 50 Hz to 200 Hz.For the music signal, the spectrogram of WG50 and CAMM50 are shown in (g) and (h) from 50 Hz to 2000 Hz using the same colormap (-170 dB to -125 dB). A close-up view with another colormap range (-150 dB to -125 dB) is plotted for WG50 and CAMM50 right below to show the enhancement from 50 Hz to 200 Hz. 57

4.6 Measured (a) SPL and (b) THD for WG50 and CAMM50 in free field. (c) SPL and (d) THD improvement for CAMM50 compared with WG50. 62

4.7 Measured (a) SPL and (b) THD for WG50 and CAMM50 on HATS. (c) SPL and (d) THD improvement for CAMM50 compared with WG50. . . 63

5.1 Schematic of the through-metal-wall WC-UPT and WC-UDT system enabled by the pillar-based acoustic metamaterial. A close-up view of the metamaterial is displayed in the bottom-left corner. The displacement field of the metamaterial at VEM is shown in the top-right corner, which is the mechanism used to enhance the ultrasonic power transmission rate through the metallic wall. 67

5.2 Design of the pillar-based metamaterial for the through-metal-wall WC-UPT and WC-UDT. (a) Schematic of a periodically arranged unit cell under a incident plane wave and the first irreducible Brillouin zone. (b) The complex band structure. The real eigenfrequency is plotted on y axis and the imaginary eigenfrequency is represented by the gray scale. The green ellipse encompasses three propagating modes corresponding to δ, γ_1, and γ_2. The distribution of the normalized displacement magnitude |u| for these modes is depicted by the color scale. The red dash line is the sound line. (c) Power transmission rate for different number of unit cells under a normally incident plane wave. (d) Power transmission rate as a function of the incident angle of θ when $\phi = 0$. 68

5.3 (a) and (b) show the schematic and photo of the experimental setup. (c) and (d) show the fabricated plate with AMMs. (e) The on-axis pressure magnitude distribution has multiple local extremes in the near field of the piston transmitter. (f) Comparison of simulated and measured power transmission rate. 70

5.4 The transmitted pressure field from numerical simulations (at 460 kHz) and experimental measurements (at 442 kHz) demonstrates the transmission enhancement enabled by AMM. (a) Simulated and (b) measured pressure field in x-y plane at $z = 45$ mm. (c) Simulated and (d) measured pressure field in x-z plane at $y = 0$ mm. The center of the transmitter surface is set as the origin of the coordinate. For each sub-figure, the pressure magnitude is normalized by the maximum value in the case of "No Plate". 73

5.5 Experimental results of wireless and contactless ultrasonic power transfer through a metallic wall using the pillar-based metamaterial. (a)Schematic and photo of experimental setups. The enhanced ultrasonic transmission is collected by a receiver to charge capacitors. (b) The measured output signals of the receiver under an excitation of 445 kHz continuous-mode ultrasound for four different configurations: an input voltage of 4.4 Vpp on the transmitter for (i) "No Plate", (ii) "Plate w/ AMM", and (iii) "Plate w/o AMM", as well as (iv) an input voltage of 20 Vpp on the transmitter for"Plate w/o AMM". (c) The charging time dependence of voltage on a 220 µF capacitor for the four configurations. (d) Comparison of the charged voltage and average charging power. (e) Photo showing that a commercial LED lit up in the configuration (ii). 74

5.6 Experimental results of wireless and contactless ultrasonic data transmission of a binary image of "PSU". (a) The transmission of binary data using ASK modulation: (i) a 15-bits binary signal embedded within the start bits (100) and the stop bits (001), (ii) the binary signal is transformed into digital signal before being transmitted through a PZT transducer, in which each bit is represented by 5 cycles of sine waves at 445 kHz, (iii) the received time-domain digital signal for "Plate w/ AMM", and (iv) the received time-domain digital signal for "Plate w/o AMM". For (ii) - (iv), left axis is the digital voltage and right axis is the digital power. (b) The original image composed of 15×36 pixels is encoded into binary signals of "0" and "1". (c) The transmitted digital image. (d) The received digital image for "Plate w/ AMM". (e) The received digital image for "Plate w/o AMM". The digital power in (c)-(e) is normalized by their respective maximum digital power. The signals in the 15th column (highlighted by blue blocks) of images in (b)-(e) are shown in (a). 76

5.7 The power transmission rate as a function of SUS316L loss factor in COMSOL. 77

5.8 The pressure distribution at the power transmission peak frequency 460 kHz for (a) 6×6, (b) 10×10, and (c) 20×20 unit cells. The middle part without the pressure distribution is the plate region simulated with "Solid Mechanics" module. 78

5.9 The distribution of (a) the background pressure and (b) the scattered pressure when the excitation frequency is 460 kHz and $\theta = 60°$. 79

5.10 Design of the double-sided pillar-based metamaterial for the power transmission enhancement through a 1 mm metal plate in air at 50 kHz. (a) Schematic of a periodically arranged unit cell under a incident plane wave and the first irreducible Brillouin zone. (b) Band structure. (c) Power transmission rate for the plate w/ and w/O AMM under a normally incident plane wave. (d) The typical loss factor of SUS316L significantly affects the power transmission rate. 80

5.11 Impact of fabrication errors on the resonance frequency of a pillar and its power transmission rate. (Top) (a) Symmetric and (b) asymmetric shapes. (c) Resonance frequency and power transmission rate (at 458 kHz) affected by degree of asymmetry. (Bottom) (d) Isometric and (e) cross-sectional views. (f) Resonance frequency and power transmission rate bars at resonance frequencies dependent on tolerance parameters, h and w, of the cone shape, respectively. 81

5.12 (a) The power transmission rate when the plate is placed at the minimal/-maximal pressure location in the near field of the transmitter ($d_{\mathrm{tm}} = 9.1$ mm/ 14 mm). (b) The pressure distribution for "Plate w/ AMM" at 460 kHz 83

5.13 The measured emitting and received signals in the time domain (left column) and frequency domain (right column) for three cases: (a) "No plate", (b) "Plate w/ AMM", and (c) "Plate w/o AMM". For time signals, the top panel displays two periods of the burst and the bottom panel displays the zoomed-in signals. 84

5.14 (a) The measured impedance of the receiver. (b) The output voltage and power from the receiver to a series-connected resistive load, respectively, showing an optimal output power at $325\,\Omega$. 85

5.15 Schematic diagram for the energy harvesting circuit. 86

5.16 The traces of the circuit on (a) the top layer and (b) the bottom layer of the PCB. (c) 3D rendering and (d) the photo of the PCB. 86

List of Tables

2.1 Geometric parameters of the metasurface absorber with 4 different unit cells without optimization. The lateral size of the supercell is 20 cm × 20 cm. The overall thickness of the absorber is 19 cm. Its volume porosity is 80%. 17

2.2 Geometric parameters of the optimized metasurface absorber composed of 4 different unit cells. The lateral size of the supercell is 20 cm×20 cm. The overall thickness of the absorber is 15.40 cm. Its volume porosity is 84%. 21

2.3 Comparison of the absorption performance between the non-optimized (design A) and the optimized (design B) absorber. "Theory" and "Simulation" refer to the average absorption coefficients over 50-63 Hz based on the analytical model and the first type of numerical result, while "Experiment" refers to the average absorption coefficient over 48-61 Hz based on the experimental result. ϕ_V and T are the volume porosity and total thickness of the design. $T_{\min}$ is the minimum thickness dictated by the principle of causality (i.e., (**Eq. 2.7**)). 23

2.4 The coupling effects that each model takes into account. By comparing the corresponding curves in **Figure 2.6**, the evanescent wave coupling and the acoustic-structure interaction can be separately evaluated for the validation of the assumptions that are made in the chapter 2.2.3. 26

2.5 Geometric parameters of an optimized metasurface absorber composed of 19 different unit cells. The lateral size of the supercell is 78.84 cm × 78.84 cm. The overall thickness of the absorber is 20 cm. Its volume porosity is 90%. 28

3.1 The geometric parameters of our design in **Figure 3.1**(b). The unit is in mm. 39

4.1 TS parameters of the moving-coil transducer from Klippel LPM measurements 48

Acknowledgments

Foremost, I am very grateful to Dr. Yun Jing for entrusting me with this opportunity and constantly guiding me through all the projects that I pursued. I've come a long way since I first met him in 2016 when I was an undergraduate student. I really appreciate the large amount of time he has spent guiding me to learn how to identify the imminent problem in the research that needs to be solved, how to tackle technical details, and how to build efficient communication skills.

I would like to express my sincere appreciation to National Institutes of Health (NIH), National Science Foundation CMMI Award (Nos. 1951221, and 1951106), National Natural Science Foundation of China under Grant No. 11704284, Meta Platforms, Inc, the Penn State Startup funds for Dr. Yun Jing, and the Program of Acoustics at Penn State, for financially supporting me through my graduate studies and facilitating an experience that sat at the intersection of academia and industry. The findings and conclusions do not necessarily reflect the view of the funding agency. Also to the members of my dissertation committee, Dr. Victor Sparrow, Dr. Benjamin Beck and Dr. Xingjie Ni, for their valuable time and helpful insights on my research. Also to the members in the the Program of Acoustics, Dr. Andrew Barnard, Dr. Daniel Russell, Dr. Julianna Simon, Dr. Stephen Thompson, Dr. Thomas Gabrielson for their valuable teaching and helpful insights on the broader field of acoustics.

Special thanks are given to various SIMBA lab-mates who helped me a lot. Dr. Mourad Oudich patiently walked beside me on my projects and addressed technical problems about elastic metamaterials; Dr. Yuanchen Deng and Dr. Nikhil Gerard who helped me not only on research but also on life and I will never forget the moment we spent together as simple as a after-lunch coffee chat. I would also thank other lab members - Dr. Tarry (Chen) Shen, Dr. Ni Sui, Dr. Juanjuan Gu, Dr. Jiaxin Zhong, Dr. Hyeonu Heo, Mr. Hyungjoo Park, Miss Yutong Wang, Mr. Jeff Bell, Miss Kama Bell, and Mr. Mattew Olmstead for all our insightful discussions and for the candid friendship that we share.

Over the course of my PhD, I have been blessed to have the opportunity to work with the individuals who pioneered my present field of study. I'm extremely grateful to them for their time and efforts. I would like to acknowledge Dr. Yong Li, Dr. Steven Cummer, Dr. Junfei Li, Dr. Xiang Yan, Dr. Fuh-Gwo Yuan, Dr. Xiuyuan Peng, Dr. Xiaoxing Xia, Dr. Yong Zhu, Mr. Dongting Li, and all Metamates including Dr. Chuming Zhao, Mr. Frank Yao, Dr. Tetsuro Oishi, Mr. John Stewart, Mr. Ulrik Skov, Dr. Limin Zhou, and Mr. Rex Price.

Lastly, but most importantly, I would like to express my heartfelt thankfulness to my parents and my girlfriend Chang Yan, for their unconditional love and support.

Chapter 1
Introduction

Acoustics is the branch of science that studies the propagation of sound and vibrational waves. Audible acoustic waves are ubiquitous in our everyday experience: they form the basis of verbal human communication, and the combination of pitch and rhythm transforms sound vibrations into music. Waves with frequencies beyond the limit of human audibility are used in many ultrasonic imaging devices for medicine and industry. However, acoustic waves are not always easy to control. Audible sound waves spread with modest attenuation through air and are often able to penetrate thick barriers with ease. Electronic devices are able to amplify and manipulate sound signals, but only after they are converted to electronic form. New tools to control these waves as they propagate, in the form of new artificial materials, are extremely desirable [1].

While the quest for such tools has always existed, our yearning for them was revived in the 1990s, with developments in the fields of photonic and phononic crystals [2, 3]. Initially inspired by an analogy with the quantum mechanical band theory of solids in which electronic waves interact with a periodically arranged atomic lattice to form energy bands separated by bandgaps, photonic and phononic crystals were proposed theoretically [4, 5] and realized experimentally [6, 7]. To be effective, the lattice constants of photonic and phononic crystals have to be on the order of the relevant electromagnetic and elastic/acoustic wavelength. Owing to the large wavelength of acoustic waves in the audible regime ranging from centimeters to meters, phononic crystals were mostly realized in the ultrasonic regime, because lower frequencies would require rather bulky samples.

1.1 Acoustic metamaterials

The emergence of acoustic metamaterials not only resolved the sample size problem but also introduced new functionalities not found previously [8]. The term “metamaterials”

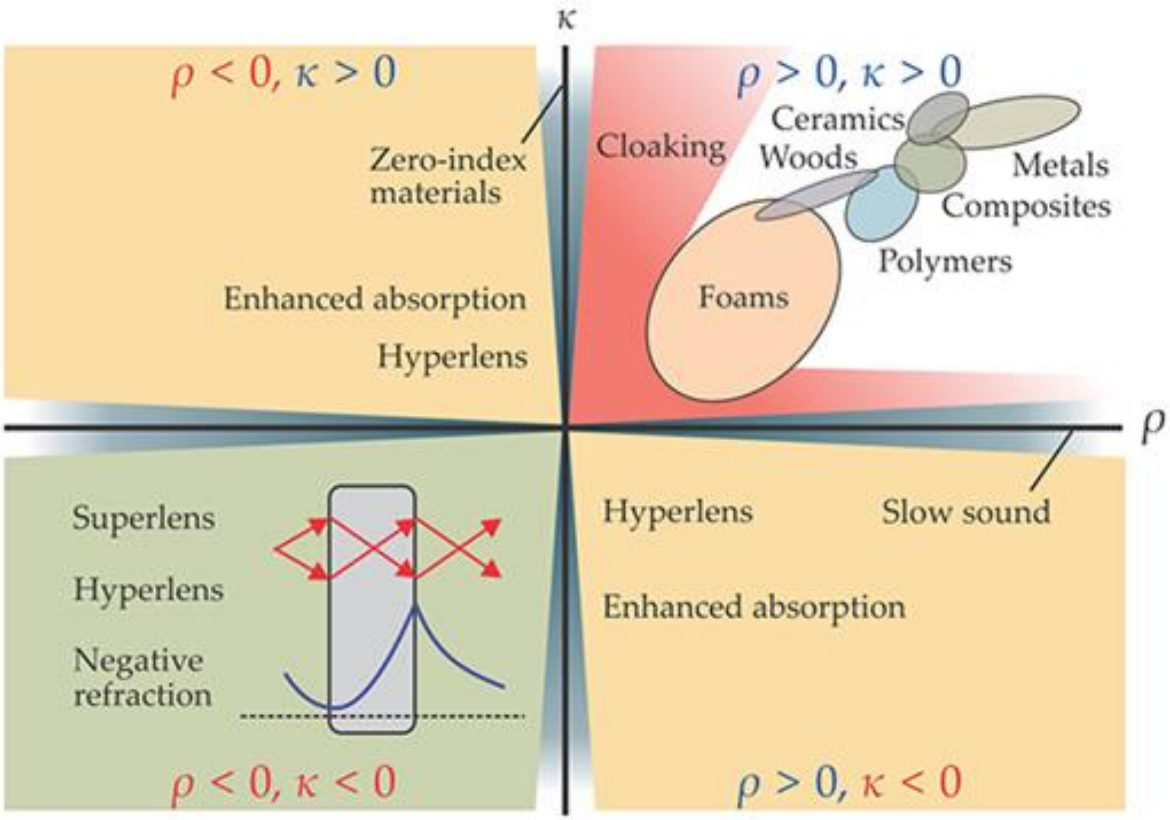

Figure 1.1. An expanded range of mass density ρ and bulk modulus (stiffness) κ can be accessed with acoustic metamaterials. The upper-right quadrant, for which ρ and κ are positive, is the realm of conventional materials and metamaterial cloaking devices. The remaining three quadrants and their boundaries correspond only to metamaterials, some of whose applications are shown. Zero-index and slow-sound materials, respectively, have vanishing ρ and κ. The lower-left quadrant illustrates some properties of superlenses and hyperlenses, both of which, as described in the text, defeat the diffraction limit. The bending of acoustic rays by those lenses is governed by a negative index of refraction, which leads to the simultaneous focusing of propagating waves (red arrows) and magnification of evanescent waves (blue curve), which together mitigate the effects of diffraction. Reprinted from "Acoustic metamaterials." by Haberman, Michael R., and Matthew D. Guild, *Physics Today* 69.6, 2016.

was originally coined to denote a class of structured composites whose wave functionalities arise as the collective manifestations of its locally resonant constituent units. Because the resonant frequency of a unit depends only on its inertia (for example, the mass) and the stiffness (for example, that of the spring), the relevant wavelength at the resonant frequency can be orders of magnitude larger than the physical dimension of the resonant unit. This subwavelength characteristic is therefore a common feature of all types of metamaterials, whose definition has now broadened to include subwavelength structures with functionalities not found in nature.

Extended from electromagnetic metamaterials [9, 10], the researches in the field of acoustic metamaterials began in 2000 [11]. After that, the exploration of acoustic metamaterials with negative density and negative bulk modulus becomes a hot topic [12, 13, 14]. Other topics explored at the same time in the fields also include acoustic cloak [15, 16], acoustic superlens and superlens [17, 18], etc. All the acoustic metamaterials mentioned before could be summarized in **Figure 1.1** [19]. In acoustics, the propagation of sound waves is governed by two equations, the mass conservation law and the momentum law. When both material compressibility and density are positive, the refraction index is also positive. When a beam of sound wave incident from air to this medium, the incident beam and the refracted beam will lie on both sides of the normal line. When one of compressibility and density is negative while the other keeps positive, given by the square root in the expression of sound speed, the material is called single-negative with its sound speed being imaginary, and hence, sound waves cannot travel inside this media. When both compressibility and density are negative, the material is called double-negative and the refraction index becomes negative, resulting in the negative refraction. In this case, for a sound beam coming from air into this media, the incident beam and the refracted beam will lie on the same side of the normal line. Double-negative acoustic metamaterials enable significantly improved refractive properties through negative refraction. They permit us to construct superlenses that amplify evanescent waves and provide subwavelength resolution for acoustic imaging devices. Double-negative materials can also be fabricated into hyperlenses, which use a hyperbolic dispersion relation between frequency and wavenumber, rather than the elliptical dispersion found in traditional anisotropic materials, to produce negative group velocity and a negative index of refraction.

Although metamaterials have helped to advance acoustics technology in the past decade, researchers have mostly relied on linear, passive and static meta-atoms, as described in the previous paragraphs. However, these properties limit the applicability of metamaterials and their general impact on technology. Passivity, linearity and time-invariance impose fundamental bounds on the available choices of acoustic parameters. For example, the frequency dispersion of passive linear acoustic materials is bound by Kramers–Kronig-like dispersion relations [20], which ultimately limit the bandwidth over which certain long-sought properties of metamaterials are available and, therefore, the spectrum of operation of some metamaterial devices. This is especially true when resonant and, hence, frequency-dependent inclusions are considered, as in many of the examples discussed in the previous paragraphs, in which case passivity imposes a bound

on the bandwidth of operation that scales with the size of the inclusions.

For all these reasons, there has been a growing effort to explore active acoustic metamaterials, which could potentially overcome the challenges described above and increase their effectiveness in relevant applications. Active unit cells for metamaterials with unusual acoustic properties have been considered in several designs. The term 'active' is used quite generally to indicate inclusions that can provide energy to the impinging wave and feedback to the acoustic system, that can be controlled or that are externally biased. The most common elements used in active meta-atoms are active transducers, micro- or nano-electromechanical systems, piezoelectric materials and electrically loaded acoustic elements. Piezoelectric materials provide an ideal platform to tune and control the acoustic properties of a metamaterial in a compact way, because they respond strongly to electrical signals and can be controlled with relatively simple electronics [21]. Piezoelectric effects may also be exploited in semiconductor substrates [22], and these materials may be used to provide effective acoustic gain to amplify the acoustic wave as it propagates through them. A similar route to acoustic gain and active control of the acoustic properties of a metamaterial may be provided by loading loudspeakers, which, similar to piezoelectrics, convert airborne acoustic waves into electric signals and vice versa, using electronic circuitry. These strategies have been successfully used, for instance, to obtain controllable acoustic gain and loss in a lumped element configuration [23].

One particularly interesting subclass of active metamaterials is a pair of balanced active elements and dissipating elements. Such a combination of elements has been shown to provide unusual acoustic responses. This field of research has stemmed from theoretical research in the area of quantum mechanics, where it was shown that a special class of Hamiltonians that commute with the parity–time (PT) operator can support real energy eigenvalues even though they are non-Hermitian [24]. Extended from the theoretical discovery to classical wave systems, PT-symmetric optical metamaterials was then shown to support lossless propagation and loss compensation, unidirectional invisibility and threshold-free lasing, among other things. Recently, PT symmetry has become relevant to the field of acoustic metamaterials, in which gain and active components are much more readily available than they are in optics. PT-symmetric acoustic metamaterials have been a basis for novel acoustic devices, including new cloaks for sound with highly asymmetric scattering responses [25] and advanced sensors with minimal scattering [23].

Another area of research in the field of active acoustic metamaterials is that of non-reciprocal metamaterials, in which the reciprocity is broken so that one-way propagation and isolation are allowed. Several non-reciprocal metamaterial devices providing

large isolation levels have been proposed that exploit greatly enhanced Doppler effects in resonators loaded with a spinning fluid [26] and suitable forms of spatiotemporal modulation in coupled resonating cavities [27]. Nonlinearities [28] also provide a route to isolation and non-reciprocal transmission. A basic scheme involves asymmetric frequency conversion and suitable filtering, which may be achieved in its simplest form by combining a nonlinear medium with a frequency-selective structure (e.g., mirror and lattice) [29].

1.2 Acoustic metasurfaces

Although acoustic metamaterials provide unprecedented ways of wave manipulation, the realization typically requires intricate fabrication, and the devices are subjected to strong thermoviscous losses. High-frequency signals are commonly dampened even in natural materials, and as sound propagates in metamaterials, especially in volumetric samples with thicknesses of multiple wavelengths, the energy is partially, and often largely, dissipated. This problem is especially relevant in the case of resonant inclusions. The quest to manipulate waves using the smallest possible amount of space and engineered materials has led to the exploration of acoustic metasurfaces starting from 2010s.

In contrast to the volumetric modulation using metamaterials, acoustic metasurfaces [30], a 2D verison of acoustic metamaterials composed of subwavelength cells, provide non-trivial local phase shifts to the waves that transmit through or reflect from them within a planar or nearly flat geometry at a thicknesses much smaller than the wavelength. Similar to acoustic metamaterials, this idea is also first introduced in electromagnetic waves [31]. Extraordinary functionalities demonstrated by acoustic metasurfaces include efficient wavefront modulation [32, 33], deep sub-wavelength focusing [34], negative refraction [35], asymmetric sound transmission/reflection [36, 37], and ultra-thin absorbers [38, 39, 40].

The general concept of metasurfaces was initiated and introduced by the use of generalized Snell's law that governs wave propagation at the interface of two homogenous media [31]. Snell's law can be extended theoretically to define the phase at the interface to achieve desired sound wave reflection or refraction. Such control on sound waves can be achieved by introducing abrupt phase shifts in the acoustic path by incorporating periodic structures on a planar interface on subwavelength scales. **Figure 1.2** illustrates an acoustic plane wave incident on an artificially engineered interface which introduces an additional phase shift to the acoustic waves transmitted or reflected from the interface. Considering that the interface is located in the plane of z= 0, then it creates a phase

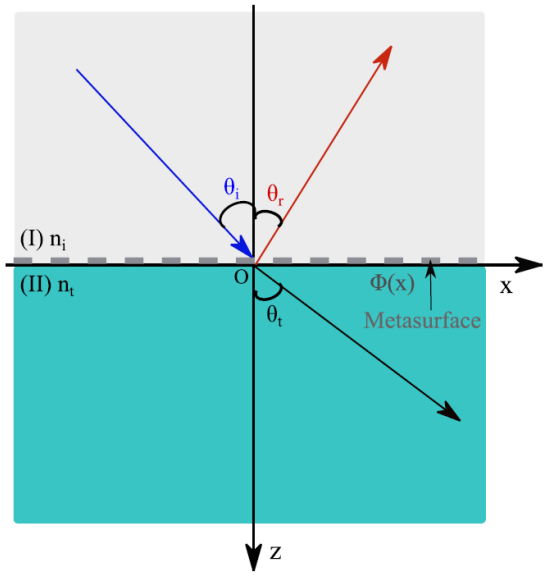

Figure 1.2. Schematic illustration of generalized Snell's law and acoustic metasurface. Using an artificially engineered interface, an abrupt phase shift along the interface is introduced. The interface is located at $z = 0$. Reprinted from "Acoustic metasurfaces." by Assouar, Badreddine, et al., *Nature Reviews Materials* 3.12, 2018.

discontinuity as $\phi(x)$. A detailed explanation is given in Ref. [30]. Governed by the generalized Snell's law of reflection, the relationship between the angle of incidence, θ_i and angle of reflection, θ_r can be expressed as

$$\sin\theta_{\mathrm{r}} - \sin\theta_{\mathrm{i}} = \frac{\lambda_1}{2\pi}\frac{\mathrm{d}\phi(x)}{\mathrm{d}x}, \tag{1.1}$$

The major building blocks of acoustic metasurface include space-coiled structure [32], array of the Helmholtz resonators [41], and membrane type structure [38]. When discussing acoustic wave manipulation, two important parameters should be considered, one is the phase for tailored wavefront and the other is the amplitude of the reflected or transmitted waves. The phase of the reflected waves can be tuned by a space-coiled structure. Such structures elongate the effective propagating path along with the coiling structure which is longer than the geometrical dimensions of the structure. The key benefit of the coiling up structure is that it can control the refractive index of the acoustic metasurface by controlling the path length to various degrees as per the requirement. Because of the longer path length, reflected waves can be modulated and the reflected phase shift can be tailored within the entire 0–2π range. The coiling path, however, is normally associated with excessive thermoviscous losses. To achieve a high refractive index and high transmission at the same time, a metasurface structure was proposed

using an array of four HRs and a connecting pipe connected at the open side of the HRs [33]. Here, the series of HRs contributes to cover a full range of phase 0-2π and the connected pipe contributes to achieving hybrid resonance that compensates the impedance mismatch with the surrounding medium. Using a straight pipe with the length of $\lambda/2$, effective impedance matching was obtained, which is based on Fabry-Parrot resonance. The resulting metasurface had a tunable phase velocity and a transmission efficiency that is close to unity with a deep-subwavelength width of the structure.

1.3 Outlines and objectives

Recent developments in acoustic metamaterials research(including phononic crystals and acoustic metasurfaces) have shown promising progress in overcoming the fundamental physical limitations of acoustics. While the majority of this research is curiosity-driven and focused on fundamental physics, there has been a scarcity of acoustic metamaterials research that can have a direct and immediate impact on real-world applications. In this thesis, metamaterial-based acoustic devices are put forward for various applications at audio and ultrasound frequencies such as noise control via sound absorption in room acoustics and HVAC systems, bass loudness enhancement of electrodynamics transducers in AV/VR devices, and wireless and contactless ultrasound power transfer and data transmission through a metallic wall. The contributions to this field are summarized as below:

- In chapter 2, we report on an analytical, numerical and experimental study of a low-frequency broadband (50–63 Hz, one third octave band), high absorption (average absorption coefficient 93%), near-omnidirectional (0–75°) acoustic metasurface absorber composed of four coupled unit cells at a thickness of 15.4 cm (1/45 of the wavelength at 50 Hz). To further broaden the bandwidth (50–100 Hz, one octave band), a design with 19 unit cells coupled in a supercell is analytically studied to achieve an average absorption coefficient of 85% for a wide angle range (0–75°) at a thickness of 20 cm (1/34 of wavelength at 50 Hz). The genetic optimization algorithm is used to reach a causally optimal design. The proposed design methodology may solve the long-standing issue for low frequency absorption in room acoustics.

- In chapter 3, we designed a near-perfect acoustic absorber (99% absorption) composed of monopole-dipole resonators with its spatial period being close to one

working wavelength (95% of the wavelength). The condition for perfect absorption is to render degenerate monopole-dipole resonators critically coupled. Frequency domain simulations, eigenfrequency simulations, and the coupled mode theory are utilized to demonstrate the acoustic performances and the underlying physics. The sparse-resonator-based sound absorber could greatly benefit noise control with air flow and this study could also have implications for electromagnetic wave absorbers.

- In chapter 4, we designed an acoustic metamaterial inside a head-mounted audio module to achieve a 3–7 dB broadband sound pressure level (SPL) improvement in the bass range (50–700 Hz), which is the most challenging frequency range for radiation enhancement. The adoption of the acoustic metamaterial not only enhances voltage sensitivity near the intrinsic metamaterial resonance frequency, but also extends the broadband enhancement to a lower transducer resonance frequency by carefully engineering the metamaterial-transducer resonant coupling. The improvement of the audio module is demonstrated through fully coupled electrical-mechanical-acoustical numerical simulations using finite element analysis, which are validated against comprehensive measurements including electrical impedance analysis, speaker diaphragm displacement analysis, voltage sensitivity and power sensitivity analysis, and spectrogram. This study not only offers a promising path to improve the audio module quality without increasing the size, but also represents an important milestone toward using acoustic metamaterial research to solve audio industry challenges

- In chapter 5, we designed a pillar-based acoustic metamaterial for wireless and contactless ultrasonic power transfer and data transmission through a metallic wall by leveraging the pillar's vertical elongation mode. Experiments conducted in water demonstrate a 33-fold power transmission enhancement (from 2% to around 66%) at approximately 450 kHz through a 1 mm thick metallic wall. Furthermore, our experiments show that a commercial light-emitting diode can be illuminated by harvesting the metamaterial-enhanced transmission of ultrasonic energy, which would not have been possible with the metallic wall alone even at an input voltage approximately five times greater. In addition, data transmission through the metallic wall is demonstrated by employing amplitude shift keying modulation to transmit an image, showcasing the remarkable improvement in image quality enabled by the metamaterial. This study paves the way for a future generation of wireless and contactless ultrasonic power transfer and data

transmission applications.

Chapter 2
Broadband Acoustic Absorbing Metasurfaces in One-port Systems

This chapter presents the study that was published in

- Ji, Jun, et al. "Low-frequency broadband acoustic metasurface absorbing panels." Frontiers in Mechanical Engineering 6 (2020): 586249.

Some minor changes have been made to the text to better organize this work into the thesis. Furthermore, some figures have been rearranged and rescaled to match the single-column format of the thesis.

2.1 Background and Introduction

A sound absorber with a broadband and high absorption at a deep-subwavelength scale is of great interest in many occasions, such as room acoustics [42], automobiles and aerospace engineering [43]. A particular interest is to realize the so-called modal equalization (i.e., absorbing the normal mode frequencies of a room which usually fall below 100Hz) [44, 45, 46, 47] for improving sound generation and speech interpretation. However, this is hindered by the inability of conventional sound absorbing materials to effectively remove low frequency sound [48].

The emergence of acoustic metamaterials [8, 49] and acoustic metasurfaces [30, 50] has enabled novel methods to design acoustic functional devices and has facilitated the development of new sound absorbing structures. To achieve the deep-subwavelength scale, one strategy is to use a very thin decorated membrane [51, 40]. In such a design, however, a uniform and controlled tension of the membranes is needed, which leads to fabrication challenges and durability issues. Another strategy is to modify the geometry of the conventional Helmholtz resonator (HR) and the microperforated panel (MPP) [52] into space-coiling structures [53, 54, 55], embedded-neck structures [56, 57] or multi-coiled structures [58]. Under the condition of impedance match or critical coupling [59, 60], these designs can achieve a perfect sound absorption. Both the strategies above, however, have relatively narrow absorption bandwidth, which inevitably hinders practical applications. Some designs improve the bandwidth of single/identical resonator by tailoring the damping, such as increasing the intrinsic material damping [61] or utilizing a heavily overdamped condition [62]. Such designs, however, are either impractical or can hardly be applied to airborne sound absorption without a sacrifice of thickness [60].

To maximize the bandwidth of acoustic absorbers, a combination of different resonators [63, 64, 65, 66, 67, 68, 69, 70, 71, 72] has been proposed as an effective design strategy. However, their corresponding thicknesses along the propagating direction are either thick or left with a potential for improvement. It is thus reasonable to ask: How much potential is there left for improvement? Or, for a target absorption spectrum, what is the minimum sample thickness required? These questions were addressed recently by [39] in which a target absorption is attained with the minimum sample thickness as dictated by the law of causality. However, the sponge, which is not desired in harsh environment, is needed to achieve a causally optimal design for a broadband design, by remediating the negative absorption effects resulting from using a small, finite number of resonators. In addition, the examples demonstrated in that study pertain to broadband absorption at mid to

high frequency ranges. To design a causally optimal sound absorber which can achieve a broadband, near-omnidirectional high absorption at extremely low frequencies is still a largely unsolved issue. Though this issue was partially addressed by [58], the design therein was neither broadband nor demonstrated to be causally optimal.

To address the foregoing issues, this study provides a framework to design a metasurface sound absorbing panel which is composed of non-uniform unit cells with different embedded necks in a supercell. In the design procedure, three degrees of freedom (DOFs), which are the lateral size of the unit cells, the number of unit cells and the lateral size of the supercell, are crucial factors to provide a broad range of surface impedance for a target absorption spectrum. Constrained by a desired absorption spectrum, a supercell at a minimum thickness is designed with the aid of optimization based on the Genetic algorithm (GA). Besides, the roles of different couplings (the interference coupling in the far field, the evanescent wave coupling, and the acoustic-structure interaction) on the absorption are separately evaluated.

The study is structured as follows: In section 2.2, the metasurface geometry and the corresponding theoretical model are presented, along with the causal optimality recently introduced to sound absorption. In section 2.3.1, a design with a validation of simulation and experimental results is presented. To form the desired absorption spectrum over 50-63 Hz, a fairly weak coupling between unit cell is assumed and each unit cell is thus designed independently [63, 73] to have a perfect absorption (an impedance-matching condition) at its specified resonant frequency. At each peak of the absorption spectrum, the absorption is solely contributed from one resonator. Section 2.3.2 presents a design where the lateral sizes of unit cells are demonstrated to be instrumental to reducing the thickness by means of GA-based optimization. The thickness of the optimized structure is reduced by 23% without sacrificing the absorption performance. At the two center peaks of the absorption spectrum, the strong coupling, in which more than one resonator is excited, is observed. This leads to a new avenue to designing a deep-subwavelength sound absorber. The strong coupling is briefly explained as the far field coupling [74] with the Hamiltonian from the coupled-mode theory [75, 76]. In section 2.3.3, the evanescent wave coupling and the acoustic-structure interaction are separately evaluated for the validation of the assumptions made in section 2.2 In section 2.3.4, a judicious tuning of a supercell's lateral size and the number of unit cells in a supercell, combined with the careful design of the lateral sizes of unit cells, is demonstrated to jointly facilitate a causally optimal [39] absorber covering 50-100 Hz. The causally optimal absorber is further compared with an ideal absorber at an ideally minimum thickness. Section 2.5

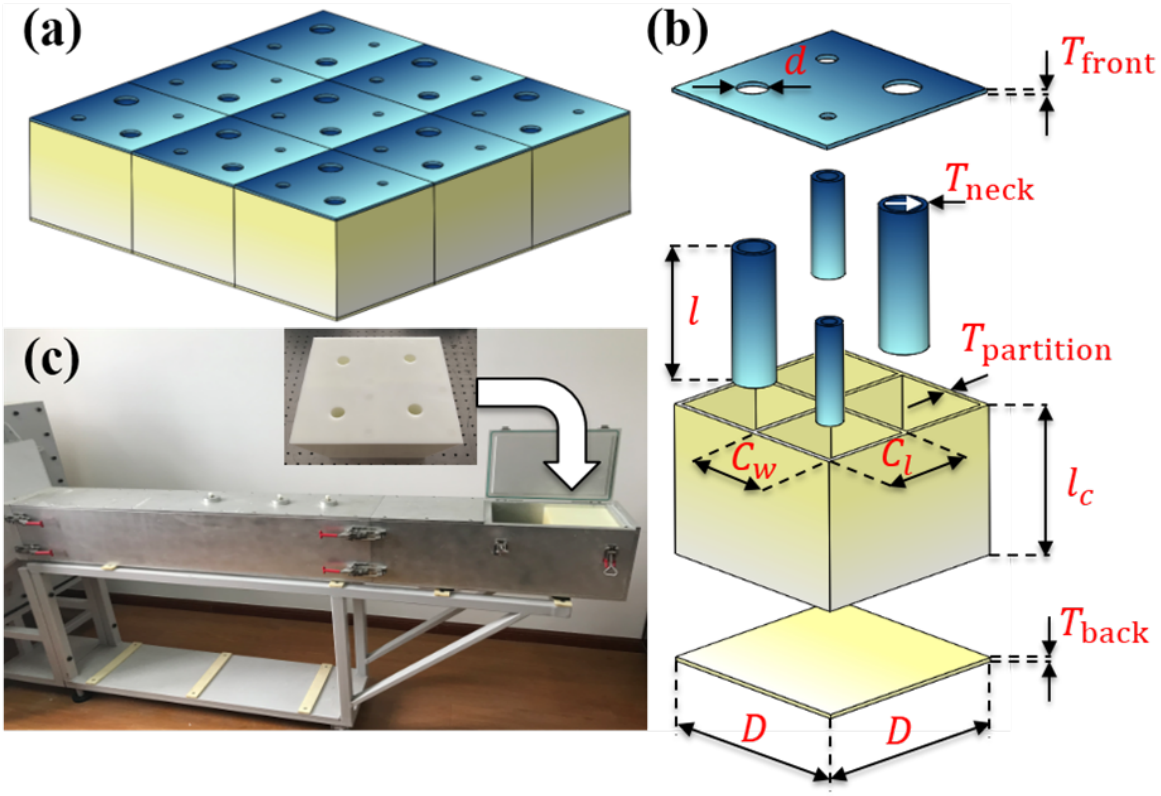

Figure 2.1. (a) Schematic of a metasurface absorber with 9 supercells. (b) The explosive view of one supercell with 4 different unit cells. The thickness of the front panel, T_{front}, the thicknesses of the necks' walls, T_{neck}, and the thicknesses of partitions, $T_{\text{partition}}$, are all set as 5 mm, according to our experimental trials, to mitigate the coupling effect between neighboring air domains through the shared partitions so that the assumption of acoustically rigid boundaries in the analytical and numerical models is genuinely valid. The thickness of the back panel, T_{back}, is 2 mm. The diameter of the neck is d, the length of the neck is $l_n = (l + T_{\text{front}})$, the lateral size of a unit cell is $S(C_w \times C_l)$, the length of the cavity is l_c, and the side length of a supercell is D. (c) The photograph of the experimental set-up for measuring absorption using the two microphones method. The lateral size of the impedance tube is 20 cm $\times$20 cm.

concludes the study.

2.2 Theoretical model

2.2.1 Description of metasurface geometry

Figure 2.1(a) shows the proposed metasurface with 2-dimensional periodic array of supercells. **Figure 2.1**(b) shows one supercell with different deep-subwavelength resonant units with embedded cylindrical necks. The incident pressure is $p_{in} = P_{in}e^{-j(k_x x + k_y y - k_z z)}$,

in which $k_x = k\sin\theta_{in}\cos\phi_{in}$, $k_y = k\sin\theta_{in}\sin\phi_{in}$, and $k_z = k\cos\theta_{in}$. θ_{in} is the polar angle of incidence and ϕ_{in} is the azimuthal angle of incidence. $k = \omega/c_0$. The time dependence $e^{j\omega t}$ is dropped for simplicity.

2.2.2 Theoretical model for a single resonant unit cell with the embedded neck

The Stinson's model [56, 77, 78], which is valid for a broad range of frequencies, is used to model the narrow neck with the visco-thermal loss effect taken into account. Therefore, we have the impedance for the cylindrical neck with a circular cross-section [56],

$$Z_n = -\rho_0 c_0 \frac{2j\sin(k_c l_n/2)}{\sqrt{(\gamma-(\gamma-1)\psi_h)\psi_v}} \tag{2.1}$$

where ρ_0, c_0 and γ are density, speed of sound and the ratio of specific heats of air. The values are taken as 1.21 kg/m^3, 343.2 m/s and 1.4. $k_c = k\sqrt{(\gamma-(\gamma-1)\psi_h)/\psi_v}$, $\psi_v = \frac{J_2(k_v d/2)}{J_0(k_v d/2)}$, and $\psi_h = \frac{J_2(k_h d/2)}{J_0(k_h d/2)}$ refer to the complex wave number, the viscous function and the thermal function of the embedded neck [56]. k_v and k_h the viscous wave number and the thermal wave number: $k_v^2 = -j\omega\frac{\rho_0}{\eta}$,$k_h^2 = -j\omega\frac{\rho_0 C_p}{K}$. η, C_p, and K are the dynamic viscosity of air, the specific heat at constant pressure and the fluid thermal conductivity, of which the values are taken as 1.825×10^{-5}kg/(m $\cdot$ s), 1007J/(kg $\cdot$ K), and 0.02514 W/(m $\cdot$ K). All the geometric symbols are referred to **Figure 2.1**(b). This model, which takes thermal loss into account for the long neck, has been well validated against experimental results recently [56]. Note that the conventional HR model [79] is only a special model derived from this generalized model [52, 77, 80].

For resonant unit cells whose dimensions are all much smaller than the working wavelength, the impedance for the irregular-shape cavity resulted from the embedded neck can be approximated as [56],

$$Z_c = -\frac{jS\rho_0 c_0^2}{\omega V} \tag{2.2}$$

where ω is the angular frequency. S and V are the lateral area and the volume of the cavity. $V = Sl_c - \pi(d/2+T_{\text{neck}})^2 l$. Under this scenario, it is the volume of the cavity that plays the important role. It is reasonable to neglect the thermal and viscous loss here since the dimensions of the cavity are much larger than the boundary layer thickness for the frequencies of interest. The overall impedance of the resonator can be approximated

as the sum of the impedances of the neck and cavity, which reads [56],

$$Z = Z_n + Z_c + 2\sqrt{2\omega\rho_0\eta} + j\omega\rho_0\delta \tag{2.3}$$

where the subscript n represents the neck and c represents the cavity. $2\sqrt{2\omega\rho_0\eta}$ is the resistance correction. $\delta = [1 + (1 - 1.25)\varepsilon] \times (\frac{4}{3\pi})d$ is the mass end correction in which $\varepsilon = d/\min(C_w, C_l)$ is the ratio of the neck's diameter to the narrower side of the cavity.

2.2.3 Theoretical model for supercell with different unit cells

When a supercell of the panel is composed of M different unit cells in parallel, its absorption performance can be characterized by a mean specific acoustic admittance or a mean specific acoustic impedance at normal incidence [81],

$$\frac{1}{Z_{\text{tot}}} = \sum_{1}^{M} \frac{\phi_N}{Z_N} \tag{2.4}$$

where Z_N is the specific acoustic impedance for resonator N in which end corrections of the neck to both the waveguide and the cavity are considered. ϕ_N is the surface porosity, $\phi_N = \pi(\frac{d_N}{2})^2/D^2$. Note that the far field interference coupling (e.g., constructive and destructive interference) among the reflected propagating waves from the individual unit cells [65] is implicitly included in **Eq. 2.4**. The sound absorption coefficient can be subsequently calculated by [82],

$$\alpha(f, \theta_{\text{in}}) = \frac{4\text{Re}(Z_{\text{tot}})\rho_0 c_0 \cos\theta_{\text{in}}}{[\rho_0 c_0 + \text{Re}(Z_{\text{tot}})\cos\theta_{\text{in}}]^2 + [\text{Im}(Z_{\text{tot}})\cos\theta_{\text{in}}]^2} \tag{2.5}$$

For normal incidence, a perfect absorption requires an impedance match between the panel and the air,

$$\begin{aligned} \text{Re}(Z_{\text{tot}}) &= \rho_0 c_0 \\ \text{Im}(Z_{\text{tot}}) &= 0 \end{aligned} \tag{2.6}$$

Although this method is physically straightforward, computationally inexpensive and accurate for our deep-subwavelength structures, several underlying assumptions and limitations need to be noted. First, **Eq. 2.5** can be assumed to be independent [83] of the azimuthal angle ϕ if the lateral size of the supercell is deep-subwavelength. Otherwise, an asymmetric absorption [37, 84] would be observed because of the geometric asymmetry, when the incident wave is from the same polar angle but different azimuthal

angles. Second, this frequently used method is an approximation in terms of the accuracy of the mean specific impedance. **Equation. 2.4** is based on the assumptions [81] that lateral sizes of necks are considerably smaller than the wavelength and the lateral size of the supercell is sufficiently small, at which the pressure is constant over the surface and the volume displacement is additive. These assumptions can also be understood in a mathematical manner: Only the fundamental mode wave dominates the scattering field and thus needs to be considered, when $\lambda \geq 2D$ [72], regardless of the angle of incidence. When these assumptions are invalid, the coupled-mode theory [37] and radiation impedance method [66, 84] can be used, which either implicitly or explicitly take into account the coupling of evanescent waves between unit cells. Third, the acoustic-structure interaction is neglected. The second and third assumptions will be carefully examined in this study.

Throughout this study we will use a figure of merit $\alpha_{avg,\theta}^{f_1-f_2}$ to characterize and evaluate the absorption performance of the sound absorbing panel, which is the average absorption coefficient from f_1 to f_2 at the incident angle θ.

2.2.4 Causal optimality in sound absorption

An absorber can be regarded as causally optimal when its thickness reaches the minimum limitation dictated by the principle of causality [39]:

$$T \geq \frac{1}{4\pi^2}\frac{B_{\text{eff}}}{B_0}\left|\int_0^\infty \text{In}[1-A(\lambda)]\,\mathrm{d}\lambda\right| = T_{\min} \tag{2.7}$$

where λ is the wavelength in air, $A(\lambda)$ is the absorption as a function of the wavelength, B_{eff} is the effective bulk modulus of the absorber in the static limit, and B_0 is the bulk modulus of the air. B_{eff} can be calculated as $\frac{B_0}{\phi_V}$, in which volume porosity $\phi_V \equiv V_{\text{air}}/V_{\text{tot}}$ is the volume fraction of the air domain considering $B_{\text{solid}} \gg B_{\text{air}}$.

2.3 Results and discussions

2.3.1 Design for 50-63 Hz (one-third octave) absorption without optimization

Motivated by the application of modal frequency absorption, four different resonant unit cells arranged in a supercell, with parameters listed in **Table. 2.1**, are realized,

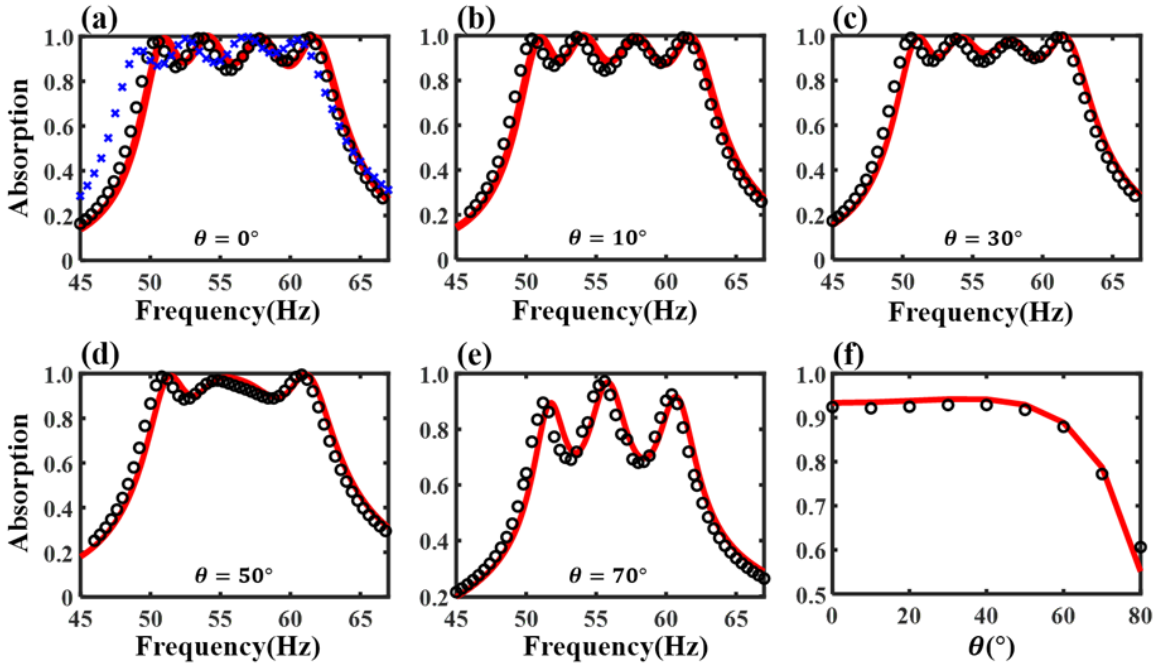

Figure 2.2. (a) The theoretical (red solid line), the first type of numerical (black circles) and experimental (blue crosses) absorption coefficient at normal incidence for the non-optimized metasurface absorber. (b)-(e) The theoretical and numerical absorption coefficient for the angles of incidence 10°, 30°, 50°, and 70°. (f) The theoretical and numerical average absorption coefficient over 50-63 Hz vs. angle of incidence.

with $\alpha_{avg,0^\circ}^{50-63} \approx 93\%$ for the analytical prediction and simulation, and $\alpha_{avg,0^\circ}^{48-61} \approx 93\%$ for the experiment, as shown in **Figure 2.2**(a). The total thickness is 19 cm, which is around 1/36 of the wavelength at 50 Hz. Its absorption performance over 50-63 Hz as a function of the angle of incidence is also shown in **Figures 2.2**(b)-(f). The analytical model is based on **Eq. 2.5**, while details of the sample fabrication and experimental setup are provided in **Section 2.4.1**. Details of the first type of numerical model can

Table 2.1. Geometric parameters of the metasurface absorber with 4 different unit cells without optimization. The lateral size of the supercell is 20 cm × 20 cm. The overall thickness of the absorber is 19 cm. Its volume porosity is 80%.

Number	f(Hz)	d(mm)	l_n(mm)	l_c(mm)	S(mm^2)
1	50.5	18.6	175.0	183.0	102.0×93.0
2	54.0	18.2	165.0	183.0	92.0×92.0
3	58.1	17.4	123.0	183.0	93.0×92.0
4	62.3	17.6	122.0	183.0	83.0×93.0

be found in **Section 2.4.2**. The first type of numerical model is distinct from the second type of numerical model, which will be discussed in Section 2.3.3. The average absorption coefficient over 50-63 Hz is observed to be around 90% for angles of incidence smaller than 60 degree, because of the subwavelength size of the supercell. For angles of incidence larger than 60 degree, the absorption drops, likely due to an impedance mismatch. Interestingly, starting from around 50°, only 3 absorption peaks appears instead of 4 peaks in the absorption spectrum, which is a signature of coupling between two unit cells [68] and this phenomenon is resulted from a coalescence of eigenstates [37, 85] as the incident angle changes.

The design principle of this absorber is described as follows. The lateral size of the supercell is fixed as 20 cm×20 cm, matching the size of our existing impedance tube (**Figure 2.1**(c)). The suitable number of unit cells in a supercell, which depends on the Q factor of unit cells and the desired 50-63 Hz absorption spectrum, is chosen as 4. Additional unit cells are needed, if their Q factor is larger [58]. To form a continuously high absorption spectrum, each unit cell is designed to have a perfect absorption, following **Eq. 2.6**, at a specific frequency inside the targeted absorption spectrum. The frequencies at which the perfect absorption occur are nearly equally spaced. By assuming a weak coupling effect between unit cells at these perfect absorption frequencies, each unit cell can thus be designed independently. During this design process, the lateral size of each unit cell is assigned without being optimized. In **Figure 2.3**(a), the absorption coefficients of the supercells with only one individual unit cell are plotted as mark lines (blue diamonds, green circles, magenta points and black crosses), while that of the supercell with all unit cells is plotted as red solid line. For example, the curve for "unit cell 1" is a plot of $Z_{\text{tot}}(f) = (Z_1(f))/\phi_1$, with $\phi_1 = (\pi(d_1/2)^2)/(20\text{cm})^2$. It is noted that the peaks of the red solid line, which indicates the near-perfect absorption of the supercell, matches well with peaks of the individual unit cells, which to a certain extent supports the assumption of the weak coupling between unit cells. It is, however, still too early to claim from these analytical results in **Figure 2.3**(a) that these near-perfect absorption points are contributed solely from individual unit cells operating independently. The underlying physical behavior will be revealed in the next paragraph by means of finite element method (FEM) simulations. Two important points of this trial-and-error design strategy should be mentioned. First, how large the cross-sectional area is assigned to each cavity is roughly proportional to the target wavelength because of the fact that a larger volume of cavity is required for a smaller resonant frequency. For example, unit cell 1 which targets the lowest frequency has a cavity with the largest cross-sectional area. The best

assignment of cross-sectional area to each cavity, however, is not investigated here but will be discussed in section 2.3.2. Second, the design of a long and embedded neck plays a critical role in minimizing the thickness of the unit cell for the longest wavelength and thus the overall thickness of the supercell, because a large phase delay is correlated with a long neck [18]. During the design of unit cell 1, the neck length l and the length of its cavity l_c can be obtained by solving **Eqs. 2.6**, whereas d is parametrically swept and the cross-sectional area is set as 93 mm$\times$102 mm. One set of l and l_c is chosen, in which l is as close as possible to l_c but a clearance between l and l_c is left to ensure that the mass end correction is physically meaningful. The concept of curved necks [56], which is capable of further shrinking the total thickness, is not used here though, considering the fabrication complexity.

To gain insights concerning how the supercell is behaving at these near-perfect absorption frequencies, the sound intensity fields just above the supercell surface are drawn at the resonant frequencies of two selected unit cells (53.6 Hz and 57.8 Hz) using COMSOL in **Figures 2.3**(b)-(e). At these resonant frequencies, the sound intensity is observed to be highly concentrated and drawn to the only unit cell whose mode is excited. Instead of "penetrating" the entire supercell and being absorbed by all the unit cells at a similar amount, the sound energy is dissipated mostly by one resonating unit cell while other unit cells behave in a way as if they were "sealed". This is a clear signature of the weak coupling between the resonant unit cells at the resonant frequencies, and thus it confirms the validity to design each unit cell independently for a near-perfect absorption.

2.3.2 Design for 50-63 Hz (one-third octave) absorption with optimization

In the previous section, the achieved design for the desired absorption spectrum has room to shrink the thickness, considering several deficiencies during the design methodology. First, by assuming a weak coupling between unit cells, all unit cells in the previous section are designed independently to realize near-perfect absorption at their individual resonant frequencies to form a continuously high absorption spectrum. A better assignment of the contribution from all unit cells to the total absorption at each individual frequency of interest is left to be resolved. Second, the assignment of the cross-sectional area to each cavity follows an empirical idea: Generally, a larger cross-sectional area is required for a lower frequency if the cavities are required to have the same depth. A better assignment of cross-sectional areas also needs to be proposed. To address the two concerns above,

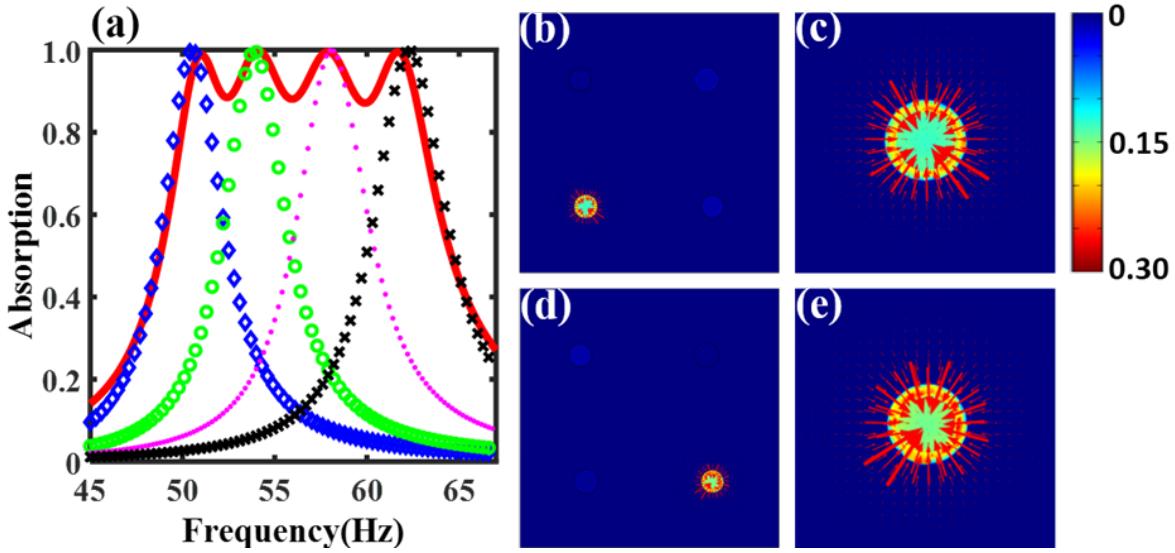

Figure 2.3. (a) The theoretical absorption coefficient of the non-optimized supercell (red solid line) and individual unit cells (blue diamonds, green circles, magenta points and black crosses are for unit cell 1,2,3 and 4 respectively). The curve for "unit cell N" is an absorption spectrum for a metasurface in which only unit cell N can interact with the incident sound and all the other unit cells are blocked at the front panel. N=1,2,3,4. Sound intensity maps of the non-optimized supercell at (b) 53.6Hz and (d) 57.8Hz, respectively. The bottom-left unit cell of (b) and the bottom-right unit cell of (d) are enlarged, as shown in (c) and (e), respectively. The incident pressure is normalized to 1 Pa. Color bar (W/m^2): component of the sound intensity vector that are perpendicular to the supercell surface, i.e., I_z. Arrow: components of the sound intensity vector that are parallel to the supercell surface, i.e., I_x and I_y. The size of the arrows is proportional to the magnitude of the intensity.

the lateral areas of unit cells are assigned as additional variables to be treated in GA, while the thickness of the absorber is to be optimized for the same absorption spectrum, i.e., $\alpha_{avg,0^\circ}^{50-63} \geq 93\%$. The details of variables, constraints and the object function are listed in **Section 2.4.3**. Note that the area of supercell, instead of being a variable in the next section, is also fixed to be 20cm $\times$ 20cm which is the size of our impedance tube.

Figure 2.4 shows the absorption performance of the optimized design, which is 15.4 cm (1/44.5 of the wavelength at 50 Hz) and is 23% thinner than the non-optimized one, with the geometric parameters listed in **Table. 2.2**. However, its average absorption performance is not sacrificed as shown from the comparison of two designs' performance in **Table. 2.3**. Note that the average frequency range for the analytical predictions and the numerical results is 50-63 Hz, while that for the experiment is 48-61 Hz because of the small frequency shift as shown in **Figure 2.2**(a) and **Figure 2.4**(a). The larger mismatch between the experimental result and the analytical prediction of the optimized

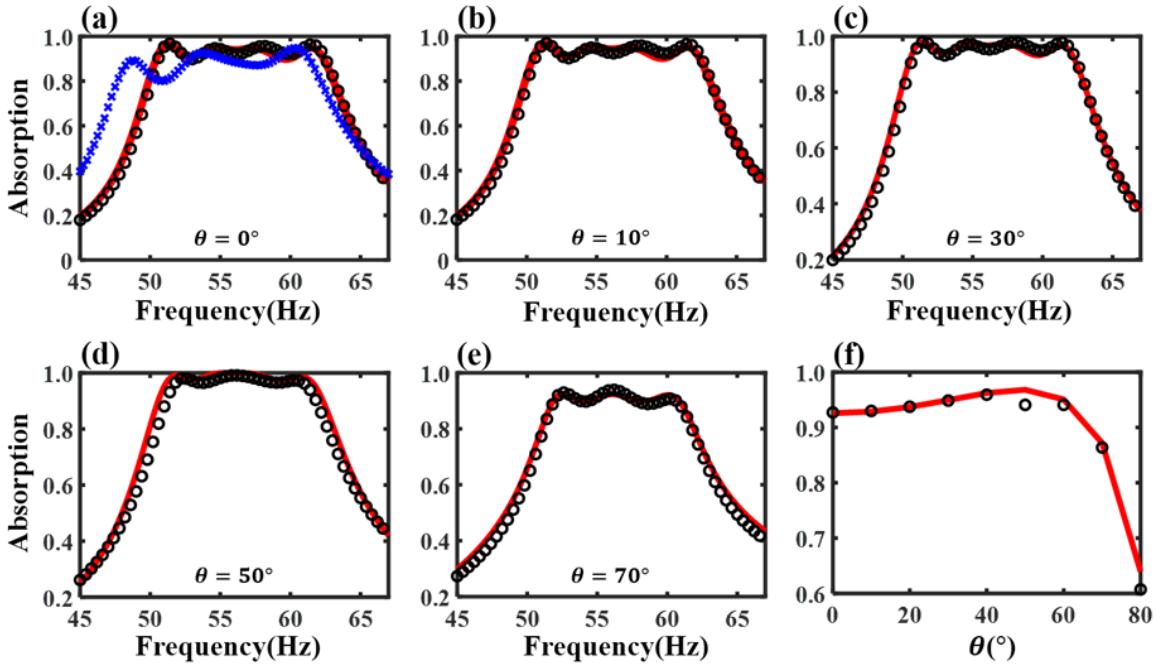

Figure 2.4. (a) The theoretical (red solid line), the first type of numerical (black circles) and experimental (blue cross) absorption coefficient at normal incidence for the optimized metasurface absorber. (b)-(e) The theoretical and numerical absorption coefficient for the angles of incidence 10°, 30°, 50°, and 70°. (f) The theoretical and numerical average absorption coefficient over 50-63 Hz vs. angle of incidence.

design, compared with that of the non-optimized design, can be reasonably explained by a larger fabrication error, as shown in **Section 2.4.1**. The maximum tolerance is 0.4 mm for the optimized sample, which is larger than that of the previous unoptimized sample, which is 0.1 mm.

Next, we will uncover how the supercell thickness can be reduced while the absorption performance is maintained. In contrast to the fairly weak coupling between unit cells demonstrated from the previous design at these near-perfect absorption points, a strong

Table 2.2. Geometric parameters of the optimized metasurface absorber composed of 4 different unit cells. The lateral size of the supercell is 20 cm×20 cm. The overall thickness of the absorber is 15.40 cm. Its volume porosity is 84%.

Number	d(mm)	l_n(mm)	l_c(mm)	S(mm^2)
1	12.4	72.4	147.0	112.1×99.9
2	9.9	63.2	147.0	80.7×88.1
3	7.6	21.1	147.0	107.3×88.1
4	11.6	62.7	147.0	75.9×99.9

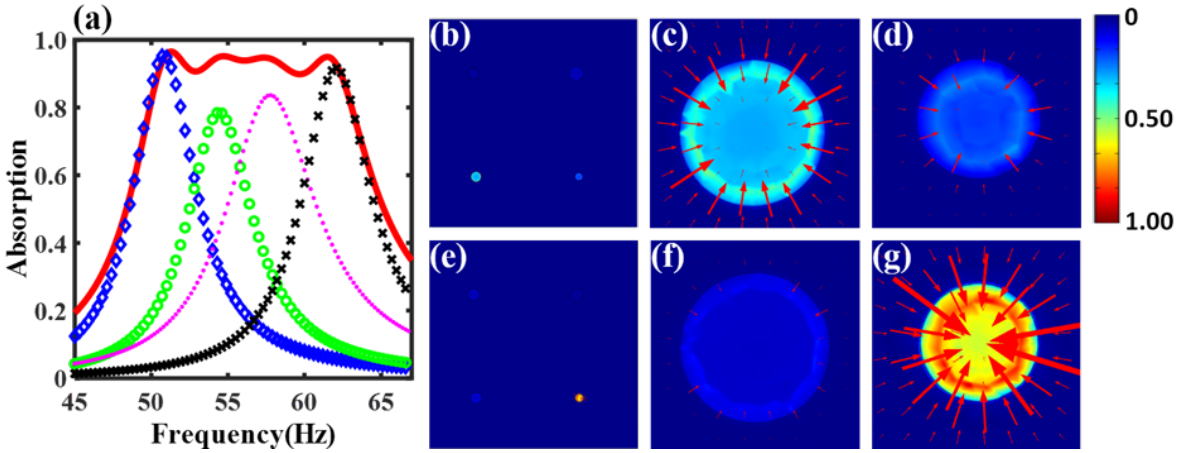

Figure 2.5. (a) The theoretical absorption coefficient of the optimized supercell (red solid line) and individual unit cells (blue diamonds, green circles, magenta points and black crosses are for unit cell 1,2,3 and 4 respectively). The curve for "unit cell N" is an absorption spectrum for a metasurface in which only unit cell N can interact with the incident sound and all the other unit cells are blocked at the front panel. N=1,2,3,4. Sound intensity maps of the optimized supercell at (b) 54.4 Hz and (e) 57.8 Hz, respectively. The bottom-left unit cell and the bottom-right unit cell of (b) are enlarged, as shown in (c) and (d), respectively. The bottom-left unit cell and the bottom-right unit cell of (e) are enlarged, as shown in (f) and (g), respectively. The incident pressure is normalized to 1 Pa. Color bar (W/m^2): component of the sound intensity vector that are perpendicular to the supercell surface, i.e., I_z. Arrow: components of the sound intensity vector that are parallel to the supercell surface, i.e., I_x and I_y. The size of the arrows is proportional to the magnitude of the intensity.

coupling, at which more than one unit cells jointly contribute to the total absorption, is observed as shown in **Figure 2.5**(a). The intensity plots for the middle two peaks of the absorption curve (i.e., 54.4 Hz and 57.8 Hz) are used to further shed light on the strong coupling. As shown in **Figures 2.5**(b)-(d), two different unit cells are excited simultaneously and strongly coupled to work as energy sinks at 54.4 Hz. At 57.8 Hz, this phenomenon is not as pronounced as that at 54.4 Hz because the portion of absorption from one of the unit cells is large, as shown in **Figures 2.5**(e)-(g). Theoretically speaking, the strong coupling is the interference of the reflected propagating waves from the simultaneously excited unit cells. The total reflected propagating wave is a linear combination of the reflected propagating waves from all the individual unit cells. Interference, a fundamental wave phenomenon, happens among these reflected propagating waves, which creates the ripples in the absorption spectrum of the supercell and even changes the number of absorption peaks (**Figure 2.4**(f)). Consequently, each individual unit cell is not required to satisfy the near-perfect absorption requirement [27] like shown in **Figure 2.3**. Moreover, the assignment of cross-sectional areas to

these non-uniform cavities is judiciously tuned thanks to the assistance of GA. As shown in **Table. 2.2**, for the unit cell 1, which corresponds to the lowest resonant frequency, its cross-sectional area is 112.1 mm×99.9 mm, which is 18% larger than that of the non-optimized design, i.e., 102.0 mm×93.0 mm, while its neck and cavity lengths are shortened. Benefiting from the strong coupling and well-designed non-uniform cavities, the thickness of supercell, which is highly dependent on the neck and cavity lengths of unit cell with the lowest resonant frequency, is decreased from 19 cm to 15.4 cm by 23%. This can be well explained from the perspective of the causality constraint (**Eq. 2.7**): The larger the volume porosity is, the smaller the minimum thickness is. Our optimized design, which has shorter embedded necks and thus a larger volume porosity, has a smaller actual thickness T and a smaller causally minimum thickness T_{min} as well, as shown in **Table. 2.3**.

The Hamiltonian from the coupled-mode theory [75, 76] is likely another way to interpret the interference coupling in the far field [74, 86]. Taking the system at the second absorption peak (i.e., at 54.4Hz) of normal incidence as an example, two resonators are effectively excited so that the four-state system can be reduced to a two-state system at this frequency. This two-state system is coupled to one port since here only the plane wave mode exists in the far field under the cutoff frequency of the waveguide. Thus, the effective Hamiltonian of this two-states, one-port open system is written as [74, 75, 76],

$$H_{\text{eff}} = \begin{pmatrix} \Omega_2 + j\delta_2 & \kappa \\ \kappa & \Omega_3 + j\delta_3 \end{pmatrix} + j \begin{pmatrix} \gamma_2 & \sqrt{\gamma_2\gamma_3} \\ \sqrt{\gamma_2\gamma_3} & \gamma_2 \end{pmatrix} \tag{2.8}$$

where Ω_n, δ_n and γ_n are the resonance frequency, the intrinsic loss rate and the radiation leakage rate to the port for the n^{th} resonator. κ is the near filed coupling which, in this case, is the evanescent wave [39] on the surface of the absorber panel. Since the off-diagonal terms represent the coupling effect between resonators, there are two kinds of

Table 2.3. Comparison of the absorption performance between the non-optimized (design A) and the optimized (design B) absorber. "Theory" and "Simulation" refer to the average absorption coefficients over 50-63 Hz based on the analytical model and the first type of numerical result, while "Experiment" refers to the average absorption coefficient over 48-61 Hz based on the experimental result. ϕ_V and T are the volume porosity and total thickness of the design. T_{min} is the minimum thickness dictated by the principle of causality (i.e., (**Eq. 2.7**)).

	Theory	**Simulation**	**Experiment**	ϕ_V	T(mm)	T_{min}(mm)
Design A	93.3%	92.4%	93.1%	0.80	190.0	169.7
Design B	92.6%	92.7%	87.8%	0.84	154.0	149.1

couplings [74] in the open system, i.e., the near field coupling κ and the far field coupling $\sqrt{\gamma_2\gamma_3}$. The near field coupling exists when the resonant modes belong to different closely distributed resonators, while the far field coupling exists when the modes have the same symmetry. The near field coupling, however, in this case is negligible, though they satisfy the condition above. This is because that the analytical model (**Eq. 2.4**), which does not consider the effect of coupling of the evanescent wave by means of self-energy term [39], still matches well with the numerical simulation in which the near field coupling is considered. Therefore, it is the interference coupling in the far field [86] that likely results in the total absorption of the supercell, which cannot be obtained by simply the summation of absorptions from each individual unit cell. We also note that, different from the closed system [85] in which the coupling term is resulted from the near field coupling, our system is an open system in which the radiation leakage γ can also become the off-diagonal elements but result in the coupling effect in the far field. Instead of the manipulation of near field coupling [39] in their open system, our improved design benefits from the far field coupling under the framework of the Hamiltonian, which similarly, is illustrated as the coherent coupling effect [65] by designing a larger number of imperfect absorbers to enhance sound absorption.

2.3.3 The coupling through the evanescent wave and acoustic-structure interaction

Besides the interference coupling in the far field, there also exists two types of coupling mechanisms in our absorber within the frequency range of interest: the evanescent wave coupling on the top surface via air and the acoustic-structure interaction between cavities through partitions. In **Figure 2.2** and **Figure 2.4**, the first type of simulations has considered evanescent wave coupling but not the acoustic-structure interaction. To consider the acoustic-structure interaction, the second type of simulations is performed using the Thermoviscous Acoustic-Solid Interaction Module of COMSOL Multiphysics 5.4 with detailed settings in **Section 2.4.2**. The coupling effects that each model takes into account are summarized in **Table. 2.4**. The absorption coefficient curves of different models for the non-optimized and the optimized design are plotted in **Figures 2.6**(a)-(c) and **Figures 2.6**(d)-(f). As shown in **Table. 2.4**, the difference between the theoretical model and the first type of numerical simulation is that the former does not consider the evanescent waves while the latter does. The difference between the first and second type of numerical model is that the former does not consider the acoustic-structure

interaction while the latter does. This means that we can separately evaluate the validation of the assumptions that are made in section 2.2.3 about the evanescent wave and acoustic-structure interaction by comparing the results in **Figure 2.6**.

One observation of **Figure 2.6** is that the positions of the peaks of the first type of numerical results are all slightly down-shifted from the theoretical predictions because of the coupling by the evanescent waves. This observation is consistent with the one in the supplementary material of [39] and shows that the coupling by the evanescent waves is negligible.

Another observation of **Figure 2.6** is the redshift of the second type of numerical results compared with the first type of numerical results. This is consistent with the redshift of the experimental results compared with the first type of numerical results, and this is resulted from the relatively weak acoustic-structure interaction through the partitions. The weak acoustic-structure interaction could be explained as follows: First, whether the structural resonance happens within the frequency of interest is examined. We numerically calculate the modal frequencies of the whole structure. For the normal incidence case, the bottom surface and four side surfaces are assumed as fixed to mimic the boundary conditions in a waveguide. For the oblique incident cases, the bottom surface is assigned as fixed and the four side surfaces are assigned as the Floquet periodic condition. In all these cases, the lowest modal frequencies are around 800 Hz, which are beyond of the range of our interest. This means that no structural resonance occurs within the frequency range of interest so that the interaction between the neighboring cavities through the partition can be approximated as a transmission problem involving only acoustic waves. In this case, we can estimate the effect of the 5 mm partition by calculating its plane wave pressure transmission coefficient (material properties are in **Section 2.4.1**), which is approximately 8% at 50 Hz when the wave direction is perpendicular to the partition. This means that the impedance and the thickness of the partition are large enough that the transmission through the partition at the frequency range of interest is reasonably small. Thus, the acoustic-structure interaction manifests itself as a small sound transmission through the partition in our case, which effectively makes the cavity less stiff and consequently results in the redshift of the resonant frequency.

Based on the above analysis and observation, the analytical model, which does not consider the acoustic-structure interaction as well as the evanescent coupling, is acceptable as a simple model to design the absorber, as long as structural resonance is not excited and the impedance and thickness of the partition are large enough to effectively reduce

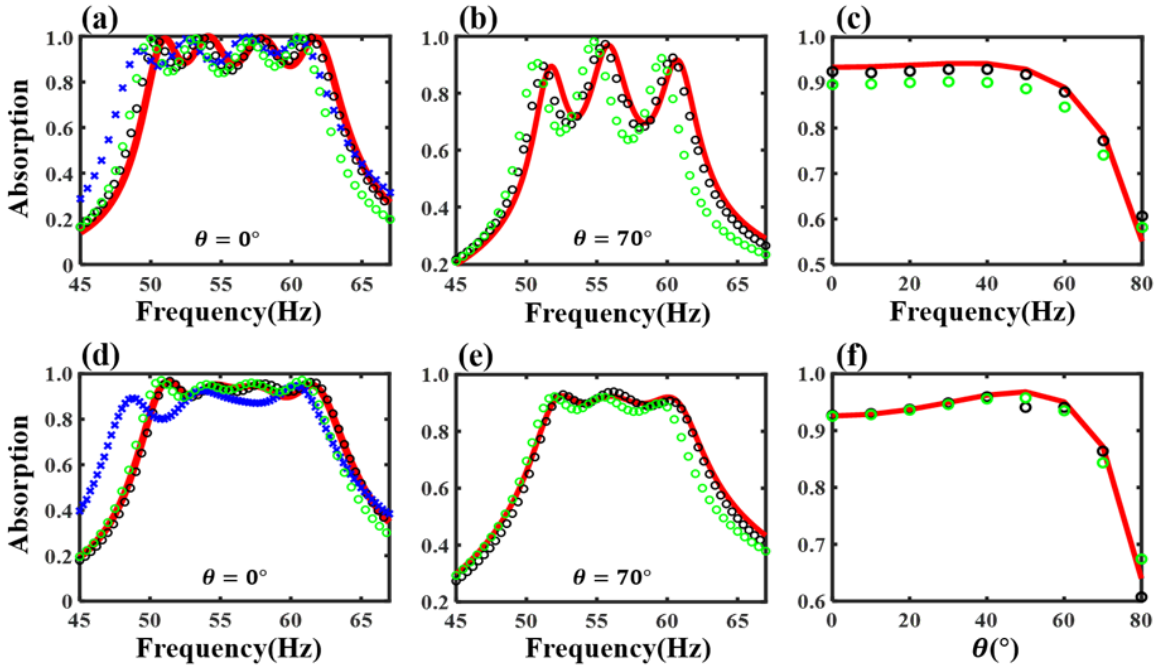

Figure 2.6. (a) The theoretical (red solid line), the first type of numerical (black circles), the second type of numerical (green circles) and experimental (blue cross) absorption coefficient at normal incidence. (b) The theoretical and the two types of numerical absorption coefficient for the angle of incidence 70°,. (c) The theoretical and the two types of numerical average absorption coefficient over 50-63 Hz vs. angle of incidence. (a)-(c) and (d)-(f) are for the non-optimized and the optimized metasurface absorber.

the sound transmission.

2.3.4 Design for 50-100 Hz (one octave) absorption with optimization

The optimized metasurface absorber, which benefits from the strong coupling between unit cells with judiciously designed cavities, is further explored to realize 50-100 Hz

Table 2.4. The coupling effects that each model takes into account. By comparing the corresponding curves in **Figure 2.6**, the evanescent wave coupling and the acoustic-structure interaction can be separately evaluated for the validation of the assumptions that are made in the chapter 2.2.3.

	The interference in the far field	The evanescent wave coupling	The acoustic-structure interaction
Theory	Yes	No	No
1st type of simulations	Yes	Yes	No
2nd type of simulations	Yes	Yes	Yes
Experiments	Yes	Yes	Yes

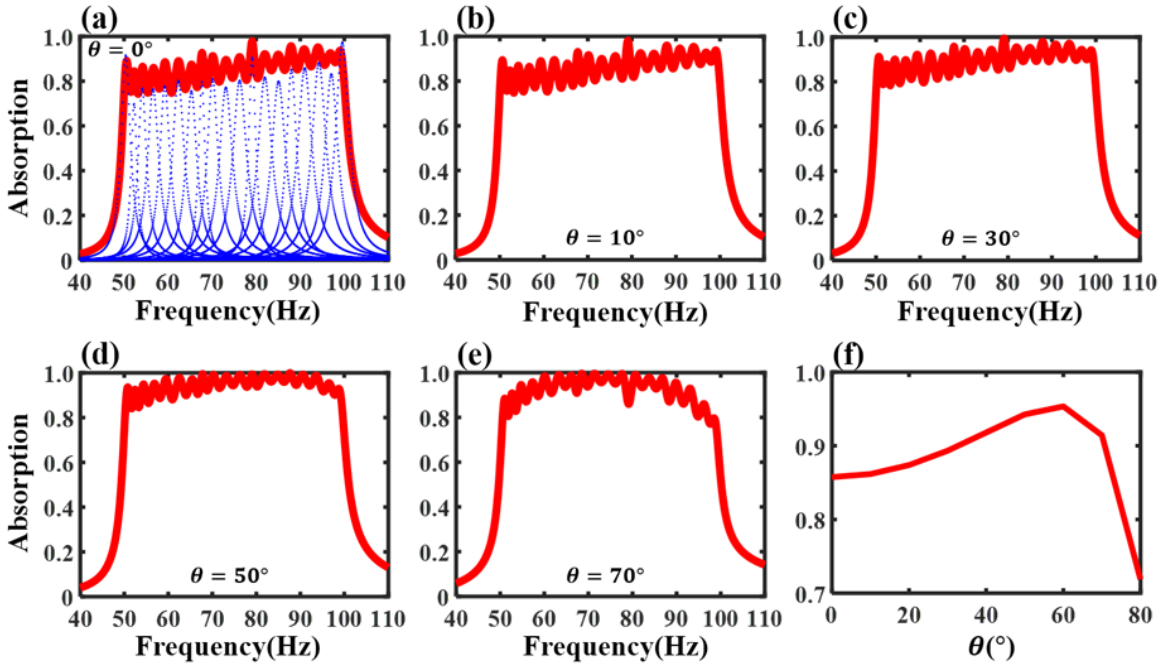

Figure 2.7. (a) The absorption coefficient of the optimized supercell (red solid line) and individual unit cells (blue points lines) at normal incidence. (b)-(e) The theoretical absorption coefficients for the angles of incidence 10°, 30°, 50°, and 70°. (f) The theoretical average absorption coefficient over 50-100 Hz vs. angle of incidence.

absorption. The lateral size of the supercell for an optimal design will be discussed below, instead of being assumed as 20 cm× 20 cm. For this reason, the experimental validation is not conducted in the section. The absorption performance of a resonator is conventionally [82] characterized by its maximum absorption cross section, which is in fact the lateral size of the supercell at which the perfect absorption condition (i.e., **Eq. 2.6**) is satisfied. The lateral size is also recently demonstrated to be directly related to the effective porosity [63, 64] and thus the impedance matching condition in **Eq. 2.6**(a). Besides, the number of unit cells, which is a bridge between the absorption ability (e.g., bandwidth) of a single unit cell and the overall absorption of the supercell, is an additional important variable not well discussed in previous literatures.

With the above concerns, GA is used as an efficient tool to seek an optimal design which satisfies $\alpha_{avg,0^\circ}^{50-100} \geq 85\%$, in which the two additional variables, (the lateral size of supercell D and the number of unit cells M), are incorporated. The details of variables, constraints and the object function are listed in **Section 2.4.4**. An optimal design, at a thickness of 20 cm (which is 1/34.3 of the wavelength at 50 Hz) and a lateral size of 78.84 cm × 78.84 cm, is achieved with all the other parameters listed in **Table. 2.5**.

Within the supercell, there are 19 different unit cells whose lateral sizes are well tuned. **Figure 2.7**(a) shows the analytically predicted absorption for the supercell and individual unit cells. The analytical model is valid since the dimensions of the supercell satisfy the assumptions discussed in Section 2.2.3. The FEM validation is not provided here since the existing computation resource in our lab is insufficient for this design with 19 unit cells. The analytical prediction, however, has been proven to be accurate in previous two designs. The average absorption coefficient over 50-100 Hz as a function of angle of incidence is plotted in **Figure 2.7**(f) and remains above 85% until 75 degree, which again demonstrates its near-omnidirectional absorption capability. The absorptions at 10,30,50 and 70 degree are plotted in **Figures 2.7**(c)-(e), respectively.

It is noted that the achieved design is causally optimal: If we insert the achieved absorption spectrum (the red curve in **Figure 2.8**) of our design and the corresponding volume porosity (90% for this design) into **Eq. 2.7**, $d_{\min}$ is calculated as 20 cm, which is precisely the thickness of our design.

Next, we will uncover how the two additional design variables, like the geometric

Table 2.5. Geometric parameters of an optimized metasurface absorber composed of 19 different unit cells. The lateral size of the supercell is 78.84 cm × 78.84 cm. The overall thickness of the absorber is 20 cm. Its volume porosity is 90%.

Number	d(mm)	l_n(mm)	l_c(mm)	S(mm^2)
1	38.4	122.9	193.0	145.6×137.4
2	21.1	11.9	193.0	145.6×137.4
3	34.4	138.3	193.0	145.6×137.4
4	26.1	33.1	193.0	145.9×137.4
5	30.4	145.7	193.0	180.8×137.4
6	20.1	5.6	193.0	144.8×176.0
7	19.2	5.3	193.0	147.8×176.0
8	17.5	5.2	193.0	149.3×176.0
9	25.6	8.9	193.0	157.4×176.0
10	17.7	5.0	193.0	164.2×176.0
11	20.8	17.9	193.0	144.1×211.6
12	17.1	7.1	193.0	146.9×211.6
13	19.1	16.8	193.0	149.5×211.6
14	17.1	5.0	193.0	150.4×211.6
15	22.6	39.1	193.0	172.5×211.6
16	19.5	18.5	193.0	156.3×243.4
17	17.3	7.9	193.0	172.3×243.4
18	17.2	10.8	193.0	180.7×243.4
19	23.3	22.5	193.0	254.1×243.4

parameters of all unit cells, play critical roles in reaching the causally optimal design (the minimum thickness) for a desired absorption spectrum. For the lateral size of supercell being a suitable value, on one hand, it should be as large as possible so that the lateral size of unit cells can be larger and therefore the thickness of all unit cells can be smaller to meet the design objective. On the other hand, it cannot be too large because that will result in an impedance-mismatch for individual unit cells and thus a drop of absorption coefficient. The number of unit cells should also be properly chosen. If the number of unit cells is too small, it would be insufficient to achieve such a broad absorption spectrum by coupling. However, if the number of unit cells is too large and the thickness is preserved, it would call for an increased lateral size of the supercell, which would result in a reduction of the impedance match and the absorption performance. Similarly, for such a case of a large number of unit cells, if the lateral size of the supercell is chosen to be preserved for the desired absorption performance, it would result in an increase in the thickness of the supercell.

In addition, we would like to further comment on the impact of the causality constraint on guiding the thinnest design of the linear and passive absorber for a desired absorption spectrum. First, it is not difficult to design an absorber which is causally optimal as indicated in the supplemental material of reference [39]: The MPP or sponge can easily become causally optimal if the desired absorption is not required to be high over a broad low frequency range. However, it is hard to realize a high absorption at such a low-frequency and broad range as presented in the study, i.e., 50-100 Hz. Second, as shown in **Eq. 2.7**, the optimal thickness not only relies on the achieved absorption spectrum, but also is highly dependent on the volume porosity. The larger the volume porosity is, the smaller the optimal thickness is. In other words, a better space utilization makes an absorber thinner. A higher volume porosity ($\approx 95\%$) can be achieved by making the partitions between the unit cells as thin as 1 mm, at which the partitions may not be treated as ideally rigid anymore. Third, designing an absorber whose absorption spectrum is as close as possible to the desired one is crucial to shrink the minimum thickness, especially for low frequencies. As shown in **Figure 2.8**, the absorption spectrum of an ideal absorber, whose absorption spectrum exactly matches with the desired one (85% over 50-100 Hz in this case), is plotted as a benchmark. The proposed design exhibits an absorption performance fairly close to the desired one with little unwanted absorption outside the frequency range of interest. This is due to the fine manipulation of acoustic surface impedance and the absorption spectrum by utilizing unit cells with large Q factors. The optimal thickness of the ideal absorber is 16.9 cm by substituting a volume

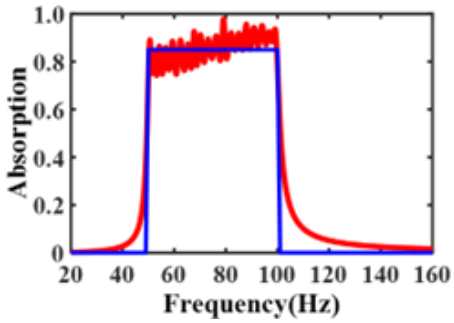

Figure 2.8. The absorption coefficient of the optimized supercell (red solid line) and the ideal absorber (blue solid line) at normal incidence. The optimal thickness for the optimized design is 20 cm. The optimal thickness for the ideal design is 16.9 cm when the volume porosity is set as 1 and the achieved absorption spectrum exactly matches with the desired one (85% over 50-100 Hz) in Eq. 7.

porosity of 100% and the desired absorption spectrum (the blue curve in **Figure 2.7**) into **Eq. 2.7**. Thus, our 20 cm design is not only causally optimal, but is also close to the ideal design. This is benefited from an adequate tuning range of acoustic impedances, which is provided by the three DOFs during the design of supercell, to simultaneously shape the absorption spectrum and to maintain a high volume porosity. The three DOFs in fact provide a similar functionality as the sponge does in [39] where lateral sizes of unit cells are uniform, and the lateral size of the supercell as well as the number of unit cells are fixed.

2.4 Methods

2.4.1 Sample fabrication and experimental setup

The sample is fabricated by using 3D-printing involving laser sintering stereo-lithography (SLA) and photosensitive resin (UV curable). The material density is approximately 1800 kg/m^3 and its speed of sound is approximately 2700 m/s. The nominal precision is 0.1mm. For design A, the measured diameters of necks are 18.50 mm, 18.17 mm, 17.38 mm and 17.60 mm, while the desired ones are 18.6 mm, 18.2 mm, 17.4 mm and 17.6 mm, as shown in Table 1. Thus, the maximum tolerance is 0.1 mm. For design B, the measured diameters of necks are 12.22 mm, 9.50 mm, 7.25 mm and 11.35 mm, while the desired ones are 12.4 mm, 9.9 mm, 7.6 mm and 11.6 mm, as shown in Table 2. Thus, the maximum tolerance for design B is 0.4 mm. The inconsistent tolerance might be a result of the quality of the resin.

The absorption coefficient is tested with a self-made impedance tube whose cross section is 20 cm by 20 cm, as shown in Fig. 1(c). The measurements of the absorption coefficient were performed using the impedance tube method complying with ASTM C384-04 (2011) and ASTM E1050-12. Two 1/4-inch condenser microphones (Bruel & Kjær type-4187) are situated at designated positions to obtain the amplitude and phase of the pressure distribution. A digital signal (white noise) generated by the computer was sent to the power amplifier (Bruel & Kjær type-2734) and then powered the loudspeaker. By analyzing the signals from the two microphones, the absorption coefficient can be obtained.

2.4.2 Numerical simulations

The first type of numerical simulations which does not consider the acoustic-structure interaction is performed under Acoustic-Thermoviscous Acoustic Interaction Module of COMSOL Multiphysics 5.4. Owing to the large difference between the acoustic characteristic impedances for solid and air, the walls of the necks, the front panel, the back panel and the partitions are assumed to be sound-hard boundaries, with no-slip and isothermal boundary condition applied. A Floquet periodicity is applied to the four side surfaces of the supercell.

The second type of numerical simulations which considers the acoustic-structure interaction is performed under Thermoviscous Acoustic-Solid Interaction Module of COMSOL Multiphysics 5.4. The walls of the necks, the front panel, the back panel and the partitions are modelled with Solid Mechanics module, with a fixed constraint being applied to the bottom of the back panel. Density, speed of sound and Poisson's ratio of the material are set as 1800 kg/m^3, 2700 m/s and 0.35. A Floquet periodicity is applied to the four side surfaces of the supercell, and a fixed constraint boundary condition is applied to the bottom surface.

In both types of numerical simulations, the absorption coefficient is calculated by a ratio of the total dissipated power to the incident power. The total dissipated power is acquired by a volumetric integral of a default variable called total thermo-viscous power dissipation density in COMSOL. To ensure the accuracy of simulation, a mesh independent test is carried out and solutions converge when the largest element size is set as 1/6 of the smallest working wavelength, the largest element size at the neck region is refined as 1/4 of the corresponding radius, the number of boundary layer is set as 6 and the thickness of first layer is set as 1/5 of viscous boundary layer thickness.

2.4.3 GA optimization for 50-63 Hz (one-third octave)

Genetic Algorithm in the toolbox of MATLAB is used to optimize our designs. The population size is 1000 and the crossover fraction is 0.8. Elite count, which selects the fittest individuals to dominate the population, is set as 20. The optimization stops after 50 stall generations. Due to the nature of heuristics, the algorithm is run 30 times for each design to find the globally optimal result. Parallel computing in MATLAB is used to minimize the computing time. To further speed up the optimization, the following design variables and constraints should be normalized.

For the design aimed at$\alpha_{avg,0^\circ}^{50-63} \geq 93\%$, there are 16 design variables:

$$X = (d_1, d_2, d_3, d_4, l_1, l_2, l_3, l_4, l_{c,1}, l_{c,2}, l_{c,3}, l_{c,4}, S_1, S_2, S_3, S_4) \tag{2.9}$$

The object is to minimize the sample thickness $F = \max(l_{c,1}, l_{c,2}, l_{c,3}, l_{c,4})$, which subjects to:

$$\begin{cases} \alpha_{avg,0^\circ}^{50-63} \geq 93\% & \\ 0.1 \leq \frac{d_N/2}{\sqrt{\frac{\eta}{(2\pi\rho_0 f_2)}}} \leq 100 & \text{for} N = 1,2,3,4 \\ T_{\text{front}} \leq l_N \leq \frac{c_0}{4f_1} & \text{for} N = 1,2,3,4 \\ 0 \leq S_N \leq D^2 & \text{for} N = 1,2,3,4 \\ l_N \leq l_{c,N} \leq \frac{c_0}{4f_1} & \text{for} N = 1,2,3,4 \\ 4 \times (d_N/2 + T_{\text{neck}})^2 \leq S_N & \text{for} N = 1,2,3,4 \\ \sum_{N=1}^{4} S_N + S_{\text{partition}} \leq D^2 & \end{cases} \tag{2.10}$$

For the constraints above, the first one is the desired absorption performance, which is calculated by the analytical model (**Eqs.2.1-2.5**). All the other constraints are geometric constraints, which are used to narrow the design space. The second constraint is the relationship between the radii of necks and the viscous boundary layer. The third and the fifth constraints require the lengths of the necks and cavities to be smaller than one quarter of the longest working wavelength. The fourth, the sixth and the seventh constraints require the lateral sizes of the cavities, the necks and the supercell to be feasible for manufacturing.

2.4.4 GA optimization for 50-100 Hz (one octave)

For the Design aimed at $\alpha_{avg,0^\circ}^{50-100} \geq 85\%$, there are $4M+2$ (M is defined in Chapter 2.2.3 as the number of unit cells in a supercell) design variables:

$$X = (D, d_1, d_2, d_3, \ldots, d_M, l_1, l_2, l_3, \ldots, l_M, l_{c,1}, l_{c,2}, l_{c,3}, \ldots, l_{c,M}, S_1, S_2, S_3, \ldots, S_M) \tag{2.11}$$

The object is to minimize the sample thickness $F = \max(l_{c,1}, l_{c,2}, l_{c,3}, \ldots, l_{c,M})$, which subjects to:

$$\begin{cases} \alpha_{avg,0^\circ}^{50-100} \geq 85\% & \\ 0.1 \leq \frac{d_N/2}{\sqrt{\frac{\eta}{(2\pi\rho_0 f_2)}}} \leq 100 & \text{for} N = 1, 2, 3, ..., M \\ T_{\text{front}} \leq l_N \leq \frac{c_0}{4f_1} & \text{for} N = 1, 2, 3, ..., M \\ 0 \leq S_N \leq D^2 & \text{for} N = 1, 2, 3, ..., M \\ l_N \leq l_{c,N} \leq \frac{c_0}{4f_1} & \text{for} N = 1, 2, 3, ..., M \\ 4 \times (d_N/2 + T_{\text{neck}})^2 \leq S_N & \text{for} N = 1, 2, 3, ..., M \\ \sum_{N=1}^{M} S_N + S_{\text{partition}} \leq D^2 & \end{cases} \tag{2.12}$$

For the constraints above, the first one is the desired absorption performance, which is calculated by the analytical model (**Eqs.2.1-2.5**). All the other constraints are geometric constraints, which are used to narrow the design space, as discussed in **Section 2.4.3**.

By parametrically sweeping M from 15 to 25, the overall thickness is found to reach the causally minimum thickness when $M = 19$.

2.5 Conclusions

This study analytically, numerically and experimentally studies a low-frequency broadband (50-63 Hz, one third octave band), high absorption (average absorption coefficient $\approx 93\%$), near-omnidirectional ($0^\circ - 75^\circ$) acoustic metasurface absorber composed of 4 coupled unit cells at a thickness of only 15.4 cm (1/45 of the wavelength at 50 Hz), in which the suitable assignment of lateral size to each unit cell plays a critical role in reducing the overall thickness. The interference coupling in the far field, the evanescent wave coupling, and the acoustic-structure interaction are discussed. Furthermore, to realize a broadband and near-perfect absorption at an optimal thickness, the lateral size of supercell and the number of unit cells in the supercell are also judiciously engineered.

Taking all these new degrees of freedom into account and with the assistance of GA, a causally optimal acoustic absorber, which is a broadband (50-100 Hz, one octave band), high-absorption (average absorption coefficient 85%), near-omnidirectional ($0° - 75°$) and deep-subwavelength (1/34 of wavelength at 50 Hz), is proposed. Our future work is to experimentally validate the proposed design for 50-100 Hz and further push the design of absorbers to the ideal one by means discussed in this study. We believe that our design philosophy, in which three degrees of freedom are proven to be critical in reaching a causally optimal thickness, would offer a gateway to designing broadband sound absorbers with different formats of unit cells (MPP, HRs, space-coiling structures, etc.) and to meet the long-standing need in room acoustics.

Chapter 3
Ultra-sparse Near-perfect Sound Absorbers in Two-port Systems

This chapter presents the study that was published in

- Ji, Jun, et al. "Ultra-sparse near-perfect sound absorbers." JASA Express Letters 3.3 (2023).

Some minor changes have been made to the text to better organize this work into the thesis. Furthermore, some figures have been rearranged and rescaled to match the single-column format of the thesis.

3.1 Background and Introduction

Noise control methods that rely on sound absorption/reflection while preserving ventilation is of great interest [87] for many occasions: automobile mufflers [88], room windows [89], sound barriers [90, 91, 92, 93] and cages [94, 95, 96], etc. In pursuit of ventilated sound absorbers, in particular, the conventional solution is to design an acoustic dissipative liner using fibrous materials [97], perforated panels with backing cavities [98, 99], or both [100]. However, these acoustic liners are often bulky and cannot achieve strong absorption, such as near-perfect absorption. Perfect absorption with a subwavelength structure [48] has been made possible recently by acoustic metamaterials [1] and acoustic metasurfaces [101] based on the enhanced local resonance and impedance matching. In fact, there is an intrinsic trade-off between the efficiency of sound absorption and ventilation [102], which means that a strong ventilation generally implies a poor absorption. For ducts or absorber arrays whose width or periodicity is limited to half wavelength, only the fundamental propagating mode exists and perfect absorption in such a scenario [40, 103, 104, 105, 106, 107] can be realized, either by harnessing a hybrid resonance composed of both monopole (symmetric) and dipole (anti-symmetric) resonances [40, 103], or by a pair of coupled resonances creating a 'soft' wall [104, 107, 108]. More recently, there is a trend to pursue a maximum periodicity under the condition of perfect absorption to advance the efficiency of ventilation. Lee et al. [109] derived an upper limit on the periodicity of a perfect absorber array, that is $2\lambda_0/\pi$, and demonstrated it with an absorber unit composed a pair of lossy and lossless resonators. Along this direction, Su et al. [110] extended the periodicity limit to $0.88\lambda_0$ by using a degenerate monopole and dipole resonances. Lapin [111] attempted the theoretical derivations of the periodicity for a perfect absorber array around two decades ago and showed that for a periodicity smaller than λ_0, the condition for perfect absorption of a plane wave incidence is to render degenerate monopole-dipole resonators critically coupled. However, no real-structure design has been presented to support this periodicity limit of λ_0. In this study, we analytically and numerically show an ultra-sparse absorber array with a periodicity of $d = 0.95\lambda_0$ achieving near-perfect (99%) absorption. Such an ultra-sparse near-perfect sound absorber array is realized with pairs of monopole-dipole resonators. Instead of using a highly coupled resonance by Su et al. [110], the capability to separately control the pair of monopole and dipole resonators helps the simultaneous realization of degeneracy and critical coupling for perfect absorption as the absorber array approaches the theoretical limit for the periodicity. With parameters of eigenfrequency,

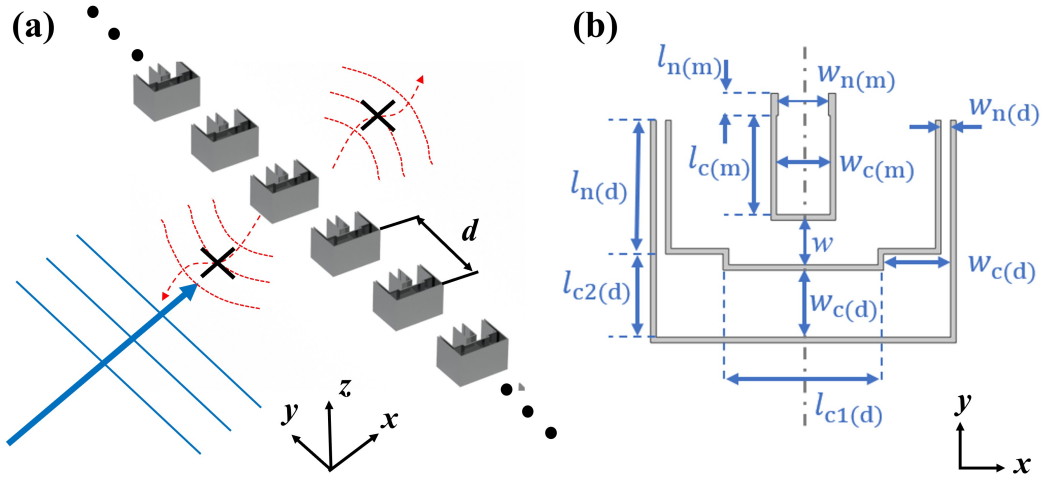

Figure 3.1. (a) 3D schematic of an ultra-sparse near-perfect absorber array. (b) Cross-sectional geometry of each unit cell of the array, which is composed of a Helmholtz Resonator as a monopole resonator and a space-coiled open-open tube as a dipole resonator. The vertical dash-dotted line in gray is the plane of mirror symmetry.

leakage loss, and dissipation loss being retrieved from Eigenfrequency study of COMSOL, the analytical calculation of absorption coefficient shows a good agreement with the numerical result.

3.2 Schematic and design

Figure 3.1(a) shows a 3D schematic of an ultra-sparse near-perfect absorber array for the frequency of interest f_0, which is considered to be 3000 Hz in this study. A plane wave normal to the array is incident along x direction. The periodicity of the array along y direction is $d = 0.95\lambda_0$. The array is uniform along z direction. Each unit cell of the array is composed of a monopole resonator and a dipole resonator, which can be characterized by their eigen frequency $f_{\mathrm{m/d}}$, leakage loss rate $\gamma_{\mathrm{m/d}}$, and dissipation loss rate $\delta_{\mathrm{m/d}}$ in Section 3.3. The coupling between two resonators is minimal and negligible, since the monopole and dipole resonators have opposite symmetry properties. **Figure 3.1**(b) shows the geometry for the unit cell in the x-y plane. The monopole resonator is realized by a Helmholtz Resonator, with neck length $l_{\mathrm{n(m)}}$, neck width $w_{\mathrm{n(m)}}$, cavity length $l_{\mathrm{c(m)}}$, and cavity width $w_{\mathrm{c(m)}}$. The dipole resonator is realized by a space-coiled open-open tube, with neck length $l_{\mathrm{n(d)}}$, neck width $w_{\mathrm{n(d)}}$, cavity length $l_{\mathrm{c1(d)}}$ and $l_{\mathrm{c2(d)}}$, and cavity width $w_{\mathrm{c(d)}}$. The monopole and dipole resonators are separated by a decent distance w to avoid a strong thermo-viscous loss in the channel region between the two resonators

so that the thermo-viscous loss exists in a controlled manner inside the resonators. The mathematical interpretation for the conditions of degeneracy and critical coupling is,

$$f_{\mathrm{m}} = f_{\mathrm{d}}; \delta_{\mathrm{m}} = \gamma_{\mathrm{m}}; \delta_{\mathrm{d}} = \gamma_{\mathrm{d}}. \tag{3.1}$$

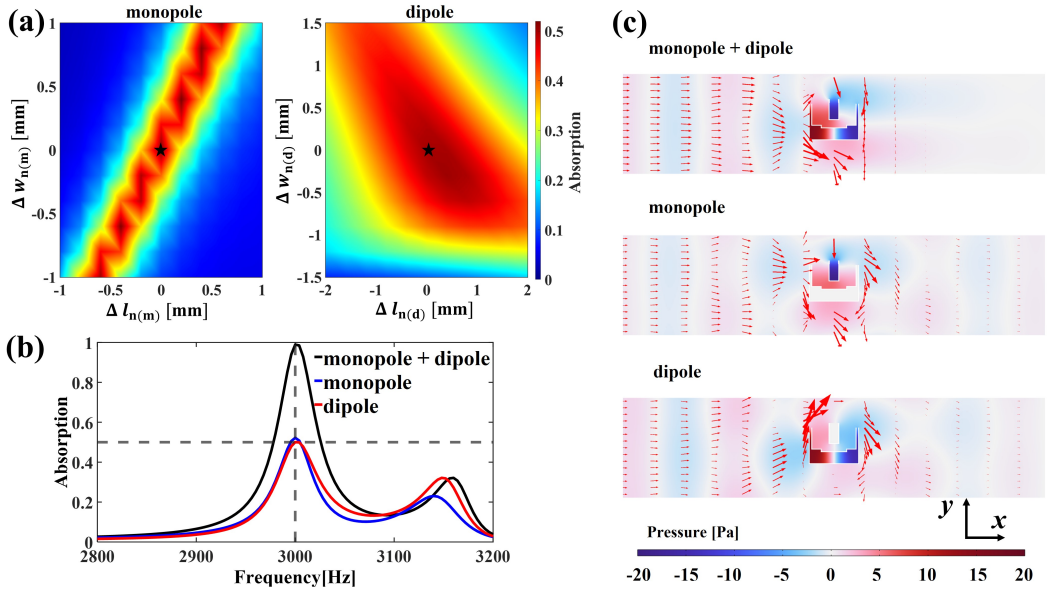

Figure 3.2. (a) Numerical absorption coefficient as a function of geometry modulation Δl_{n} and Δw_{n} for monopole (left) and dipole (right) resonators when the other resonator is closed. (b) Numerical absorption coefficient of the optimal design (marked as black stars in (a)) in frequency domain when both monopole and dipole (black curve), only monopole (blue curve), and only dipole (red curve) resonator is functional. (c) Numerically computed distributions of acoustic pressure (color) and acoustic intensity (arrow) at 3000 Hz in a unit cell with Floquet periodic boundary condition along y direction, when both monopole and dipole (top), only monopole (middle), and only dipole (bottom) resonator is functional. Magnitude of acoustic intensity is proportional to the size of arrow.

The geometric parameters of our absorber array listed in **Table. 3.1** comes from a two-step design strategy. With the required conditions in **Eq. 3.1**, an initial design is first brought up from an educated guess in which the monopole and dipole unit cell have a resonance frequency f_0. Then, Optimization module in COMSOL Multiphysics Version 6.0 is used with a target to maximize the absorption A at f_0. Geometric parameters including neck length, neck width, cavity length, and cavity width for the monopole and dipole resonators are set as design variables. The constraints include $A_{\mathrm{m/d}}$ >const. That is, the absorption for the monopole and the dipole is larger than a constant value. The efficiency of the optimization depends on the constant value, and we set it as 0.4. More details about COMSOL setup are discussed in the last paragraph of this section.

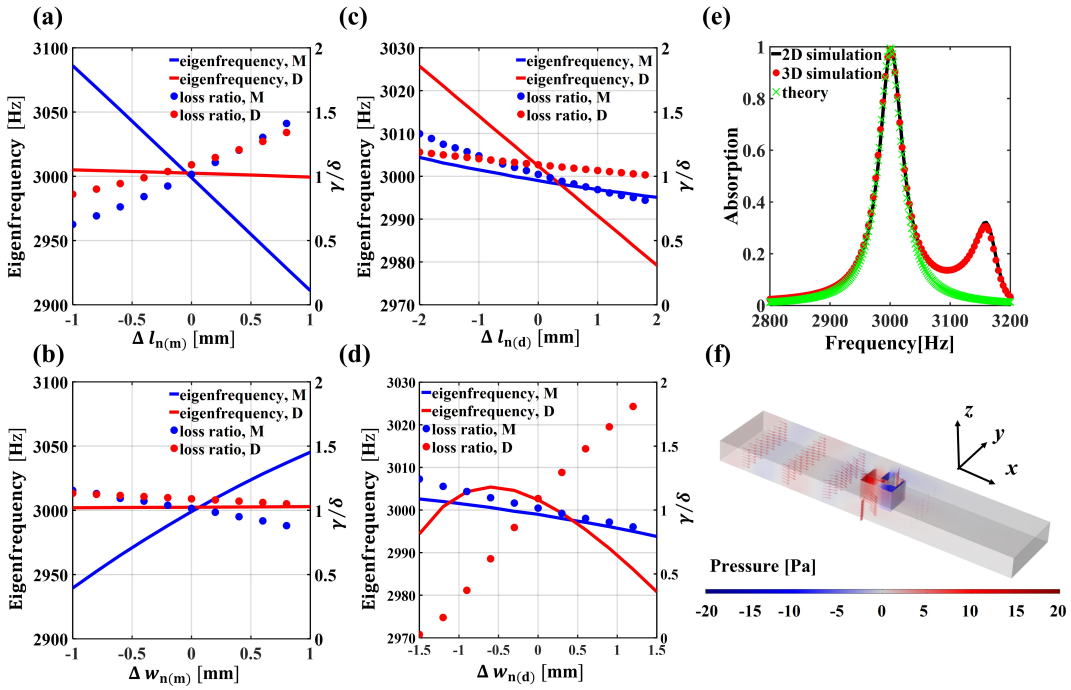

Figure 3.3. Numerical eigenfrequency and loss ratio as a function of geometry modulation (a) $\Delta l_{\mathrm{n(m)}}$, (b) $\Delta w_{\mathrm{n(m)}}$, (c) $\Delta l_{\mathrm{n(d)}}$, and (d) $\Delta w_{\mathrm{n(d)}}$. (e) Absorption coefficient of the optimal design in 2D numerical simulation, 3D numerical simulation and the couple mode theory. (f) 3D numerically computed distributions of acoustic pressure (color) and acoustic intensity (arrow) at 3000 Hz, when our designed absorber is extended 3.5 cm along z direction and put inside a 3D unit cell with Floquet periodic boundary condition along y direction. Magnitude of acoustic intensity is proportional to the size of arrow.

Different initial designs (e.g., resonators with difference neck widths and cavity widths but having the same resonant frequency f_0) from the educated guess are optimized until the total absorption reaches 99%.

Table 3.1. The geometric parameters of our design in **Figure 3.1**(b). The unit is in mm.

$l_{\mathrm{n(m)}}$	$w_{\mathrm{n(m)}}$	$l_{\mathrm{c(m)}}$	$w_{\mathrm{c(m)}}$	$l_{\mathrm{n(d)}}$	$w_{\mathrm{n(d)}}$	$l_{\mathrm{c1(d)}}$	$l_{\mathrm{c2(d)}}$	$w_{\mathrm{c(d)}}$	w
4	9	17.8	9.6	24	1.7	28.7	14.9	12	8

For ventilated absorbers without a rigid backing, at most 50% [112, 113] of the incident power can be absorbed if the absorber supports a single resonance for a single-sided incident wave. **Figure 3.2**(a) shows the numerical absorption coefficient as a function of geometry modulation Δl_{n} and Δw_{n} for our designed monopole (left) and dipole (right) resonator when the other resonator is closed. In other words, when studying the monopole behavior, the dipole is physically disabled, and vice versa. When Δl_{n}=0 and Δw_{n}=0, the

monopole and dipole resonators separately absorb around 50% absorption at 3000 Hz. In order to have a perfect absorption in such scenario, the absorber is designed to support both two resonances which are degenerate in frequency but have opposite symmetry with respect to the mirror plane of the system. As shown in **Figure 3.2**(b), absorption coefficient reaches 99% at 3000 Hz when both the monopole and dipole resonators are interacting with the incident wave. The absorption peak near 3150 Hz is resulted from an undesired mode when the periodicity is equal to one wavelength, which causes the absorption for the single resonance at 3000 Hz being a little bit larger than the maximum limit 50%. Similar to waveguide modes caused by periodically repeated rigid walls, this undesired mode is a general mode caused by the general periodic boundary condition. This undesired mode is also a roadblock to approaching the periodicity limit, since more than two modes are around the frequency of interest. Thus, to render degenerate monopole-dipole resonators critically coupled in a more extreme case, such as $d = 0.99\lambda_0$, is hard, and optimization on more than two degenerate modes is needed. **Figure 3.2**(c) shows the distributions of acoustic pressure in color and acoustic intensity using arrows at 3000 Hz. When both resonators are functional, both acoustic pressure and acoustic intensity are extremely weak on the transmission side (or right port). If only one of them is interacting with the incident wave, acoustic pressure and acoustic intensity can be visible on the right port, indicating the transmission of energy. The y component of acoustic intensity is strong near unit cells, which indicates the repetition of unit cells along the y direction and the scattering effect between them. The dipole resonator essentially is a one wavelength resonator, and acoustic pressure inside has the opposite symmetry to the monopole resonator with respect to the mirror plane of the system. Because of the space-coiling, the physical length of the dipole resonator along the x direction is around half wavelength and can be further shrunk for miniaturization purposes.

The numerical study in **Figures 3.2**(a-c) is conducted in COMSOL with Acoustic-Thermoviscous Acoustic Interaction, Frequency Domain module. The effect of the viscous friction and the heat transfer is concluded in the linearized compressible Navier–Stokes equation, the continuity equation, and the energy. Hard boundaries are imposed on the interfaces between air and 1 mm thick solid walls due to the large impedance mismatch between air and solid materials. No-slip and isothermal condition are applied at hard boundaries with boundary layer mesh. A normally incident plane wave with unit amplitude impinges along +x direction, and Floquet periodic boundary condition is applied along y direction to account for the scattering between unit cells and the fact that this is an array of resonators. The absorption coefficient can be calculated

by either the surface integral of the default variable ta.diss_tot in COMSOL (i.e., total thermos-viscous power dissipation density. W/m^3) or the line integral of the normal acoustic intensity of the reflected wave and transmitted wave.

3.3 Results and discussions

Eigenfrequency and the loss ratio (i.e., γ/δ) are retrieved using two sets of 2D Eigenfrequency study in COMSOL [114]. One set of Eigenfrequency study considers the thermo-viscous loss, in which the real part of the eigenfrequency $f_{\mathrm{m/d}}$ is the eigenfrequency and the imaginary part is $(\gamma_{\mathrm{m/d}} + \delta_{\mathrm{m/d}})/(2\pi)$. The other set of Eigenfrequency study does not consider the thermoviscous loss, in which the real part of eigenfrequency $f'_{\mathrm{m/d}}$ is larger than the eigenfrequency $f_{\mathrm{m/d}}$ and thus the imaginary part $\gamma'_{\mathrm{m/d}}/(2\pi)$ used for the leakage loss $\gamma_{\mathrm{m/d}}$ needs a revision by,

$$\gamma_{\mathrm{m/d}} = \frac{f_{\mathrm{m/d}}}{f'_{\mathrm{m/d}}}\gamma'_{\mathrm{m/d}}. \tag{3.2}$$

For both sets of Eigenfrequency study, Floquet periodic condition is applied along the y direction and plane wave radiation is applied at the two ports. **Figures 3.3**(a-b) show the numerical eigenfrequency and loss ratio as a function of monopole geometry modulation $\Delta l_{\mathrm{n(m)}}$ and $\Delta w_{\mathrm{n(m)}}$. $\Delta l_{\mathrm{n(m)}}$ and $\Delta w_{\mathrm{n(m)}}$ dominantly affect the eigenfrequency and loss ratio of the monopole mode. **Figures 3.3**(c-d) show that $\Delta l_{\mathrm{n(d)}}$ dominantly affects the eigenfrequency of the dipole mode, while $\Delta w_{\mathrm{n(d)}}$ dominantly affects the loss factor of the dipole mode. The capability to separately control the monopole and dipole resonators greatly facilitates the simultaneous realization of degeneracy and critical coupling for perfect absorption as the periodicity approaches the limit. Without varying any geometry, the designed monopole-dipole absorber is degenerate and critically coupled. Plugging the retrieved parameters into the equation derived from the coupled mode theory, [112] the absorption coefficient is,

$$A = \frac{2\delta_{\mathrm{m}}\gamma_{\mathrm{m}}}{(\omega-\omega_{\mathrm{m}})^2 + (\delta_{\mathrm{m}}+\gamma_{\mathrm{m}})^2} + \frac{2\delta_{\mathrm{d}}\gamma_{\mathrm{d}}}{(\omega-\omega_{\mathrm{d}})^2 + (\delta_{\mathrm{d}}+\gamma_{\mathrm{d}})^2}. \tag{3.3}$$

The theoretical prediction has a great agreement with both 2D and 3D simulations near 3000 Hz, as shown in **Figure 3.3**(e). The 3D simulation is conducted with our designed absorber being extended 3.5 cm along z direction and **Figure 3.3**(f) shows a 3D distribution of acoustic pressure (color) and acoustic intensity (arrow) at 3000 Hz. The discrepancy between the theoretical model and numerical models is because the

modes near 3150 Hz are not considered in the theory.

It should be pointed out that, such an ultra-sparse near perfect absorber is designed at the cost of being sensitive to the angle of incidence as shown in **Figure 3.4**. The absorption coefficient drops significantly as the oblique incident angle increases to 4°. To mitigate this issue, one could use rigid walls as a special kind of periodic condition instead of the Floquet periodic boundary condition, which is what we are using now in the numerical model. This would render the problem an absorption problem in a waveguide with only a few propagation modes, i.e., discrete incident wave components. In addition, porous materials with high dissipation loss could be used to broaden the absorption bandwidth to make the design less sensitive to the incident angle.

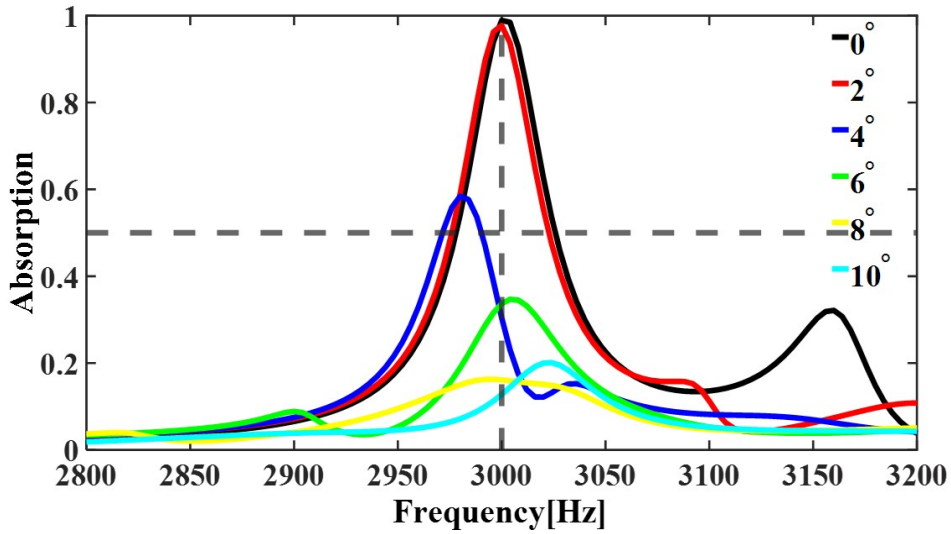

Figure 3.4. Absorption coefficient as a function of frequency and the angle of incidence in 2D numerical simulations.

3.4 Conclusions

In this study, we analytically and numerically show that an ultra-sparse absorber array with a periodicity of $d = 0.95\lambda$ can achieve near-perfect (99%) absorption at the designed frequency f_0. Such an ultra-sparse near-perfect sound absorber array is realized with an array of monopole-dipole paired resonators. By separately controlling the monopole and dipole resonators, simultaneous realization of degeneracy and critical coupling which are crucial for perfect absorption can be realized as the absorber array approaches the limit for the periodicity. With parameters of eigenfrequency, leakage loss, and dissipation loss

being retrieved from Eigenfrequency study of COMSOL, the analytical calculation of absorption coefficient yields a good agreement with numerical results in both 2D and 3D. The sparse-resonator-based sound absorber could greatly benefit noise control with ventilation and the results of this study could have implications for electromagnetic wave absorbers because of similarities in wave physics [112] governed by the coupled mode theory.

Chapter 4
Broadband Acoustic Radiation Enhancement Using Acoustic Metamaterial

This chapter presents the study that was published in

- Ji, Jun, et al. "Metamaterial-Augmented Head-Mounted Audio Module." Advanced Materials Technologies (2023): 2300834.

Some minor changes have been made to the text to better organize this work into the thesis. Furthermore, some figures have been rearranged and rescaled to match the single-column format of the thesis.

4.1 Background and Introduction

Advancements in audio modules have led to the development of successful consumer electronics products such as loudspeakers, cellphones, headphones and smart speakers. More recently, as a crucial component of head-mounted devices (HMDs), audio module quality plays a significant role in augmented reality (AR) or virtual reality (VR) experiences. These products revolutionize how humans make immersive interaction with surroundings [115] in several domains such as entertainment, health care, [116] and education. [117] Audio radiation, which is commonly used in conjunction with visual displays and other sensors, is one of the major interfaces that humans use to communicate with HMDs. However, the radiation performance of these devices has reached a plateau in recent years. Improving loudness or power efficiency without increasing the device's size remains to be extremely challenging. This is due to the fact that the power of a monopole source radiated to the far field is proportional to $(D/\lambda)^2$ (D is the diameter and λ is the wavelength). With the trend of miniaturization for HMDs, the power budget is very limited (a small battery), and the audio radiation module is confined to a small space where low-frequency radiation is even more challenging. There is an increasing need for a compact audio module that can produce a high sound pressure level while consuming low power, particularly at low frequencies ranging from 20 Hz to 1 kHz. It has been shown [118] that the bass frequencies (below 100 Hz) contributed to the largest increase of loudness in popular music recordings over time. Additionally, the octave band centered around 500 Hz is a major part of the long-term average spectrum of speech, [119] which pertains to speech intelligibility and various audiological applications.

Typical audio module designs are electrical-mechanical-acoustical coupled systems consisting of transducers, front and back acoustical cavities, and surrounding environments. Examples of classical loudspeaker designs include closed boxes, [120] vented boxes, [121] horns, [122] and transmission line. [123, 124] Recently, some folded transmission line designs [125, 126] and folded waveguide (e.g., Bose's Acoustic Waveguide speaker technology) have been used for improving the radiation performance of small audio devices. These concepts are interesting, and the acoustic domain and transducer domain has been connected using equivalent circuit method. However, in previous studies, the acoustic structural resonance and transducer resonance were nearly independent, leading to an intrinsically weak coupling between the two resonances and thus suboptimal designs especially at low frequencies.

Acoustic metamaterials [1] are artificial structures that are capable of controlling the

propagation of sound in unconventional ways, and have led to interesting phenomena such as acoustic cloaking [127, 15, 128], acoustic subwavelength imaging [17, 34, 18], acoustic rainbow trapping [129, 69], and acoustic unidirectional transparency [25, 130]. However, most acoustic metamaterials are designed in a way that makes it challenging for them to have a direct and immediate impact on real-world applications pertaining to the audio industry, with one possible exception being sound absorption [48]. On the one hand, despite the reduction of audio distortion [131] realized by the mitigation of high-frequency acoustical cavity-resonances through the addition of acoustic metamaterial-based absorbers in loudspeaker enclosures, the attempt to incorporate passive acoustic metamaterials [132, 114, 133, 134, 135, 136, 137, 138] into the loudspeaker designs has seen very limited radiation enhancement at low frequencies due to the bulky size and the lack of consideration on the metamaterial-transducer coupling. On the other hand, though active acoustic metamaterial may offer a solution to a broadband radiation enhancement [139], they often involve designs that are complicated to avoid instability and also require more power consumption.

This study proposes a metamaterial-transducer resonant coupling, by carefully designing coiled acoustic metamaterials (CAMM) inside a head-mounted acoustic module, to enhance the sound radiation performance (both loudness and power efficiency) without changing the transducer or the overall exterior enclosure dimensions, which is generally a challenging requirement for product development in the audio industry. In contrast to previous studies, the resonant coupling effect between the transducer and metamaterial resonances is utilized as a critical tool to achieve the improvement of voltage sensitivity (dB SPL re 0.1 Vrms input excitation). We numerically show that, though the metamaterial resonance frequency is around 600 Hz, a properly tuned metamaterial-transducer resonant coupling can lead to sound enhancement at a much lower frequency (100 Hz) close to the transducer resonance, which is the key to achieving broadband sound enhancement. We prototyped the design using 3D printing and validated the simulation results using free field measurements, where good agreements between the measured and simulated voltage sensitivity, excursion (the displacement of the diaphragm), electrical impedance, and power sensitivity (SPL re 0.1 W) are achieved. Finally, we recorded the audio output by mounting the audio module with CAMM on a head and torse simulator (HATS). The results showed 3 dB improvements at 100 Hz and 2.5 dB RMS improvements when using a male speech as input, and 2.6 dB improvements at 117 Hz and 0.8 dB RMS improvements when using a music song as input. It is important to note that although these improvements may seem moderate, they are actually significant by

industrial standards. These results collectively demonstrate the substantial improvement of the sound radiation from the transducer to acoustic domain enabled by acoustic metamaterials.

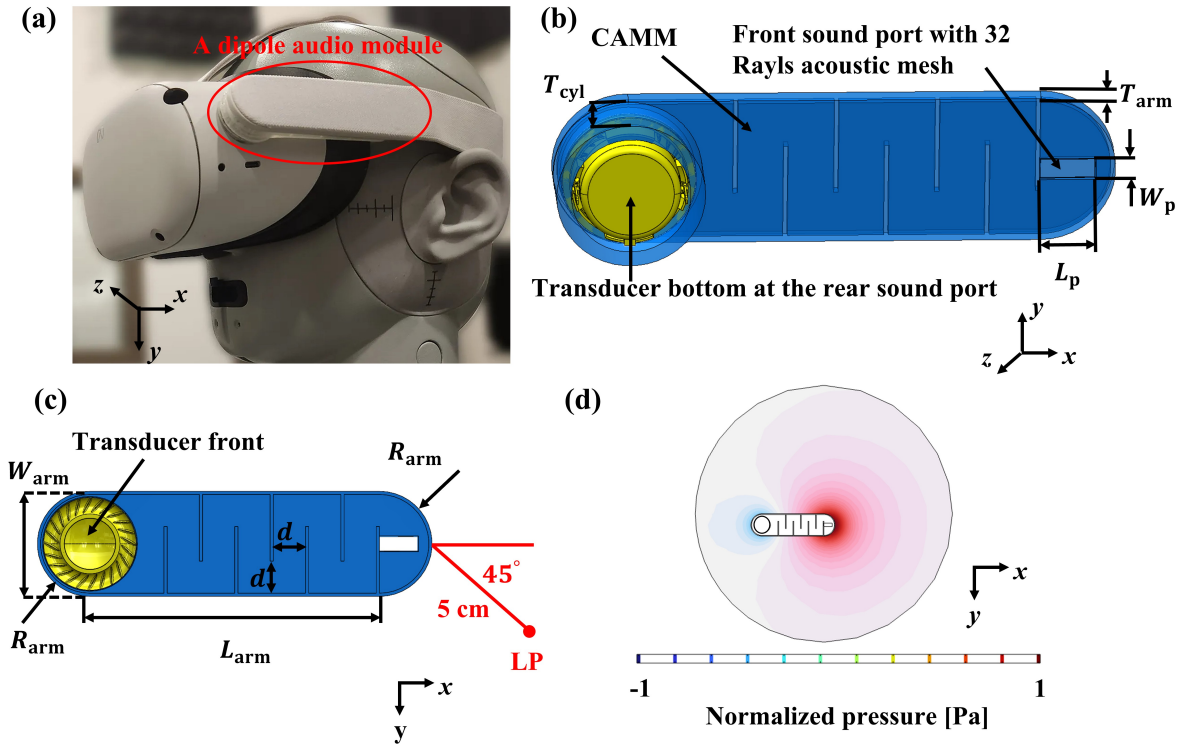

Figure 4.1. (a) A dipole audio module on a HMD (a VR device called Quest 2). (b) 3D, (c) 2D schematics of the dipole audio module with CAMM, (d) The normalized pressure distribution of the dipole configuration outside the audio module on the plane z =0.

4.2 Structure Design of CAMM

4.2.1 Schematic of a dipole audio module

A dipole source is typically employed to maximize audio output at the user's ears located at the near field and reduce the far field audio signal leakage (for privacy concerns) towards people around the user of HMD [140]. **Figure 4.1**a shows that a representative dipole audio module is located at the 'arm' of a commercial HMD (i.e., a VR device Quest 2). **Figure 4.1**b depicts a 3D schematic of the audio module, comprising a flat waveguide and a cylindrical shell where a customized and well-characterized moving-coil transducer (See **Section 4.4.4** for details) is mounted. The transducer is located further

away from the ear due to industrial design constraint for Quest 2, and the flat waveguide is used to direct sound from the transducer to a sound port (which is defined as the front port) as close as possible to the ear location. The waveguide is normally empty and thus provides a natural harbor for the installation of acoustic metamaterials. The sound port, which is situated at the left-hand side of the waveguide as shown in **Figure 4.1**b, emits the sound that originates from the bottom of the transducer and is referred to as the rear port. While one end of the shell is connected to the waveguide, the other end is connected to the main body (e.g., the optical display) of the HMD, as shown in **Figure 4.1**a. The cylindrical shell has a thickness of $T_{cyl} = 11.8$ mm, an inner radius of $R_{in} = 10.43$ mm and an outer radius of $R_{out} = 13$ mm. The thickness of the waveguide is $T_{arm} = T + 2t$, where T is the inner thickness and t is the wall thickness 0.8 mm. The cross-sectional view of the waveguide is presented in **Figure 4.1**c, where the mechanical outline is a rectangle ($L_{arm} \times W_{arm} = L_{arm} \times (W + 2t)$ =72 mm × (24.6 mm + 2×0.8 mm)) with two semi-circles ($R_{arm} = R + t$ =12.3 mm + 0.8 mm). The front sound port ($L_p \times W_p$ =9.5 mm ×3.5 mm) is covered by a thin layer of acoustic mesh with an impedance of 32 Rayl. A particular point of interest throughout this study is located at a distance of 5 cm and an angle of 45 degrees from the front sound port, on the same plane (z =0), where a microphone is placed. This location is defined as the listening position (LP) where the radiation performance is targeted to be enhanced. The radiation from the front and rear sound ports behaves approximately as a dipole, as evidenced by the wave field illustrated in **Figure 4.1**d.

Table 4.1. TS parameters of the moving-coil transducer from Klippel LPM measurements

Name	Value	Unit
R_e	3.15	ohm
L_e	0.025	mH
R_m	0.115	kg/s
M_m	0.254	g
C_m	2.602	mm/N
BL	1.011	N/A
A	2.77	cm^2
f_s	195.7	Hz

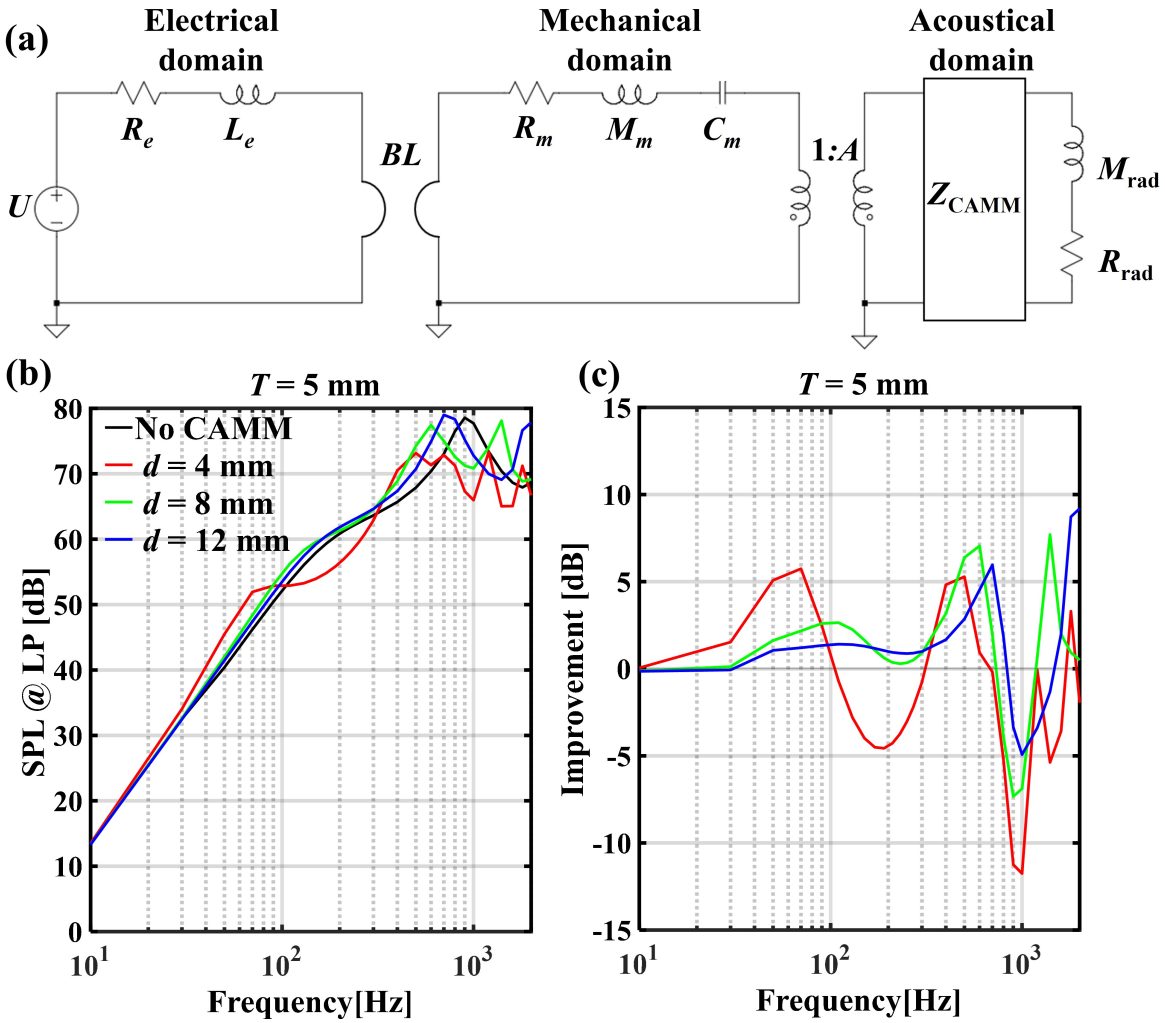

Figure 4.2. (a) Block diagram of the audio module, only the front port with CAMM is included. (b) Numerical voltage sensitivity of the audio module, when coupled resonances, which are induced by CAMM at different partition distances d, are introduced into an empty waveguide with a thickness of $T = 5.0$ mm. (c) The improvement of voltage sensitivity compared with the empty waveguide at $T = 5.0$ mm.

4.2.2 Simulations

We begin with an audio module with an empty waveguide at a thickness of T =5.0 mm and conduct numerical simulations utilizing COMSOL Multiphysics 6.0, a finite element analysis (FEA) software. The simulation utilizes an equivalent circuit method (ECM) [141] to simulate the electrical-mechanical domain of the electromagnetic transducer and calculate the speaker diaphragm displacement as an input to the thermoacoustic domain of the front and back cavities as well as the surrounding air in the far field, in order to compute the radiated sound pressure. **Figure 4.2**a illustrates the ECM model for the

audio module. The electrical domain is modeled using an inductor L_e and resistor R_e, while the mechanical domain is represented by the mechanical resistance R_m, moving mass M_m, and mechanical capacitor C_m. A gyrator with a force factor of BL couples the electrical and mechanical domains. Notably, R_m, C_m, and BL, which are typically nonlinear, [141] are considered constants (linear approximation) for this study as shown in **Table 4.1** (See **Section 4.4.4** for details), as a small voltage input signal 0.1 Vrms is utilized to ensure linearity. The coupling effect of the mechanical and acoustical domains is modeled as a transformer with the effective radiation area A of the diaphragm. SPL (i.e., $20\log_{10}(p_e/p_{ref})$, $p_{ref} = 2 \times 10^{-5}$ Pa) at LP is marked in black in **Figure 4.2**b as a benchmark. SPL is substantially affected by two resonances at low frequency range of interest, i.e., transducer resonance and waveguide resonance. The transducer resonance is $f_s = 195.7$ Hz, which can be calculated by $(2\pi \times \sqrt{C_m \times M_m})^{-1}$. The waveguide resonance is $f_w = 900$ Hz, which is a quarter wavelength resonance approximated by $f_w = c_0/(4 \times L_{eff})$, [126] where L_{eff} is the effective acoustic propagation length from the diaphragm to the front sound port. Below the transducer resonance, voltage sensitivity at LP rolls off 12 dB per octave because the radiated pressure is proportional to the square of frequency. Between the transducer resonance and the waveguide resonance, voltage sensitivity is normally independent of frequency for an empty waveguide.

With the introduction of the CAMM inside the flat waveguide, the resonant frequency of the waveguide gets closer to that of the transducer and the resonant coupling between them must be taken into consideration. Under this scenario, a delicate balance is necessary to resolve the competition between needing a lower waveguide resonance frequency and a smaller added mass on the transducer resonance, both of which can lead to improved sound radiation at lower frequencies. The CAMM is illustrated in **Figure 4.1**b, which introduces a coiled channel in the waveguide characterized by a partition distance d, to effectively increase the physical length of wave propagation path without changing the waveguide volume. A parametric study of different partition distances $d = 4$ mm, 8 mm, and 12 mm is utilized to demonstrate the coupling effect, with SPL shown in **Figure 4.2**b and the differences between CAMM designs and the benchmark shown in **Figure 4.2**c. A lower waveguide resonance frequency can be obtained as the partition distance d becomes smaller, since L_{eff} increases due to the smaller partition distance under a fixed waveguide space. However, voltage sensitivity around the transducer resonance may not benefit from CAMM with a smaller d. For a small d of 4 mm, **Figure 4.2**b indicates that the sensitivity drops above the transducer resonance, even though the sensitivity is improved below the transducer resonance. Treated as a single Degree-of-Freedom

forced vibration problem, the frequency region right above the transducer resonance is a mass-controlled region. In this region, as the added mass from CAMM (approximated by $M_a = (\rho_0 l_{eff} A)/(dT)^2$ increases because of a decrease in d, the excursion and SPL frequency response decrease. It was found that an optimal partition distance of 8 mm achieves a continuous and broadband (20 Hz – 700 Hz) enhancement of the voltage sensitivity, with peaks of 2.6 dB at 100 Hz and 7.1 dB at 600 Hz. It is important to note that unlike the conventional vented box design [121] which normally introduces a resonance lower than the transducer resonance to extend the bass response, resulting in a bulky size, our CAMM design introduces a resonance above the transducer resonance.

A dipole model is used to further understand how metamaterial-transducer resonant coupling can boost radiation in a continuous and broadband manner, especially at a lower frequency (the transducer resonance) by employing a structure with a higher resonance frequency (CAMM resonance). **Figure 4.3**a-c show the near field frequency response in the acoustic domain at different locations (at a distance of 0.5 cm from the front port, at a distance of 0.5 cm from the rear port and at LP) for three different designs. These include the benchmark design ($T = 5.0$ mm without CAMM, denoted as WG50), improperly coupled resonances ($T = 5.0$ mm and $d = 4$ mm, denoted as CAMM50_4mm), and properly coupled resonances ($T = 5.0$ mm and $d = 8$ mm, denoted as CAMM50). **Figure 4.3**d shows the pressure phase difference between the front port and the rear port (referred to as phase difference throughout the study for simplification). It can be observed that SPL at LP is highly correlated (similar shape for the SPL curves) to the front port since the LP is closer to the front port than the rear port. It can also be observed that the phase difference turns from 180 degrees to 0 degree when the working frequency goes from a frequency below the transducer resonance to the waveguide resonance, which induces a smaller cancellation between two sound ports and consequently a larger SPL at LP. Based on these two observations, we will show that SPL at the front port and phase difference between the two ports are two major contributing factors to the voltage sensitivity enhancement at LP near both the transducer resonance and waveguide resonance. Let us first focus on the voltage sensitivity near the transducer resonance. On the one hand, the properly designed CAMM has a 1.4 dB improvement on the front port SPL compared with the benchmark (from 81.8 dB to 83.2 dB) at 100 Hz, which is one factor contributing to the overall enhancement of 2.6 dB (from 52.1 dB to 54.7 dB) at the LP at 100 Hz. On the other hand, the properly designed CAMM introduces a slightly different phase difference compared with the benchmark (from 176° to 175.5°) at 100 Hz, resulting in a smaller dipole cancellation, which is the

other factor contributing to the enhanced SPL at the LP. Note that instead of directly employing a structure resonating at 100 Hz, such a radiation enhancement of 2.6 dB at 100 Hz, which is due to the metamaterial-transducer resonant coupling from a 600 Hz metamaterial resonator, has never been reported and can prove valuable for the audio industry. Next, let us focus on the voltage sensitivity near the waveguide resonance. For the properly designed CAMM, as the magnitude of the front port response reaches a peak and the phase difference becomes 0 degree, the audio module is transformed from a quasi-dipole to an efficient monopole radiator, as confirmed by the peak of SPL at LP. If the metamaterial-transducer resonant coupling is improperly designed such as CAMM50_4mm, there is a significant drop of SPL at the LP between the transducer resonant frequency and metamaterial resonant frequency (100 Hz – 600 Hz), which is primarily caused by the drop of SPL from the front port. Based on the analysis of a single Degree-of-Freedom forced vibration, acoustic pressure radiated from the transducer right above the transducer resonant frequency is inversely proportional to the added mass from CAMM (approximated by $M_a = (\rho_0 l_{eff} A)/(dT)^2$. Thus, the excessive added mass from CAMM50_4mm on the transducer resonance is responsible for the drop of SPL at the LP for the improperly coupled resonance design.

4.3 Results and discussions

4.3.1 Measured Radiation Enhancement induced by CAMM in free field

In this section, we use comprehensive analyses and experiments to demonstrate the coupled resonances that complement the acoustic domain analysis presented in the previous sections. **Figure 4.4**a and **Figure 4.4**b depict the experimental setups for measuring voltage sensitivity and excursion in free field (See Numerical and Experimental Methods for details). **Figure 4.4**c and **Figure 4.4**d illustrate the comparisons between simulations and measurements of voltage sensitivity and excursion, respectively. The measurement is in good agreement with the simulation. In **Figure 4.4**c, CAMM50 achieves a broadband (50 Hz – 700 Hz) enhancement of output SPL with constant voltage excitation compared to WG50, with peaks of 2.6 dB (3.1 dB) at 100 Hz (95 Hz) and 7.1 dB (7.1 dB) at 600 Hz (500 Hz) in simulations (experiments). The full spectrum measured from 20 Hz to 20 kHz is shown in **Section 4.4.3**, and useful measurements start around 50 Hz because of the background noise at low frequencies. The enhancement

of radiation in the acoustic domain at these two peaks is due to an enhanced excursion under the same voltage, which is caused by metamaterial-transducer resonant coupling, as shown in **Figure 4.4**d. The measurement of total harmonics distortion shows that CAMM does not introduce a strong distortion to the signal (**Section 4.4.6**).

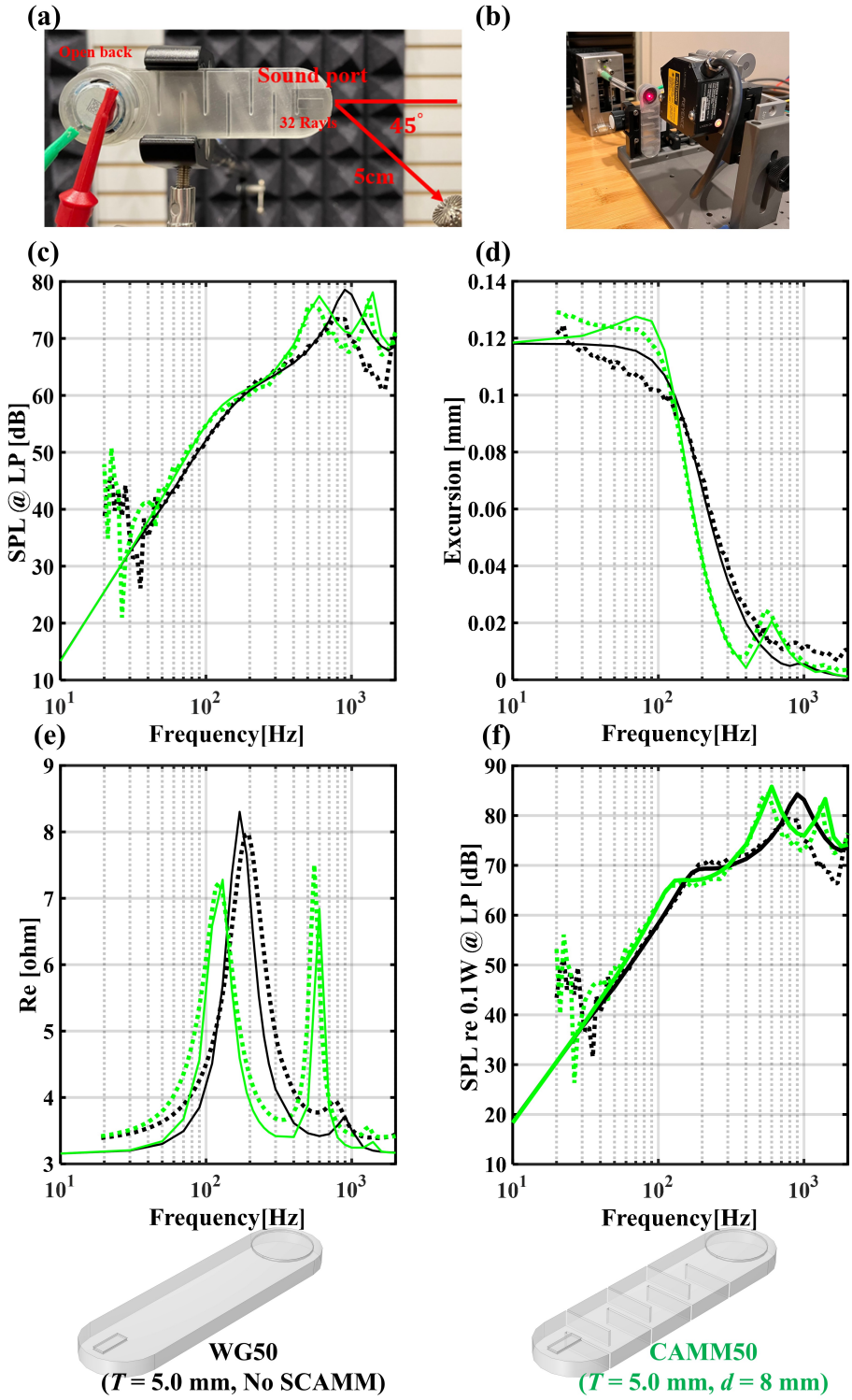

Figure 4.3. Numerical results of the dipole response for WG50 (black), CAMM50_4mm (red), and CAMM50 (green). The voltage sensitivity at three locations: (a) at a distance of 0.5 cm from the front port, (b) at a distance of 0.5 cm from the rear port and, (c) LP. (d) shows the pressure phase difference between the front port and rear port.

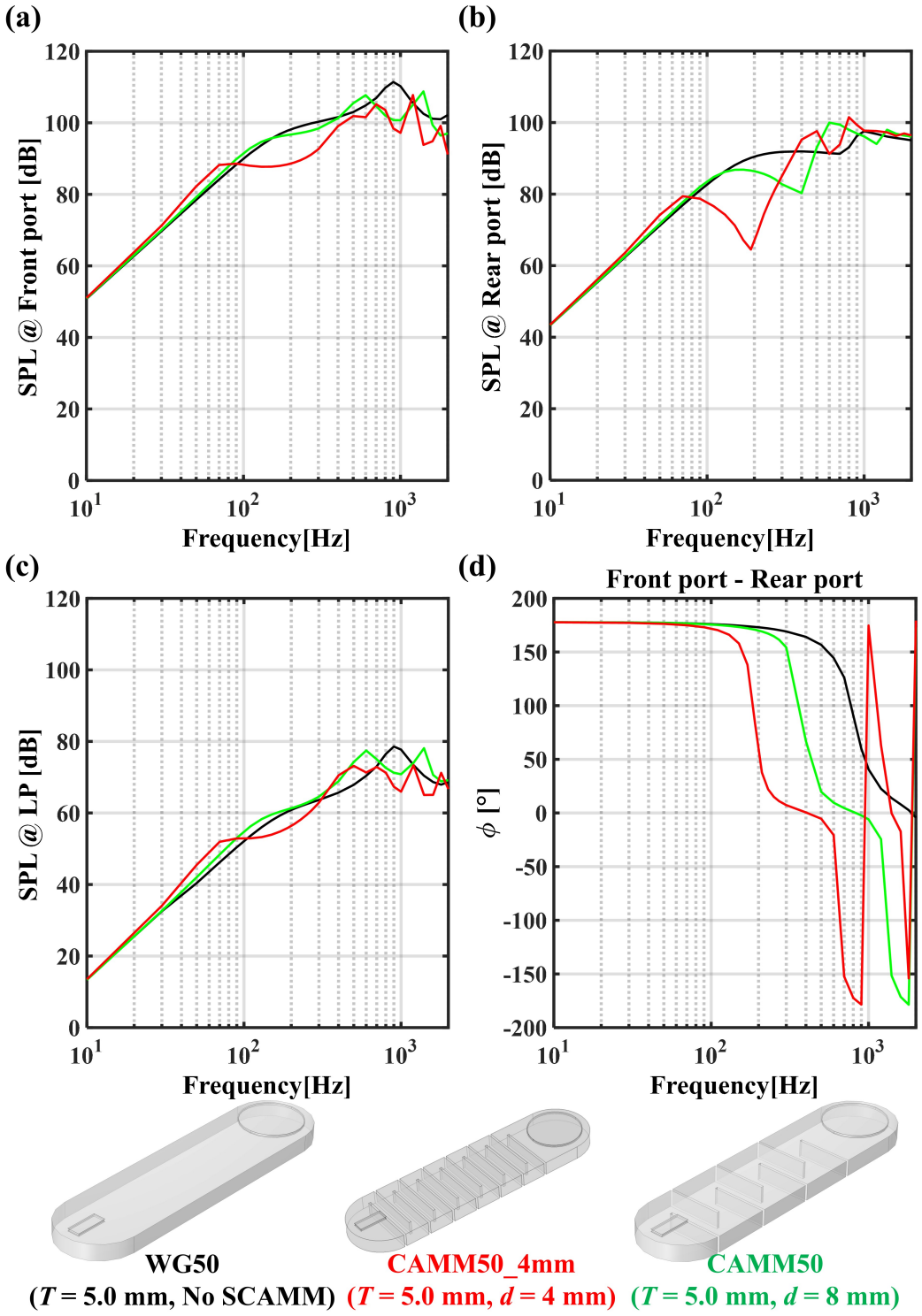

Figure 4.4. Photograph of measuring (a) voltage sensitivity and (b) excursion and electrical impedance of the audio module in free field under 0.1 Vrms. Measurements (dash lines) and simulations (solid lines) of (c) voltage sensitivity at LP, (d) excursion at the center of the speaker diaphragm, (e) the real part of the electrical impedance, and (f) power sensitivity per 0.1 W at LP for WG50 (black) and CAMM50 (green).

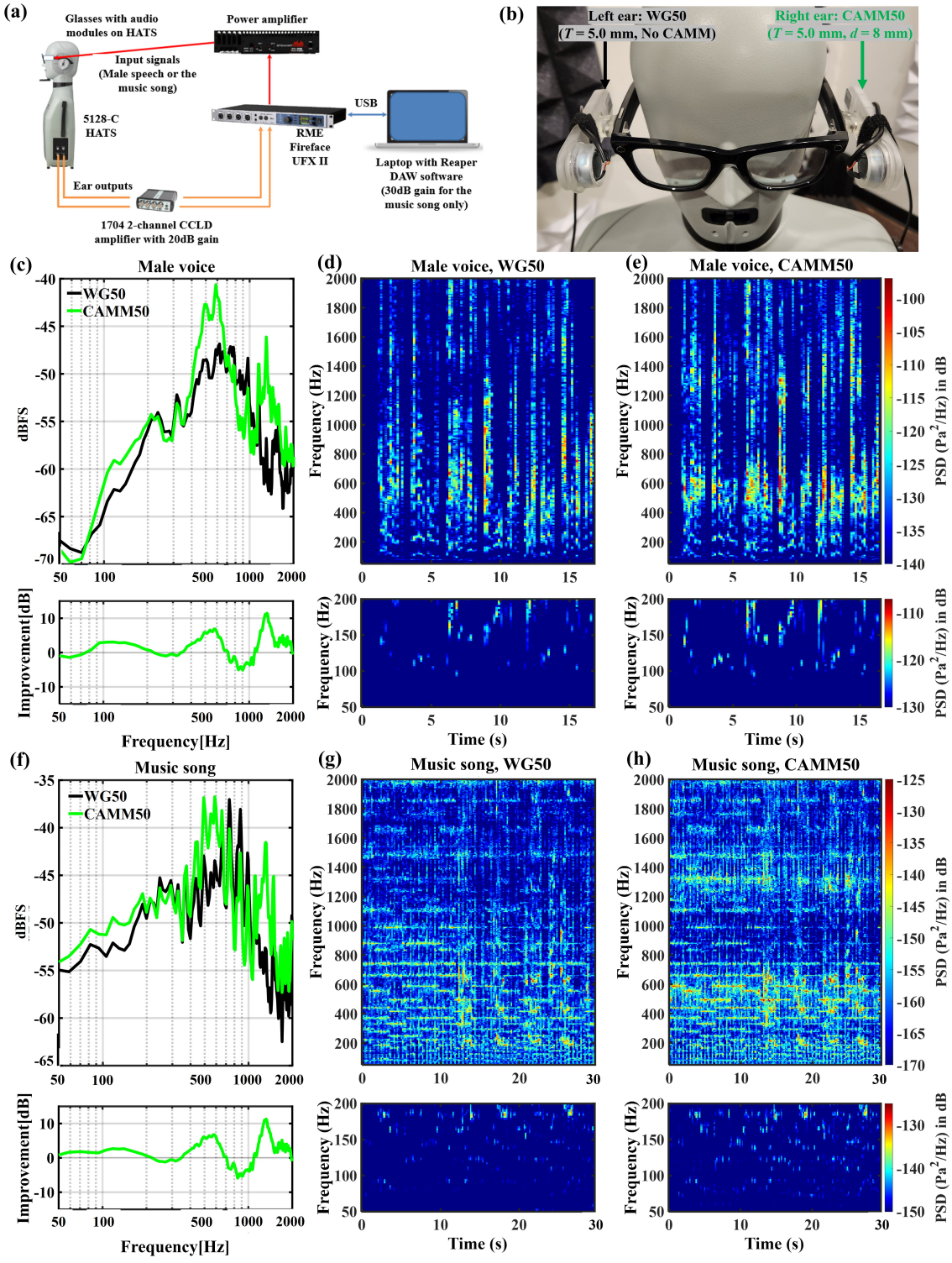

Figure 4.5. (Caption on the next page.)

Figure 4.5. (a) Schematic of measuring the voltage sensitivity on HATS when (b) WG50/CAMM50 is mounted on the left/right ear under 0.1 Vrms excitation voltage. Measured digital signals for the voltage sensitivity using in-ear microphone when (c) male voice signals and (f) a music signal are played by WG50 (black) and CAMM50 (green). Improvement of the voltage sensitivity compared with WG50 for the male voice signals and the music signal are plotted in the figures right below the voltage sensitivity. For the male voice signals, the spectrogram of WG50 and CAMM50 are shown in (d) and (e) from 50 Hz to 2000 Hz using the same colormap (-140 dB to -97 dB). A close-up view with another colormap range (-130 dB to -107 dB) is plotted for WG50 and CAMM50 right below to show the enhancement from 50 Hz to 200 Hz. For the music signal, the spectrogram of WG50 and CAMM50 are shown in (g) and (h) from 50 Hz to 2000 Hz using the same colormap (-170 dB to -125 dB). A close-up view with another colormap range (-150 dB to -125 dB) is plotted for WG50 and CAMM50 right below to show the enhancement from 50 Hz to 200 Hz.For the music signal, the spectrogram of WG50 and CAMM50 are shown in (g) and (h) from 50 Hz to 2000 Hz using the same colormap (-170 dB to -125 dB). A close-up view with another colormap range (-150 dB to -125 dB) is plotted for WG50 and CAMM50 right below to show the enhancement from 50 Hz to 200 Hz.

Power sensitivity is another important metric for audio modules, particularly for power-constrained devices. **Figure 4.4**e and **Figure 4.4**f demonstrate the real part of electrical impedance and power sensitivity in both simulations and experiments, respectively. Power sensitivity can be derived as SPL re 0.1W = SPL re 0.1V + 10log10(Re), where Re is the real part of the electrical impedance. By adding the CAMM into the waveguide, two positive effects are imposed on the real part of the impedance as shown in **Figure 4.4**e: the overall impedance profile shifts to a lower frequency, and a larger real part of impedance is induced at the waveguide resonance. Because of the redshift of the real part of impedance and the enhancement of voltage sensitivity around 100 Hz shown in **Figure 4.4**c, power sensitivity of CAMM50 also achieves a broadband (50 Hz – 800 Hz) enhancement (except a few dB loss near 200 Hz) compared to WG50, with peaks of 4.2 dB (4.2 dB) at 100 Hz and 10.1 dB (9.4 dB) at 600 Hz (560 Hz) in simulations (experiments).

4.3.2 Measured Radiation Enhancement induced by CAMM on HATS

In addition to measuring audio output in free field, we have also conducted experiments in which we mounted the WG50 and CAMM50 modules in a pair of glasses to simulate a HMD, as shown in **Figure 4.5**b. Then we mount the glasses on a HATS and measure audio output from the eardrum reference point (DRP) using in-ear microphones, as shown in **Figure 4.5**a. We play both male voice signals and music signals to the WG50 and CAMM50 prototypes separately using 0.1 Vrms flat excitation without equalization

(EQ). For the first example, the standard recording of Harvard Sentences according to the IEEE standard[142] from a male speech is played, which represents discrete and low-frequency sound. As shown in **Figure 4.5**c, the measured digital signals (with 0 dB full scale (dBFS) representing the maximum value of 1) show that our CAMM50 achieves a continuous and broadband (80 Hz – 700 Hz) enhancement of voltage (except less than 1 dB loss near 200 Hz) compared to WG50, with improvement peaks of 3 dB at 100 Hz and 6.9 dB at 570 Hz, and 2.5 dB RMS improvement in the time domain. As shown in **Figure 4.5** and **Figure 4.5**e, the spectrograms of WG50 and CAMM50 from 50 Hz to 2000 Hz demonstrate the radiation enhancement as the signal varies in time. More signals marked in deep red indicate an enhancement for the frequency bands of 400 Hz to 700 Hz and 1100 Hz to 1400 Hz. A close-up view of the lower frequency range (50 Hz - 200 Hz) is plotted for WG50 and CAMM50, with more signals marked in green and yellow indicating the enhancement. For the second example, a music is played and **Figure 4.5**f shows that our CAMM50 again achieves a continuous and broadband (50 Hz - 700 Hz) enhancement of the voltage sensitivity (except around 1 dB loss near 200 Hz) compared with WG50, with improvement peaks of 2.6 dB at 117 Hz and 6.7 dB at 586 Hz, and 0.8 dB RMS improvement in the time domain. Similarly, the spectrograms of WG50 and CAMM50 in **Figure 4.5**g and **Figure 4.5**h suggest a radiation enhancement in the frequency bands of 60 Hz – 200 Hz, 300 Hz – 700 Hz, and 1200 Hz – 1800 Hz, with more signal points marked in red and yellow indicating enhancement. The measurement of total harmonics distortion shows that CAMM does not introduce a strong distortion to the signal (**Section 4.4.6**). The slightly lower improvement in the music sound compared to the male voice is due to the concentration of higher frequencies in the music, which are less enhanced by the current audio module design. The enhanced radiation measured on HATS confirms that the CAMM offers a promising solution for HMD improvement and could potentially have an immediate impact on the audio industry.

4.4 Methods

4.4.1 Numerical Simulations

3D numerical simulations are carried out by the commercial finite element software COMSOL Multiphysics v6.0. The electrical and mechanical domains are modeled in Electrical Circuit module using TS parameters measured by Klippel R&D as shown in Table 1. The acoustic domain is modeled in Pressure Acoustics and Thermoviscous

Acoustics to accurately account for the thermoviscous boundary loss. The coupling between the electrical domain and the mechanical domain is realized by "Current-Controlled Voltage Source" feature under Electrical Circuit, while the coupling between the mechanical domain and the acoustic domain is realized by "Interior Lumped Speaker Boundary" feature under Pressure Acoustics. In the low-frequency regime of interest, the movement of the transducer diaphragm is approximated as a rigid piston. The frameworks of the acoustic module are modeled as acoustically rigid. The background medium is air with mass density $\rho_0 = 1.21$ kg/m^3 and sound velocity $c_0 = 343.2$ m/s. Perfectly matched layers are imposed on the outer boundaries to eliminate sound reflections. The thin layer of acoustic mesh 32 Ralys is modeled using 'Interior Normal Impedance' feature under Thermoviscous Acoustics module, with the normal impedance set as 32 "Pa· s/m" , slip tangential velocity, and isothermal thermal condition. To ensure the accuracy of simulation, a mesh independent test is carried out. Numerical solutions converge, when the largest element size is set as 1/6 of the smallest working wavelength, the number of boundary layer is set as 6, and the thickness of first layer is set as 1/5 of the viscous boundary layer thickness.

4.4.2 Fabrication and assembly of the audio module

The CAMM sample was fabricated using Clear Resin through Form 3+ printer, which utilizes Low Force Stereolithography (LFS) and provides a nominal precision of 25 µm. Loctite vinyl plastic and fabric adhesive was used to assemble the transducer to the 3D printed sample. To ensure a full and even seal, the adhesive was applied carefully using a syringe and needle under a microscope.

4.4.3 Measurement of SPL in free field

The speaker assembly was placed at the center of the room. A B&K 4190 microphone was placed 5 cm and 45 degrees away from the assembly, per the setup diagram. Based on Listen's standard loudspeaker measurement, a signal of stepped-sine sweep was generated, with the exciting voltage set as 0.1 Vrms. The room used for testing complies with ETSI standard TS 103 224 V1.5.1. For reverberation, the ETSI calls for a Clarity 80 average to be larger than 20dB. And C80 of our room is measured as 23.5dB. The low reverberation level and the short measurement distance of 5 cm are deemed acceptable for this measurement. A time-gated measurement would have been employed if the measurement distance were much greater, such as 50 cm.

4.4.4 Measurement of Thiele-Small (TS) parameters, excursion, and electrical impedance

The TS parameters (or the small-signal parameters) of the transducer were measured using the Linear Parameter Measurement (LPM) module of the KLIPPEL Analyzer System by a small excitation signal of 0.1 Vrms. The excursion was measured using Klippel DA-2 analyzer and LK-H052 laser sensor. The speaker was contained in a transparent CAMM sample, which was held in place with the Klippel Microspeaker Clamping Jig. The laser was pointed through the CAMM sample and fixed on the center of the transducer diaphragm. The impedance was measured using the current sense and voltage monitoring capabilities of the DA-2 analyzer.

4.4.5 Measurement of SPL on HATS

The pair of glasses was mounted on a 5128C Head and Torse Simulator (HATS), and the audio module prototypes are positioned 5 cm and 45 degrees away from the ears per the diagram in Figure 5b. The room used for testing complies with ETSI standard TS 103 224 V1.5.1. Signals were measured at a 48kHz sample rate and 24-bit fixed bit depth. A 20 dB gain was added through 1704 2-channel CCLD amplifier for both male voice and music signals. A 30 dB gain was added to music recordings only to make it hearable. The measured digital signals, using Reaper DAW software, are plotted in Figures 5c and 5f with a size of 4096 and a Hann window. To convert the wav file sample values to pressure, a 95.2 dBSPL (1.151 Pa RMS/1.628 Pa) 1kHz reference signal was generated by the sound calibrator type 4231 with DI-0658 adaptor to create a calibrated wave file recording (with 20dB mic amp gain and no other gain added to the recordings). For the reference signal, the average peak sample value is 1333.602, from which the conversion factor can be calculated as 1333.602/1.628=0.00122 Pa/wav sample unit. The music recording has an additional 30 dB gain, which turns the conversion factor to 3.860e-5 Pa/wav sample unit. After converting the digital signal to pressure, power spectrum density is made in **Figure 4.5**d, e, g, and h with a size of 2^{14}, 50% overlap and a Hann window.

4.4.6 THD measurements in free field and on HATS

THD measurements, both in free field and on HATS, were conducted with a stepped-sine sweep signals (20 Hz - 20 kHz) excited at 0.1 Vrms, and a Soundcheck's HarmonicTrak

algorithm was used to measure SPL and track the level and phase of fundamental and harmonics for THD. A measured SPL and THD is plotted in **Figure 4.6**(a-b) when WG50 and CAMM50 were measured in free space. Because of the background noise at low frequencies, useful measurements start around 50 Hz. The variation of THD between WG50 and CAMM50 is plotted in **Figure 4.6**(d) and is less than 5%, which indicates that CAMM does not introduce a strong distortion to the signal. When WG50 and CAMM50 were mounted on HATS, a measured of SPL and THD is plotted in **Figure 4.7**(a-b). Because of the background noise at low frequencies, useful measurements start around 50 Hz. The variation of THD between WG50 and CAMM50 is plotted in **Figure 4.7**(d) and is less than 5%, which also indicates that CAMM does not introduce a strong distortion to the signal.

4.5 Conclusions

In conclusion, we have proposed a coiled acoustic metamaterial to enhance broadband voltage sensitivity and power sensitivity in a head mounted audio module. The metamaterial design is easily manufacturable and more importantly, it doesn't consume additional space. Through a careful tuning of the coupling between the transducer resonance and metamaterial resonance, CAMM introduces a proper added mass on the front port and a smaller phase difference between the front port and the rear port. A combination of these factors leads to a 3-7 dB radiation enhancement in a broad frequency range from 50 Hz to 700 Hz.

Note that there are similar acoustic waveguide designs used in audio engineering such as Dynamic acoustic waveguide [143] and The Wave systems patented by Bose Corporation which use a folded waveguide to improve low-frequency sound from a small enclosure by guiding air through folded acoustic waveguides. However, our proposed coiled acoustic metamaterial design exhibits a few distinctions. One the one hand, more complicated physics such as strong added-mass effect demands delicate considerations as we evolve from the conventional large form-factor audio devices to small form-factor AR/VR devices. On the other hand, besides boosting the sensitivity near the acoustic waveguide frequency, our acoustic-waveguide-like metamaterial also enhances the sensitivity at frequencies much lower than the metamaterial resonance frequency.

Our findings constitute a major step towards using acoustic metamaterial research to solve practical audio industry challenges, which will benefit consumer electronics and AR/VR technologies.

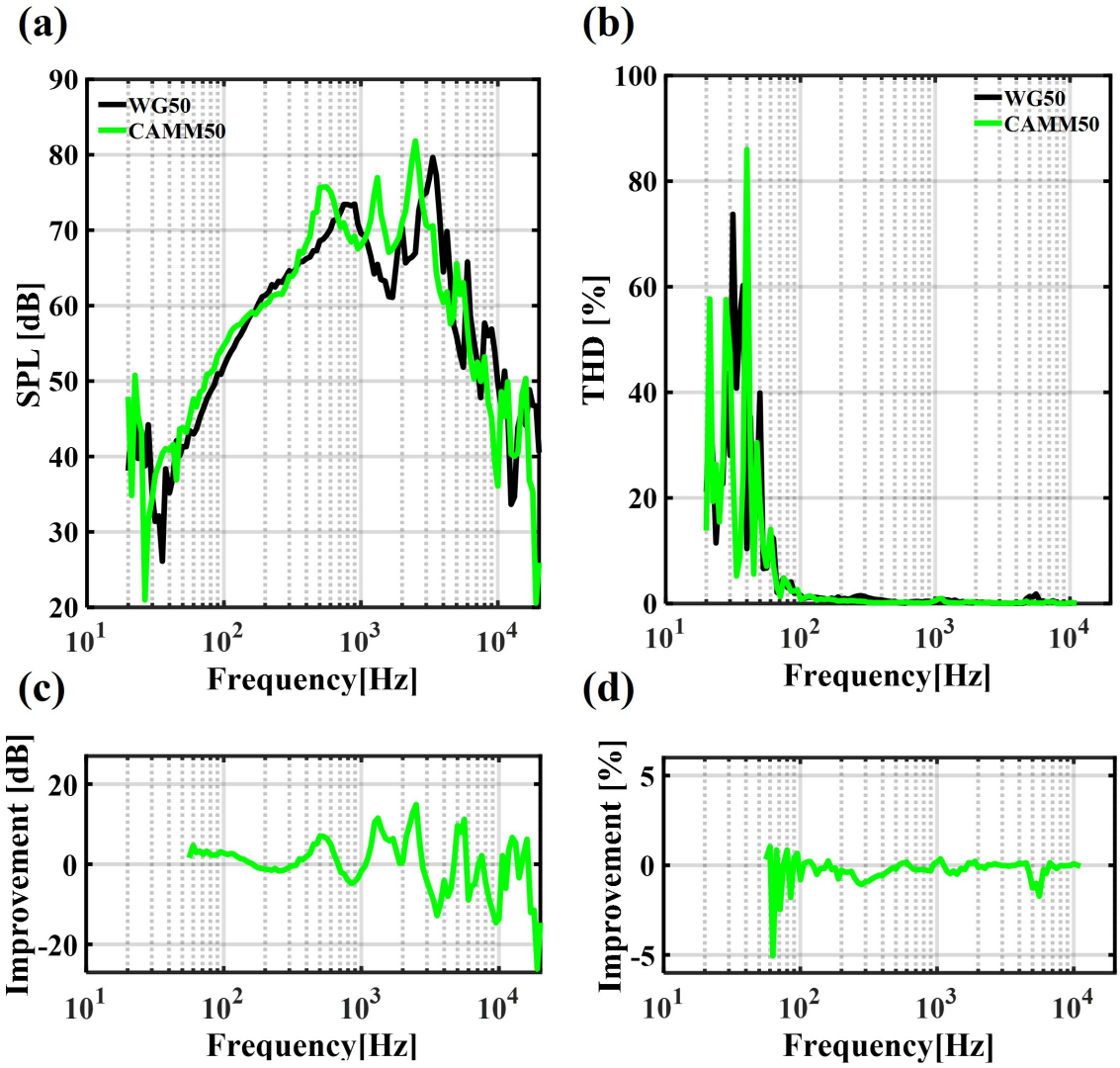

Figure 4.6. Measured (a) SPL and (b) THD for WG50 and CAMM50 in free field. (c) SPL and (d) THD improvement for CAMM50 compared with WG50.

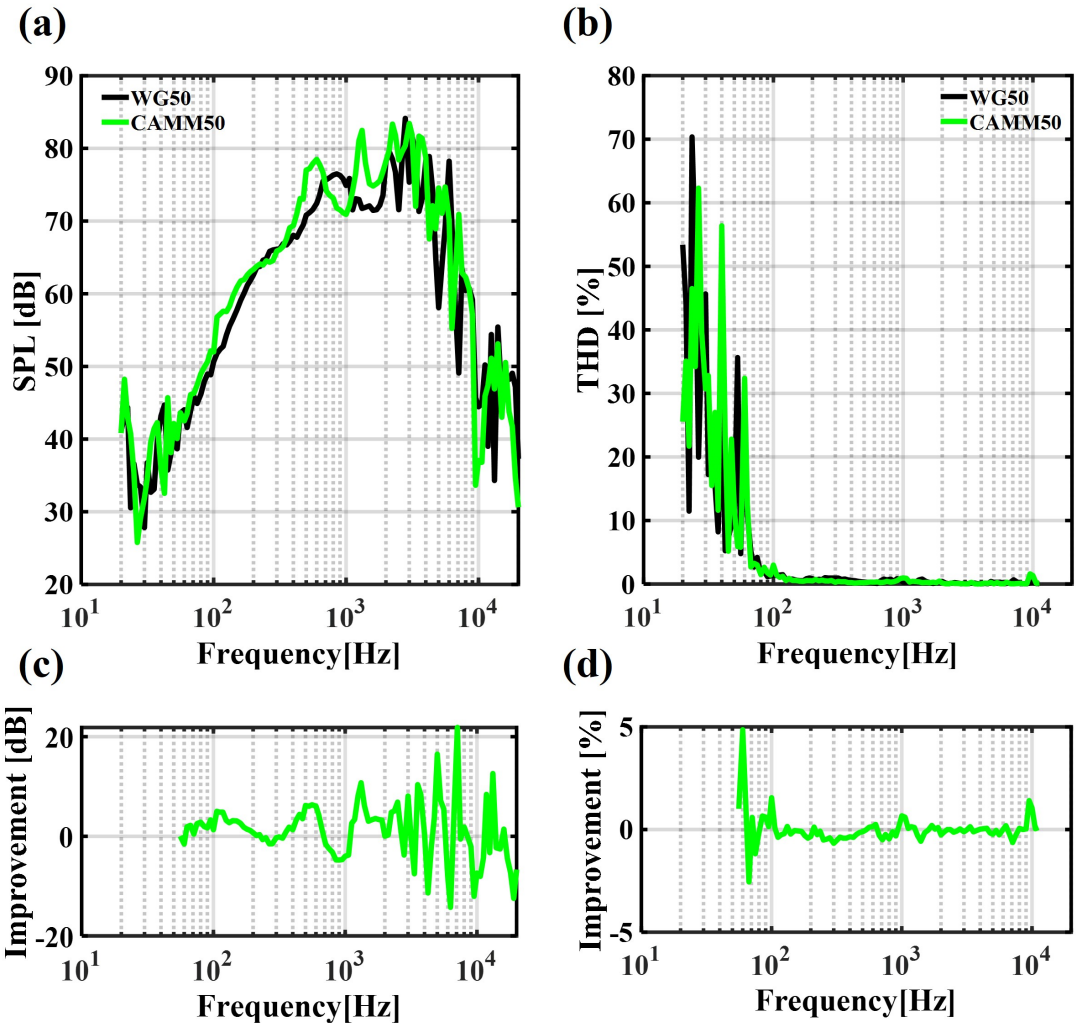

Figure 4.7. Measured (a) SPL and (b) THD for WG50 and CAMM50 on HATS. (c) SPL and (d) THD improvement for CAMM50 compared with WG50.

Chapter 5
Metamaterial-enabled Wireless and Contactless Ultrasonic Power Transfer and Data Transmission Through a Metallic Wall

This chapter presents the study that was published in

- Ji, Jun, et al. "Metamaterial-enabled Wireless and Contactless Ultrasonic Power Transfer and Data Transmission Through a Metallic Wall." Physical Review Applied, 21, 014059, 2024.

Some minor changes have been made to the text to better organize this work into the thesis. Furthermore, some figures have been rearranged and rescaled to match the single-column format of the thesis.

5.1 Background and Introduction

Wireless ultrasonic power transfer (W-UPT) and data transmission (W-UDT) through a metallic wall is an exciting and rapidly advancing field of research, as metal barriers typically hinder the use of electromagnetic power transfer due to the Faraday shielding effect [144, 145, 146]. Based upon such technologies, sensors and actuators enclosed in hermetical metal containers can be wirelessly powered and can communicate with exterior environments through intact metal walls, benefiting a variety of applications in aeronautic and aerospace engineering [147, 148] and nuclear engineering [149, 150]. Conventionally, W-UPT and W-UDT utilize at least a pair of PZT (Lead zirconate titanate) ultrasound transducers attached to a metal barrier. The main limitation of this approach, however, is that it requires direct contact of piezoelectric transducers with metal walls using couplants to ensure a good acoustic transmission path. The quality of couplants, such as epoxy, may degrade or even fail as operating time goes by [144], which can introduce large impedance mismatch over the acoustic-electric channel and cause the power transfer and data transmission efficiency to rapidly decrease. Therefore, wireless and contactless ultrasonic power transfer (WC-UPT) and data transmission (WC-UDT) through a metallic wall is highly desirable.

Meanwhile, acoustic metamaterials [1] have attracted numerous research efforts in recent years due to their capability to control the propagation of sound in unconventional ways, which have led to interesting phenomena and applications such as cloaking [127, 15, 128], sub-wavelength imaging [17, 34, 18], and unidirectional transparency [25, 130]. Despite significant advancements in acoustic metamaterials, a demonstration of an acoustic metamaterial capable of facilitating WC-UPT and WC-UDT through a metallic wall has yet to be achieved. On the one hand, whereas extraordinary acoustic transmission has been enabled by near-zero-density metamaterials [151, 152] and acoustic evanescent waves [153, 154, 155, 156], these designs still require small apertures for sound transmission, defeating the purpose of W-UPT and W-UDT. On the other hand, complementary acoustic metamaterials [157, 158, 159] have been theoretically proposed to achieve enhanced transmission non-invasively through an impedance-mismatched layer, utilizing doubly negative acoustic properties. However, experimental demonstrations of complementary acoustic metamaterials have been scarce due to the challenges in precisely prototyping either the membrane [157, 160] or intricate metallic meta-atoms [159]. For the limited experimental realizations of complementary acoustic metamaterials [161], though energy transmission improvements were demonstrated for weakly impedance-mismatched

layers (e.g., plastic or resin barrier layers in water), the same approach may not be equally effective for through-metal-wall power transfer where relative large impedance mismatch is present. In addition to complementary metamaterials, an inversely optimized auxiliary meta-lens [162] has been demonstrated to assist the focusing enhancement through a 1.8 mm metallic wall in water at 200 kHz. However, the overall power transmission rate was not quantitatively analyzed. The inverse optimization method used for designing the meta-lens also may not be applicable for all general physical scenarios.

In this study, we present a metamaterial-based approach to enable WC-UPT and WC-UDT through a metallic wall immersed in a strongly impedance-mismatched background medium. A deterministic method based on the band structure theory and transmission analyses is utilized to design an ultrasonic pillar-based metamaterial. The vertical elongation mode (VEM) of the pillars is harnessed to achieve ultrasonic power transmission enhancement through the metallic wall without direct contact with transducers. This effectively addresses the notorious couplant degradation issue that is a characteristic of conventional methods in W-UPT and W-UDT. We numerically and experimentally demonstrate that the metamaterial, fabricated by the SLS (selective laser sintering) additive manufacturing technology, enables a 33-fold ultrasonic power transmission rate enhancement from 2% to around 66% near 450 kHz through a 1 mm thick SUS316L plate, whose impedance is 29 times of the background medium water. In addition, a commercial red light-emitting diode (LED) is successfully lit up by harvesting the enhanced transmission of ultrasonic energy, which cannot be lit up without the metamaterial even at an input voltage that is close to five times greater. Benefiting from the enhanced signal-to-noise ratio (SNR) of the received signal, WC-UDT is also demonstrated by transmitting an image using amplitude shift keying (ASK) modulation at a small input voltage.

5.2 Pillar-based acoustic metamaterial

Figure 5.1 illustrates the working principle of the proposed WC-UPT and WC-UDT. A pair of co-axially aligned PZT transducers are placed on opposite sides of a metallic wall immersed in the background medium (e.g., water), working as a transmitter and a receiver, respectively. A pillar-based acoustic metamaterial, which has been studied in the past to reduce sound transmission through a thin and lightweight barrier in noise control [163, 164], is now proposed to conversely enhance the power transfer through the metallic wall. The proposed pillar-based acoustic metamaterial is composed of

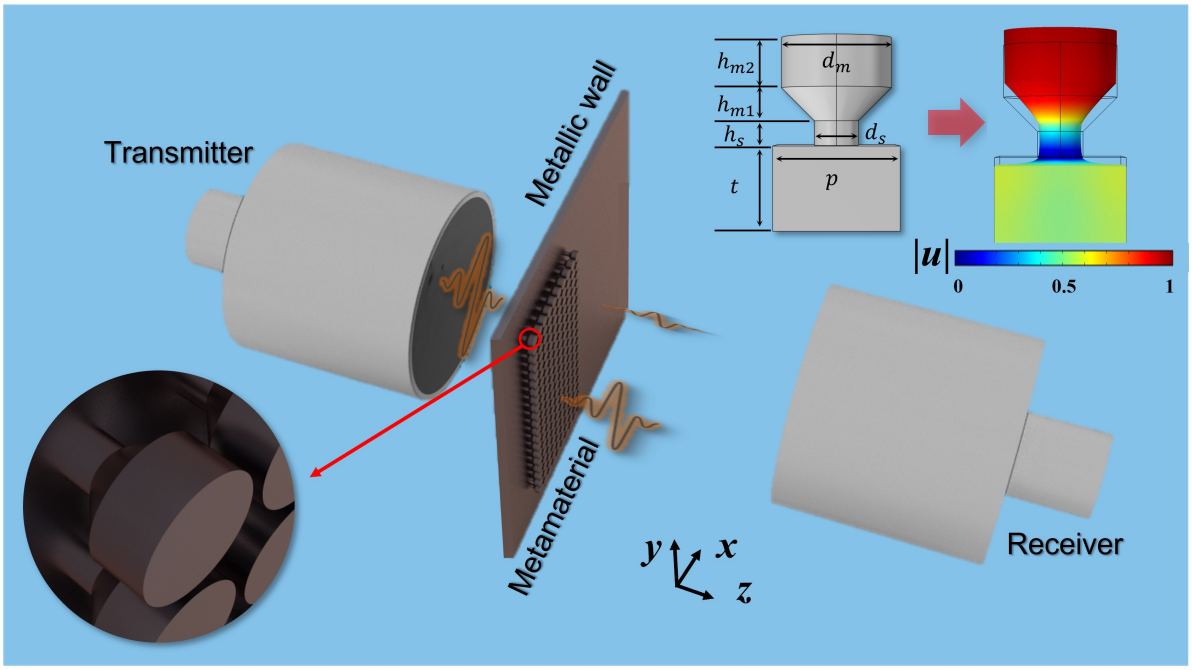

Figure 5.1. Schematic of the through-metal-wall WC-UPT and WC-UDT system enabled by the pillar-based acoustic metamaterial. A close-up view of the metamaterial is displayed in the bottom-left corner. The displacement field of the metamaterial at VEM is shown in the top-right corner, which is the mechanism used to enhance the ultrasonic power transmission rate through the metallic wall.

periodically arranged pillars (with periodicity p) distributed on the metallic wall (with thickness t), as shown in the close-up views in the top-right and bottom-left corners of **Figure 5.1**. Each pillar is fundamentally an acoustic spring-mass resonator, in which the large cylinder (with diameter d_m and height h_{m2}) works as a "mass" and the smaller cylinder (with diameter d_s and height h_s) works as a "spring". In this study, the pillar is assumed to be made of the same material as the wall, and is tapered with a height of h_{m1} between two cylinders in order to facilitate 3D printing at a high accuracy. Once the resonant frequency of the pillar-based acoustic metamaterial is carefully tuned towards the working frequency of transducers, the ultrasonic wave generated by the transmitter can propagate through the metallic wall and excite a strong vibration of the pillars. The resonating pillars, as shown by the distribution of the normalized displacement magnitude $|u|$ in the top-right corner of **Figure 5.1**, will work as secondary acoustic sources to re-radiate the ultrasonic wave to the other side of the wall, which would otherwise have a very limited power transmission without the metamaterial. Subsequently, the receiver can convert the metamaterial-enhanced ultrasonic signal back to electrical signal to power electronics or simply receive the signal for data transmission.

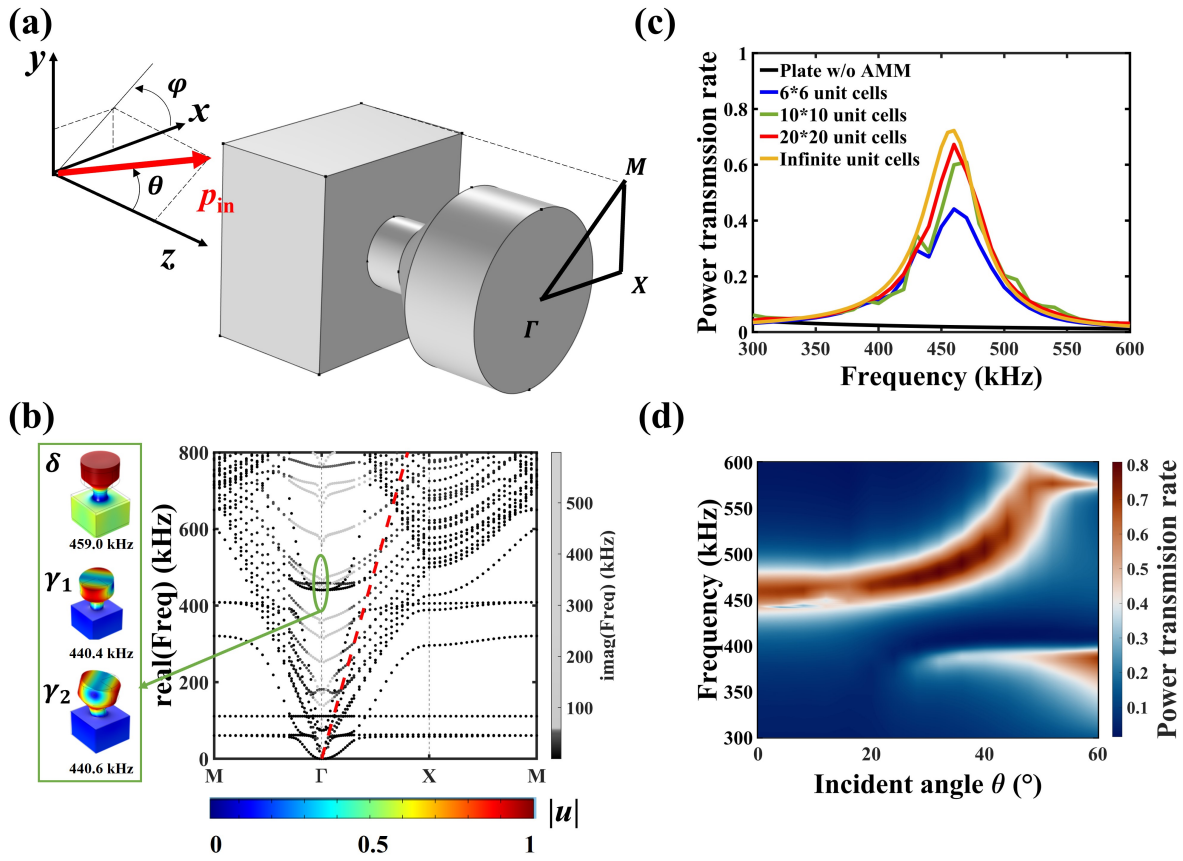

Figure 5.2. Design of the pillar-based metamaterial for the through-metal-wall WC-UPT and WC-UDT. (a) Schematic of a periodically arranged unit cell under a incident plane wave and the first irreducible Brillouin zone. (b) The complex band structure. The real eigenfrequency is plotted on y axis and the imaginary eigenfrequency is represented by the gray scale. The green ellipse encompasses three propagating modes corresponding to δ, γ_1, and γ_2. The distribution of the normalized displacement magnitude |u| for these modes is depicted by the color scale. The red dash line is the sound line. (c) Power transmission rate for different number of unit cells under a normally incident plane wave. (d) Power transmission rate as a function of the incident angle of θ when $\phi = 0$.

To demonstrate WC-UPT, we adopt a $t = 1$ mm steel (SUS316L) wall in water and a pair of PZT transducers with a center frequency around 500 kHz. The pillar-based acoustic metamaterial is designed based on the modes observed from the calculated band structure. **Figure 5.2**a shows one unit cell of the proposed acoustic metamaterial distributed on the wall. The incident pressure is $p_{\text{in}} = P_{\text{in}} e^{j(-k_x x - k_y y - k_z z)} e^{j\omega t}$, in which $k_x = k\sin\theta\cos\phi$, $k_y = k\sin\theta\sin\phi$, $k_z = k\cos\theta$, and $k = \omega/c_0$. c_0 is the sound velocity in water. θ and ϕ are the polar and azimuthal angles of incidence, respectively. **Figure 5.2**b shows the numerical calculation (see **Section 5.6.1** for details) of the complex band structure

for the periodically arranged unit cells along the edges of the first irreducible Brillouin zone $\Gamma - X - M$ as shown in **Figure 5.2**a. The size of the unit cell is $p = 1.5\,\text{mm}$ (half wavelength at 500 kHz), $d_s = 0.54\,\text{mm}$, $d_m = 1.35\,\text{mm}$, $h_s = 0.3\,\text{mm}$, $h_{m1} = 0.405\,\text{mm}$, and $h_{m2} = 0.615\,\text{mm}$. In what follows, we will only focus on the wave dispersion along the $\Gamma - X$ direction (i.e., y component of the wave vector is zero), as the same physical behaviors can be observed for the other directions. The imaginary eigenfrequency is resulted from the Plane Wave Radiation boundary condition applied on both incoming and outgoing planes. These modes with a large imaginary eigenfrequency are decaying fast in time (or highly evanescent in space since the speed of sound is real) and cannot transmit wave from one side of wall to the other side. For these modes with a small imaginary eigenfrequency, the distribution of the normalized displacement magnitude $|u|$ at Γ point near 500 kHz is plotted to help understand the induced resonances and anti-resonances from the coupling between the wall (plate) and pillars. Here, the anti-resonances are modes where the vibrational amplitude at the plate becomes zero, suggesting that the transmission through the plate is not allowed, whereas the resonances correspond to a non-zero vibrational amplitude at the plate and thus have the potential to enhance transmission [165]. Near 500 kHz, while (γ_1, γ_2) is one pair of degenerate anti-resonance modes, δ is a vertically elongation resonant mode with a successively stretching and compressing motion of the pillars along the vertical direction z. Based on the law of the momentum conservation, δ can be excited when the incident wave has a normal wave component (i.e., $\theta = 0$ and $\phi = 0$). The flat band frequency at which the δ mode [166] arises can be adjusted by altering the geometric parameters of the tapered pillar. For instance, decreasing the size of the "mass" or increasing the cross-section of the "spring" can increase the flat band frequency.

The extent to which the transmission enhancement enabled by the pillar-based acoustic metamaterial can be further assessed by numerical transmission analyses in the frequency range between 300 kHz and 600 kHz. We first study the impact of the number of unit cells on the power transmission rate, which is evaluated under a normally incident plane wave. These results are shown in **Figure 5.2**c and illustrate that the power transmission rate increases from 1.9% to 72.3% at 460 kHz when an infinite number of the designed pillar-based acoustic metamaterial units are periodically attached to a 1 mm SUS316L plate. The real eigenfrequency of 459 kHz obtained from the band structure calculation closely aligns with the peak transmission frequency of 460 kHz observed in the transmission analyses. Typical material loss of SUS316L [167] is evaluated and it barely affects the power transmission rate according to our numerical simulations (See **Section**

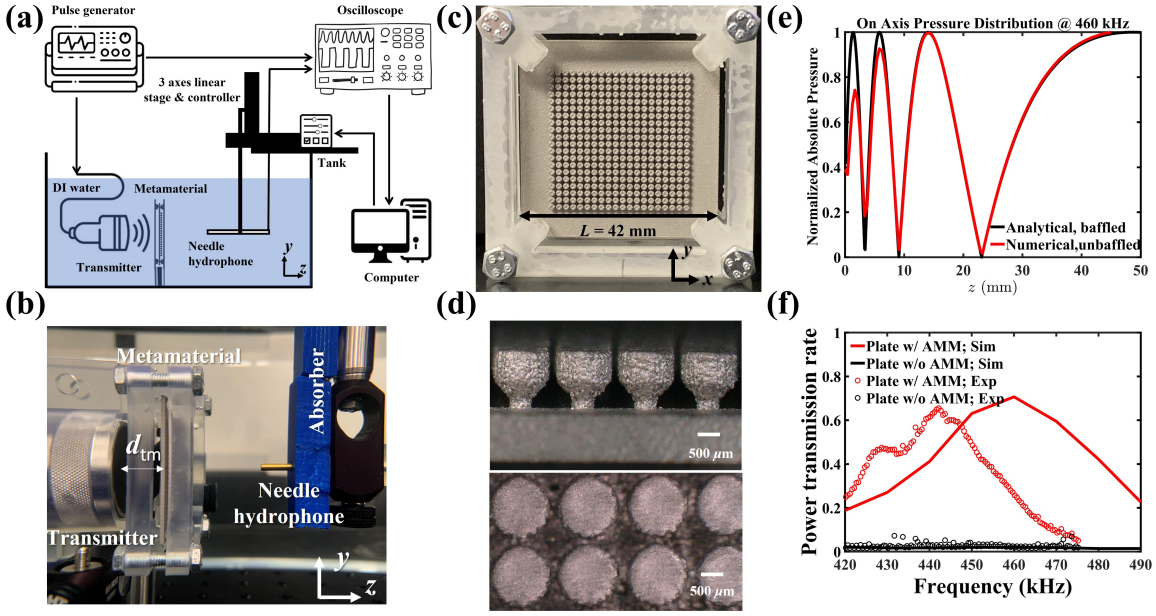

Figure 5.3. (a) and (b) show the schematic and photo of the experimental setup. (c) and (d) show the fabricated plate with AMMs. (e) The on-axis pressure magnitude distribution has multiple local extremes in the near field of the piston transmitter. (f) Comparison of simulated and measured power transmission rate.

5.6.1). For practical considerations, a series of numerical calculations for different finite numbers of unit cells attached on an infinitely large wall are conducted, and they show that 20 × 20 unit cells can achieve a power transmission rate of 67.3%, which sufficiently approaches that obtained from an infinite number of unit cells (See **Section 5.5.2** for detailed simulation setup). This verifies the hypothesis of using the resonance mechanism of VEM to enhance power transmission, which is inferred from the observations in the band structure calculation. In addition, the power transmission rate with respect to the angle of incidence is numerically evaluated, where θ varies from 0° to 60° and $\phi = 0°$. Since there is no wave component on the y direction when $\phi = 0°$, 20 unit cells are simulated along the x direction, and 1 unit cell is simulated along the y direction with a continuity boundary condition to reduce computational costs (See **Section 5.5.3** for the detailed setup of simulations). The results are shown in **Figure 5.2**d and indicate that the power transmission rate can stay at a large magnitude (more than 70%) for a wide range of angles of incidence from 0° to 60°, when excited at the proper frequency. For smaller angles of incidence though, the optimal frequency remains relatively constant and is around 460 kHz.

The generality of the pillar-based acoustic metamaterial on through-metal-wall power

transmission enhancement is numerically confirmed in the background medium of air, where the impedance contrast is around 104,850. Note **Section 5.5.4** shows that the power transmission rate is 0.00001% around 50 kHz through a 1 mm thick SUS316L bare plate immersed in air, and it can be enhanced by at least four orders of magnitude to 20%, 2%, 0.6% or 0.15%, when the loss factor of SUS316L for AMM is set as 0.0001, 0.0005, 0.001 and 0.002, respectively. Unlike the waterborne case, the power transmission rate for the airborne case is inherently ultra-sensitive to the loss factor and has a narrower bandwidth, as shown in **Figure** C4. These are likely originated from the substantial impedance mismatch between the air and SUS316L, and would place a demand on advanced 3D additive metal printing to precisely control the loss factor for experimental validations.

To further demonstrate the philosophy of using the pillar-based acoustic metamaterial for ultrasonic power transmission enhancement, the waterborne case is experimentally validated against numerical simulations, using the state-of-the-art 3D metal printing technology. A 42 mm $\times$ 42 mm $\times$ 1 mm wall ($L \times L \times t$, L is the side length) decorated with 20 $\times$ 20 aforementioned pillars is under an excitation from a PZT transducer with a diameter $d = 2a = 1$ inch and a central frequency around 500 kHz. **Figure 5.3**a and **Figure 5.3**b show the schematic and photo of the experimental setup. The origin of the coordinate is set at the center of the transmitter surface and the on-axial propagating direction of the transmitter aligns with the positive z direction. Since the on-axis pressure magnitude has multiple local extremes in the near field of the piston transmitter as shown in **Figure 5.3**e (Details of simulated radiation field of the transmitter are referenced to **Section 5.5.6**), the plate with or without AMM is placed at the farthest maximum from the transmitter for the ease of experimental implementations, that is $d_{\mathrm{tm}} = a(a/(m\lambda_0) - m\lambda_0/(4 * a)) = 14$ mm for $m = 3$ (the third extreme moving in toward the transmitter) [168] at $f_0 = 460$ kHz. However, we note that the power transmission rate is insensitive to d_{tm}, as supported by the same transmission enhancement achieved when the plate is placed at the minimal pressure location in the near field of the transmitter (Details are referenced to **Section 5.5.7**). **Figure 5.3**c shows the photo of the plate with AMM fabricated by SLS technology (see **Section 5.6.2** for details), and **Figure 5.3**d shows a close-up view. A needle hydrophone scans the transmitted pressure field at the other side of the plate in both x-y plane and x-z plane for three configurations ("No Plate", "Plate w/ AMM", and "Plate w/o AMM"), as shown in **Figure 5.4**. Details of experimental measurements are referred to **Section 5.6.3** and **Section 5.5.8**. The simulated and measured pressure amplitude distribution in x-y plane is retrieved at

$z = 45$ mm, which is close to the Rayleigh distance, as shown in **Figure 5.4**a and **Figure 5.4**b. The Rayleigh distance, $L_R = d^2/(4\lambda_0)$, is the transition point between the near field and far field, and it is the preferred location for a receiving transducer to tap the maximum power from the transmitter [169]. Pressure amplitude distribution in x-z plane is plotted at $y = 0$ mm in **Figure 5.4**c and **Figure 5.4**d for numerical and experimental results, respectively. The displayed pressure field is at the peak power transmission frequency, which is 442 kHz for the measurements and 460 kHz for the simulations. Then, the amount of power at the transmitted side is estimated based on the square of pressure amplitude at the surface of $z = 45$ mm, which is a reasonable approximation when transitioning to the far field. The power transmission rate for the "Plate w AMM" and "Plate w/o AMM" configurations can be obtained by normalizing the power transmission of each respective plate configuration to that of the reference "No Plate" configuration. **Figure 5.3**f shows a comparison of simulated and measured power transmission rate for the plate with and without AMM. The measured power transmission rate for the 1 mm bare plate is approximately 2% around 442 kHz. In contrast, with the addition of AMM on top of the plate, the measured power transmission is boosted to 65.5% at 442 Hz, with a half-power bandwidth of 33 kHz. Except the slight frequency shift (which is likely due to imperfect fabrication and details are referenced to **Section 5.5.5**), a good agreement is observed between measured and simulated results, showing the expected power transmission enhancement enabled by the AMM.

5.3 Wireless and contactless ultrasonic power transfer

With the verified capability of transmission enhancement through the metallic wall, the pillar-based acoustic metamaterial is then employed to realize a WC-UPT. **Figure 5.5**a shows the schematic and photo of energy harvesting through the metal wall, with a larger transducer (1.5 inch diameter, 400 kHz resonant frequency) being placed at $z = 45$ mm as a receiver to collect the transmitted ultrasound power to the maximal extent. The receiver is characterized by the impedance spectrum measurement and the optimal power transfer test using a resistive load [170, 171] (See **Section 5.5.9** for details).

Next, we demonstrate that the enhanced ultrasonic power transmission is harvested to charge a series of capacitors and light up a commercial LED, which is otherwise impossible through a bare plate. **Figure 5.5**b shows the measured output signals of the receiver under an excitation of 445 kHz continuous-mode ultrasound for four different configurations: an input voltage of 4.4 Vpp on the transmitter for (i) "No Plate", (ii)

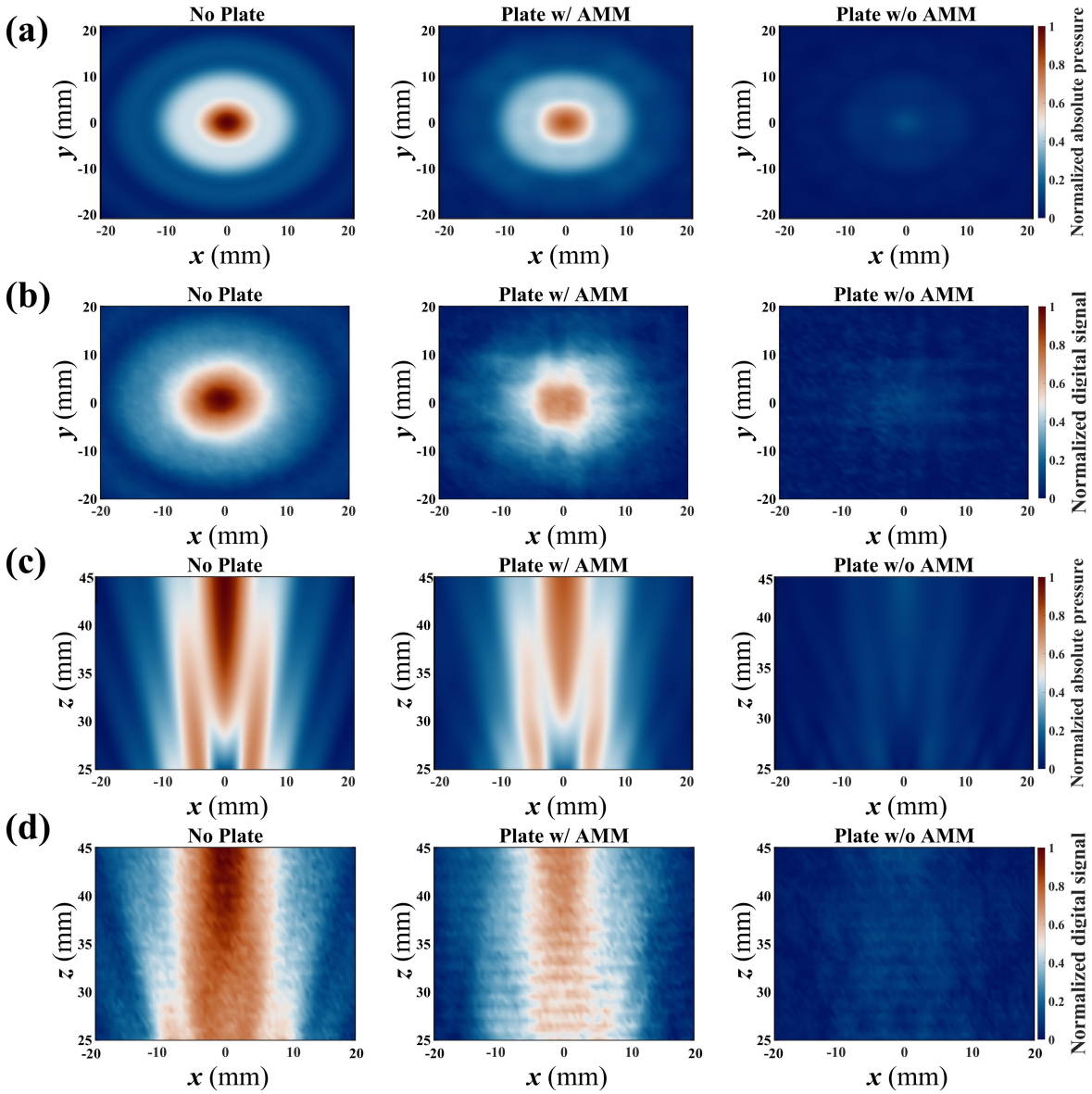

Figure 5.4. The transmitted pressure field from numerical simulations (at 460 kHz) and experimental measurements (at 442 kHz) demonstrates the transmission enhancement enabled by AMM. (a) Simulated and (b) measured pressure field in x-y plane at $z = 45$ mm. (c) Simulated and (d) measured pressure field in x-z plane at $y = 0$ mm. The center of the transmitter surface is set as the origin of the coordinate. For each sub-figure, the pressure magnitude is normalized by the maximum value in the case of "No Plate".

"Plate w/ AMM", and (iii) "Plate w/o AMM", as well as (iv) an input voltage of 20 Vpp on the transmitter for "Plate w/o AMM". The alternating current (AC) collected by the receiver is not a feasible power source for most electronics. Therefore, the AC signal is rectified into a DC signal using a pre-designed full-wave-bridge-rectification circuit (See

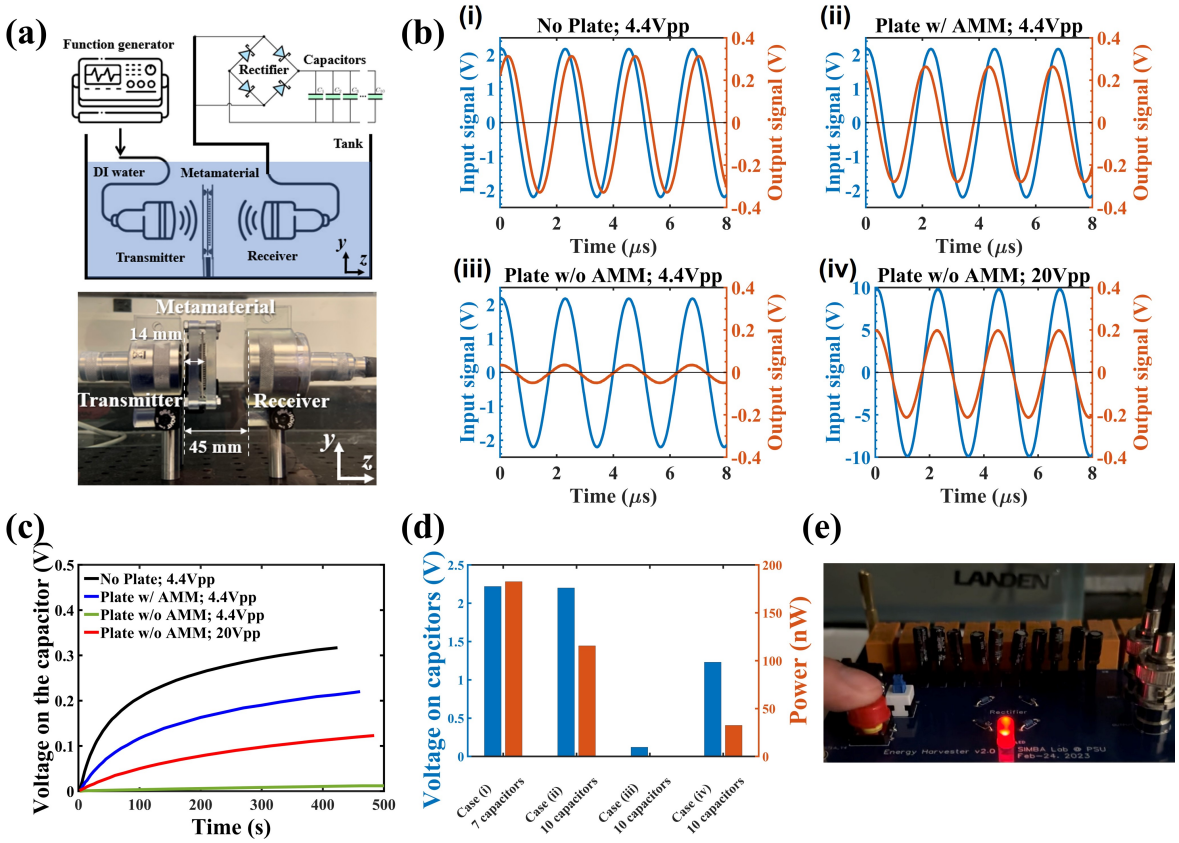

Figure 5.5. Experimental results of wireless and contactless ultrasonic power transfer through a metallic wall using the pillar-based metamaterial. (a)Schematic and photo of experimental setups. The enhanced ultrasonic transmission is collected by a receiver to charge capacitors. (b) The measured output signals of the receiver under an excitation of 445 kHz continuous-mode ultrasound for four different configurations: an input voltage of 4.4 Vpp on the transmitter for (i) "No Plate", (ii) "Plate w/ AMM", and (iii) "Plate w/o AMM", as well as (iv) an input voltage of 20 Vpp on the transmitter for"Plate w/o AMM". (c) The charging time dependence of voltage on a 220 µF capacitor for the four configurations. (d) Comparison of the charged voltage and average charging power. (e) Photo showing that a commercial LED lit up in the configuration (ii).

Section 5.5.10 for details about the circuit design). **Figure 5.5**c shows the measured DC signals stored on a 220 µF during the charging process for more than 400 s until the voltage rise becomes gradual and approaches saturation. While the amplitudes of AC output signals are read as (i) 0.334 V, (ii) 0.264 V, (iii) 0.036 V, and (iv) 0.199 V, the DC voltage on each capacitor is (i) 0.317 V, (ii) 0.220 V, (iii) 0.012 V, and (iv) 0.123 V. The slight voltage drop from AC to DC is mainly caused by the built-in voltage drop across the diodes of the rectifier. Considering the threshold voltage to light up a red LED is around 2 V, 7 series-connected capacitors in the first configuration "No Plate"

collect 2.22 V, as shown in **Figure 5.5**d, which is enough to light up the LED. The power is also evaluated in the process, which is given by [172] $\bar{P} = C_s V_s^2/(2T)$, where C_s is the capacitance, T is the charging time, and V_s is the stored DC voltage. Thus, the energy stored on the capacitors in the first configuration is increased by 77.4 μJ in 424 s, indicating that the power output capability is 182 nW. In the second case of "Plate w/ AMM", 10 series-connected capacitors reaches 2.1 V with a output power of 116 nW, to successfully light up the LED as shown in **Figure 5.5**e. The output power of the second case is calculated as 64% of the first case, in good accordance with the measured power transmission coefficient 65.5% in **Figure 5.3**d. However, for the third case of "Plate w/o AMM", the total voltage on 10 series-connected capacitors is only 1.2 V, which is insufficient to power the LED, even when a 20 Vpp excitation was applied to the transmitter (which is the fourth case of "Plate w/o AMM"). Details about the energy harvesting circuit is referred to **Section 5.5.10**.

5.4 Wireless and contactless ultrasonic data transmission

In addition to WC-UPT, WC-UDT is also demonstrated using the same setup in **Figure 5.5**a. Instead of using the continuous mode at a large input voltage for power transfer, burst-mode sinusoidal signals under ASK modulation are fed into the transducer at a small input voltage (25 mV) to transmit the encoded binary data. The received signals, having undergone SNR enhancement facilitated by AMM, can then be amenable to decoding. Using a string of 15-bits data (which is the signal of 15th column in **Figures 5.6**((b)-(e)) as an example, **Figure 5.6**a showcases the encoding and decoding communication process of WC-UDT: (i) The 15-bits binary signal is first embedded within start bits (100) and stop bits (001). (ii) A time-domain digital signal is generated to transmit the 21-bits binary signal using ASK modulation, and is then fed into the transmitting transducer. Here, each bit is represented by 5 cycles of sine waves at 445 kHz. 21 bits are transmitted every 0.4 ms and the communication speed is 52.5k bps. The digital power, which is defined as the summation of the voltage square for every 5 cycles of sine waves, is proposed as an algorithm to characterize the quality of the transmitted digital signal and extract data from the received digital signal. As shown by the orange curve, the line-shape of the digital power for the transmitted signal agrees perfectly with the binary signal, showing the good quality of the transmitted signal. (iii) Despite a slight distortion in the received digital signal mainly caused by the frequency response of the transducer pair, the decoded signal, obtained by computing its digital power, exhibits

a strong correspondence with the transmitted signal in the presence of AMM. (iv) In the absence of AMM, the transmitted signals is weaker and strongly contaminated by the noise. Consequently, the recovery of the transmitted signal from the received signal becomes challenging. Next, a more complicated binary image showing letters of "PSU" is used to demonstrate WC-UDT. **Figures 5.6**b depicts the original image composed of 15×36 pixels, which is encoded into binary signals of "0" and "1". **Figures 5.6**((c)-(e)) are images of the digital power (normalized by their respective maximum digital power) for the transmitted signal, the received signal in the presence of AMM, and the received signal in the absence of AMM, respectively. The implementation of AMM allows for the restoration of a clear image depicting the letters "PSU". In contrast, the absence of AMM yields a noise-dominant recovered image, which necessitates an increase in the input voltage and subsequently incurs a higher power cost.

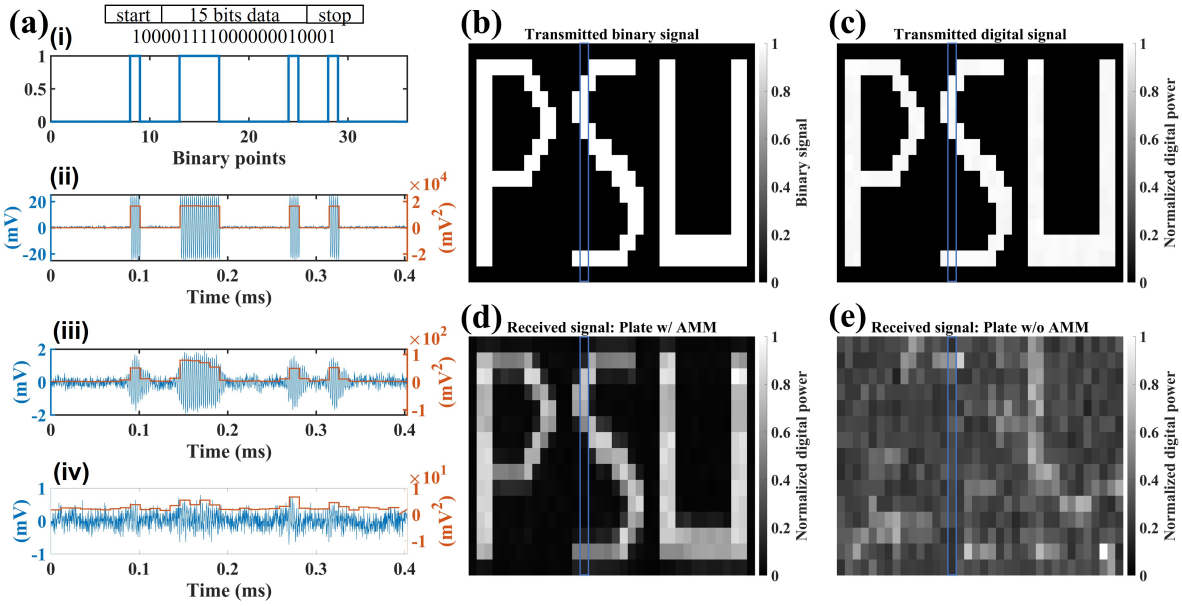

Figure 5.6. Experimental results of wireless and contactless ultrasonic data transmission of a binary image of "PSU". (a) The transmission of binary data using ASK modulation: (i) a 15-bits binary signal embedded within the start bits (100) and the stop bits (001), (ii) the binary signal is transformed into digital signal before being transmitted through a PZT transducer, in which each bit is represented by 5 cycles of sine waves at 445 kHz, (iii) the received time-domain digital signal for "Plate w/ AMM", and (iv) the received time-domain digital signal for "Plate w/o AMM". For (ii) - (iv), left axis is the digital voltage and right axis is the digital power. (b) The original image composed of 15×36 pixels is encoded into binary signals of "0" and "1". (c) The transmitted digital image. (d) The received digital image for "Plate w/ AMM". (e) The received digital image for "Plate w/o AMM". The digital power in (c)-(e) is normalized by their respective maximum digital power. The signals in the 15th column (highlighted by blue blocks) of images in (b)-(e) are shown in (a).

5.5 Discussions

The section includes more detailed analyses for previous sections.

5.5.1 The impact of loss factor of SUS316L on the power transmission rate in simulations

To evaluate how loss factor of SUS316L affects the power transmission rate in COMSOL, four different typical values are considered: $\eta = 0.0001$, $\eta = 0.0005$, $\eta = 0.001$, and $\eta = 0.002$. In the simulations, one unit cell is considered under a normally incident wave, and "Continuity" under "Periodic Condition" is applied to both water and SUS316L since there is no wave components along the x and y direction. The loss factor is applied under "Damping" of "Linear Elastic Material". The simulated results in **Figure 5.7** indicate that the typical loss factor of SUS316L barely affects the power transmission rate.

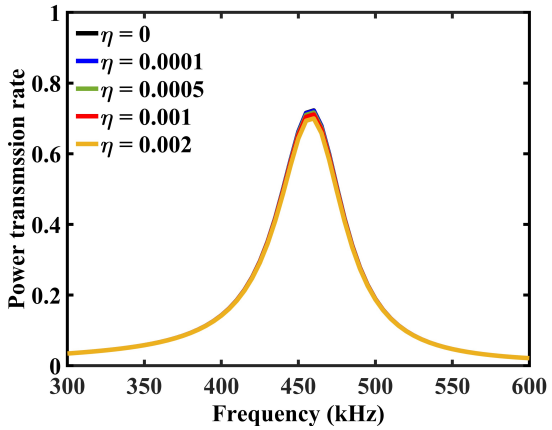

Figure 5.7. The power transmission rate as a function of SUS316L loss factor in COMSOL.

5.5.2 The impact of the number of unit cells on the power transmission rate in simulations

To evaluate how the number of unit cells affects the power transmission rate in COMSOL, three different cases are considered: 6×6, 10×10, and 20×20 unit cells. The incident wave is a plane wave normal to the plate surface using "Plane Wave Radiation", and the plate is infinitely large to ignore the backward propagation from the edges by setting "Perfectly Matched Layer" around the plate. The incident and transmitted wave are confined in a

waveguide having the same cross sectional area with the metamaterial units to ignore the wave diffraction effect. Only 3×3, 5×5, and 10×10 unit cells are modeled in COMSOL with "Symmetry" boundary condition to reduce computational costs. "Perfectly Matched Layer" is set at the transmission end to reduce the back reflection. The non-perfect plane wave from the transducer effect, the finite plate size effect and the wave diffraction effect are considered in the large sample test in **Figure 5.12**. **Figure 5.8** shows the pressure distribution for the three cases at the power transmission peak frequency 460 kHz.

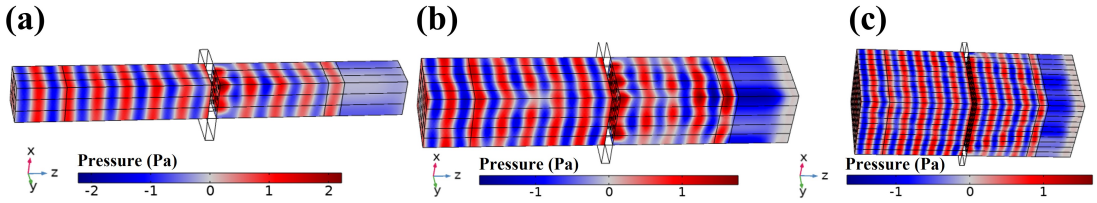

Figure 5.8. The pressure distribution at the power transmission peak frequency 460 kHz for (a) 6×6, (b) 10×10, and (c) 20×20 unit cells. The middle part without the pressure distribution is the plate region simulated with "Solid Mechanics" module.

5.5.3 The impact of the incident angle on the power transmission rate in simulations

To evaluate how the anlge of incidence θ affects the power transmission rate in COMSOL, we have chosen the case of 20×20 units for illustration. Since we have assumed $\phi = 0$, there is no wave component along the y direction. Therefore, we have constructed only one unit cell along the y direction, with "Continuity" under "Periodic Condition" being applied to both water and SUS316L along the y direction to reduce computational costs. The incident wave is applied using "Background Pressure Field" with a parametric sweep of θ from 0° to 60° and the scattered field can be solved from 300 kHz to 600 kHz. "Perfectly Matched Layer" is applied at both the incident and transmitted sides to minimize reflections. The transmitted power is calculated by integrating the default function "Acoustic Intensity" along a surface enclosing the metamaterial at the transmitted side. **Figure 5.9**a and **Figure 5.9**b illustrate the distribution of the background pressure and the scattered pressure, respectively, when the excitation frequency is 460 kHz and $\theta =$ 60°. And a strong transmission can be observed.

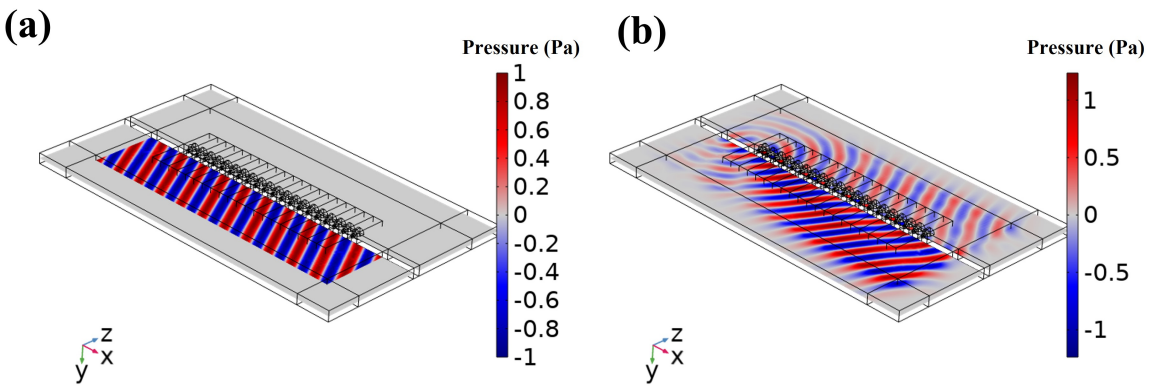

Figure 5.9. The distribution of (a) the background pressure and (b) the scattered pressure when the excitation frequency is 460 kHz and $\theta = 60°$.

5.5.4 Power transmission enhancement through $t = 1\,\text{mm}$ SUS316L wall in air around 50 kHz

To demonstrate the generality of the design philosophy of power transmission enhancement, a double-sided pillar-based acoustic metamaterial is proposed to enhance ultrasonic power transmission through 1 mm thick SUS316L plate in air, with a 50 kHz ultrasound as the incident wave, as shown in **Figure 5.10**a. Considering the huge impedance mismatch between air and SUS316L, identical pillars are distributed on both sides of the plate to induce a larger vibration for power transmission enhancement. The same procedure with band structure and transmission analyses is utilized to design the metamaterial. The only difference from the water scenario is that the background medium of air is not considered in the band structure calculation since the mass loading effect from air is very small. Consequently, the obtained band structure is purely real. The size of the unit cell is $p = 5.72\,\text{mm}$ (less than one wavelength at 50 kHz), $t = 1\,\text{mm}$, $d_s = 0.42\,\text{mm}$, $d_m = 5.43\,\text{mm}$, $h_s = 0.86\,\text{mm}$, $h_{m1} = 1.15\,\text{mm}$, and $h_{m2} = 6.14\,\text{mm}$. **Figure 5.10**b and **Figure 5.10**c show the band structure and the power transmission for a unit cell with Floquet periodic condition, respectively. The vertical elongation mode at 50.92 kHz shown in the inset contributes to the power transmission rate enhancement from 0.00001% to near 100% around 51 kHz. Unlike the water-SUS316L case, the air-SUS316L case is ultra-sensitive to the loss factor of SUS316L, as shown in **Figure 5.10**d. As the loss factor increases, the peak power transmission rate near 51 kHz is decreased by several orders of magnitude, which is 94%, 20%, 2%, 0.6%, and 0.15% when the loss factor is 0, 0.0001, 0.0005, 0.001, and 0.002, respectively. However, the power transmission rate for the loss factor of 0.002 is still 4 orders of magnitude higher than that without AMM.

The nature of being ultra-sensitive to the loss factor and the narrow bandwidth are likely caused by the huge impedance mismatch between the air and SUS316L, which requires more advanced 3D additive metal printing in the future for experimental validations.

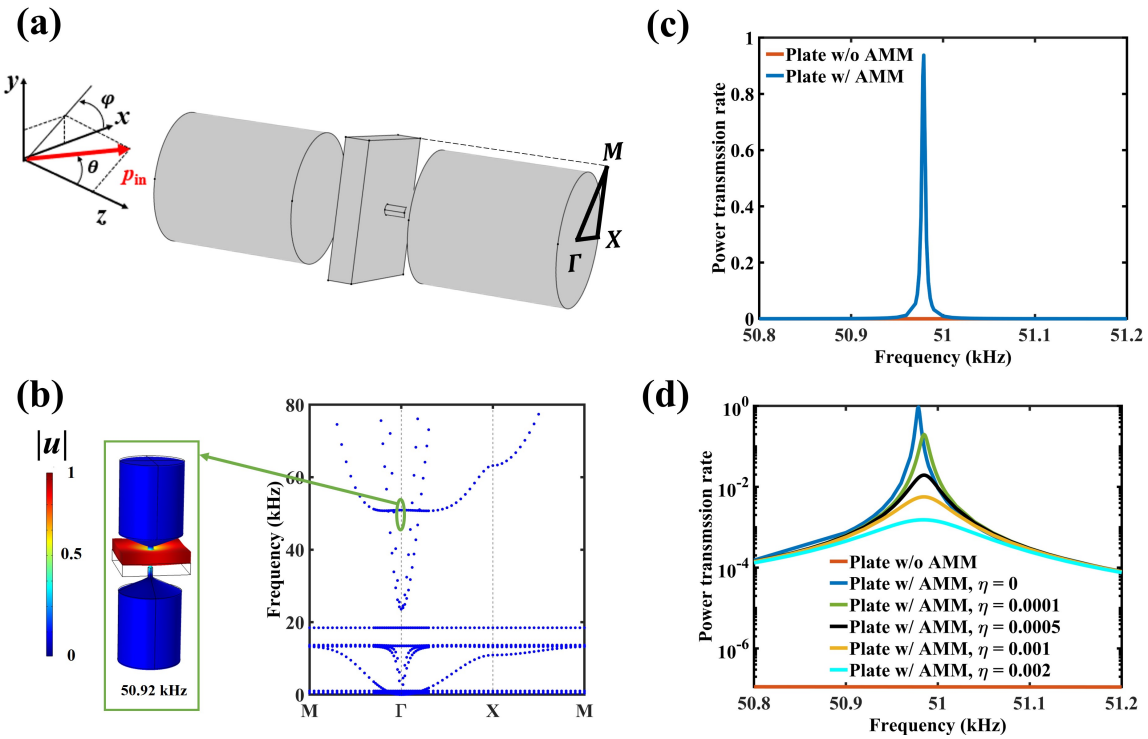

Figure 5.10. Design of the double-sided pillar-based metamaterial for the power transmission enhancement through a 1 mm metal plate in air at 50 kHz. (a) Schematic of a periodically arranged unit cell under a incident plane wave and the first irreducible Brillouin zone. (b) Band structure. (c) Power transmission rate for the plate w/ and w/O AMM under a normally incident plane wave. (d) The typical loss factor of SUS316L significantly affects the power transmission rate.

5.5.5 The impact of the fabrication errors on the resonance frequency and power transmission rate in simulations

The impact of fabrication errors on the resonance frequency of a pillar is illustrated in **Figure 5.11**. The upper section of the figure shows symmetric (**Fig.5.11**a) and asymmetric (**Fig.5.11**b) pillar shapes, highlighting the influence of asymmetry on the resonance frequency and maximum power transmission rate (**Fig.5.11**c). The lower section of the figure presents an isometric view (**Fig.5.11**d) and a cross-sectional view **Fig.5.11**e) of a non-flat profile cone-shaped pillar. 3D bar graphs depict the variation

of the resonance frequency (**Fig.5.11**f) and the maximum power transmission rate at resonance frequencies (**Fig.5.11**g) with geometric tolerance parameters such as the height (h) and width (w) of the cone shape. The degree of asymmetry does not affect the resonance frequency as long as the mass cylinder is shifted within 2.5% of the mass diameter. Furthermore, the maximum power transmission rate remains unaffected, with changes of less than 0.02%. Although there is relatively noticeable deviation in resonance frequency and power transmission rate due to geometric tolerance, the variations are still acceptable. The non-flat profile cone-shaped pillar exhibits less than 2% and 3% variations in resonance frequency and power transmission rate, respectively, underscoring its robustness.

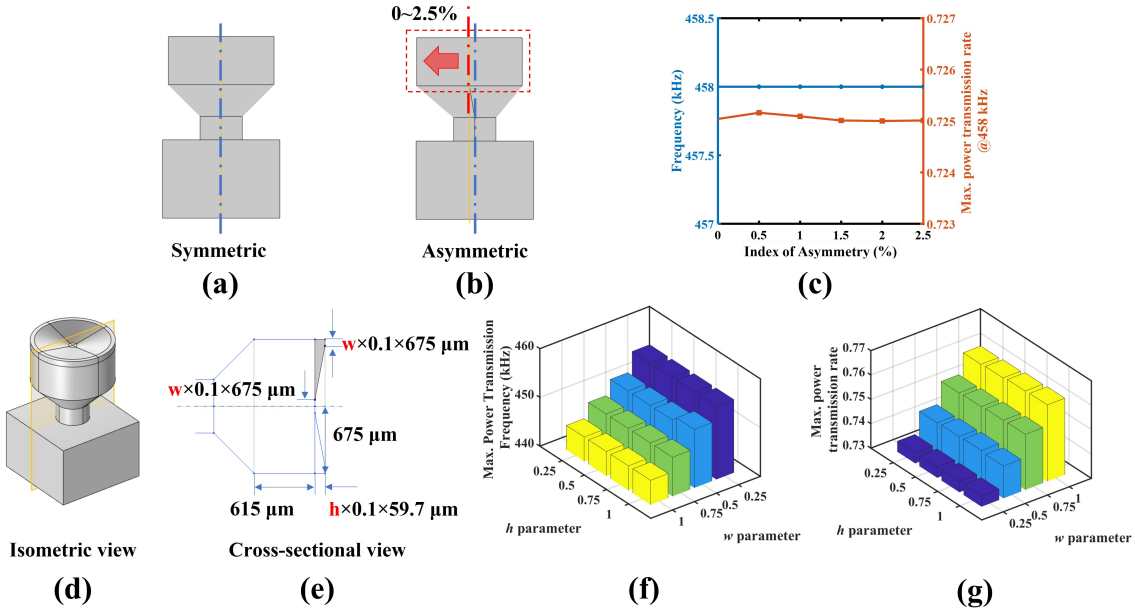

Figure 5.11. Impact of fabrication errors on the resonance frequency of a pillar and its power transmission rate. (Top) (a) Symmetric and (b) asymmetric shapes. (c) Resonance frequency and power transmission rate (at 458 kHz) affected by degree of asymmetry. (Bottom) (d) Isometric and (e) cross-sectional views. (f) Resonance frequency and power transmission rate bars at resonance frequencies dependent on tolerance parameters, h and w, of the cone shape, respectively.

5.5.6 Characteristics of the transmitter

The on-axial pressure field of the unbaffled 1 inch transducer is simulated in COMSOL, and it is compared with the analytical prediction [168] for a baffled piston source at 460 kHz as shown in **Fig.5.3**e. The transducer is modeled by imposing "Incident Pressure

Field" under "Plane Wave Radiation" on a circle with a diameter of 1 inch. The locations of the multiple local extremes in the near field are matched with the predictions, while the magnitude of the normalized pressure is slightly different from the predictions, which is mainly cause by the unbaffled condition.

5.5.7 The impact of the transmitter-sample distance on the power transmission rate in simulations

A series of large sample simulations are conducted to model the real experimental scenarios. Only 10×10 unit cells are modeled in COMSOL with "Symmetry" boundary condition to reduce computational costs, and a workstation with 1 TB memory is used to run the simulations. The non-perfect plane wave from the transducer effect, the finite plate size effect and the wave diffraction effect are considered in the following ways: 1) The transducer is modeled by imposing "Incident Pressure Fiel" under "Plane Wave Radiation" on a quarter of the circle with a diameter of 1 inch. 2) "Fixed Constraint" under "Solid Mechanics" is imposed on the corner of the plate to modal the sample holder in experiments. 3) "Perfectly Matched Layer" is set at the surroundings to reduce the back reflection like the anechoic absorbing layer in experiments.

To evaluate how the transmitter-sample distance d_{tm} affects the power transmission rate in COMSOL, two extreme cases in Figure 3e are considered: $d_{\mathrm{tm}} = 14$ mm in which the plate is placed at the far-est maximum on-axial pressure point, and $d_{\mathrm{tm}} = 9.1$ mm in which the plate is placed at the minimal on-axial pressure point. **Figure 5.12**a shows that the power transmission rate is almost the same for both cases. At the peak power transmission frequency of 460 kHz, a strong transmission can be attained with AMM, as depicted in the pressure distribution for both cases in **Figure 5.12**b.

5.5.8 The measurement of transmitted pressure field

Figure 5.13 illustrates the emitted and received signals by the transducer and hydrophone, respectively, in both the time and frequency domains for various cases. The emitting signal comprises five cycles in each burst, with a frequency of 445 kHz, and the burst period is 1 ms. Here, the signal received at a spatial point located at $(x, y, z) = (0, 0, 45\,\mathrm{mm})$ is presented as an example.

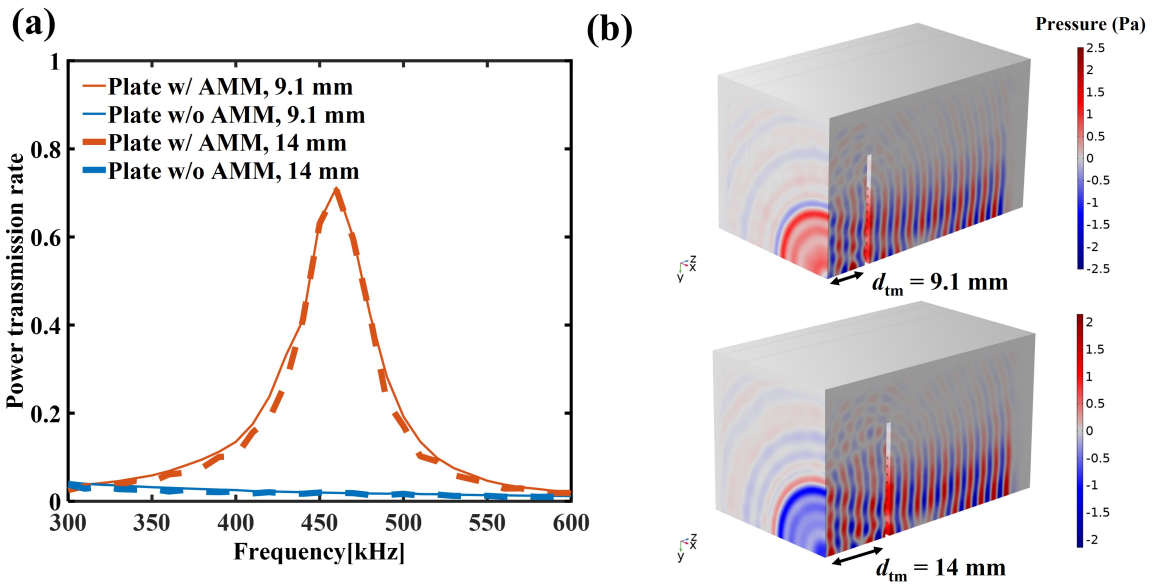

Figure 5.12. (a) The power transmission rate when the plate is placed at the minimal/maximal pressure location in the near field of the transmitter (d_{tm} = 9.1 mm/ 14 mm). (b) The pressure distribution for "Plate w/ AMM" at 460 kHz .

5.5.9 Characteristics of the receiver

Figure 5.14a shows the measured impedance of the 1.5 inch receiver with a resonant frequency around 400 kHz. The magnitude of the measured impedance is 300 Ω at 460 kHz. Next, the optimal power transfer from the receiver to a resistive load is demonstrated in **Figure 5.14**b. Different load resistances (from 50 Ω to 1×10^6 Ω) are connected in series to the receiver, when the 1 inch transmitter is driven by a continuous-mode ultrasound at 460 kHz (which is close to the frequency we are interested to harvest energy). As the load resistance increases, the measured output voltage on the resistor shows a rising tendency and saturates at a higher external load. The instantaneous power output of the receiver is also estimated by $(V_{\text{pp}}^2/(4Z_L))$ [172], where V_{pp} is the peak-to-peak output voltage on the resistive load Z_L. The instantaneous power output reaches the maximal at an external load of 325 Ω, which has a good match with the measured impedance magnitude of the receiver 300 Ω at 460 kHz. The results indicate that the power transfer can be optimal when the impedance between the receiver and the load is matched.

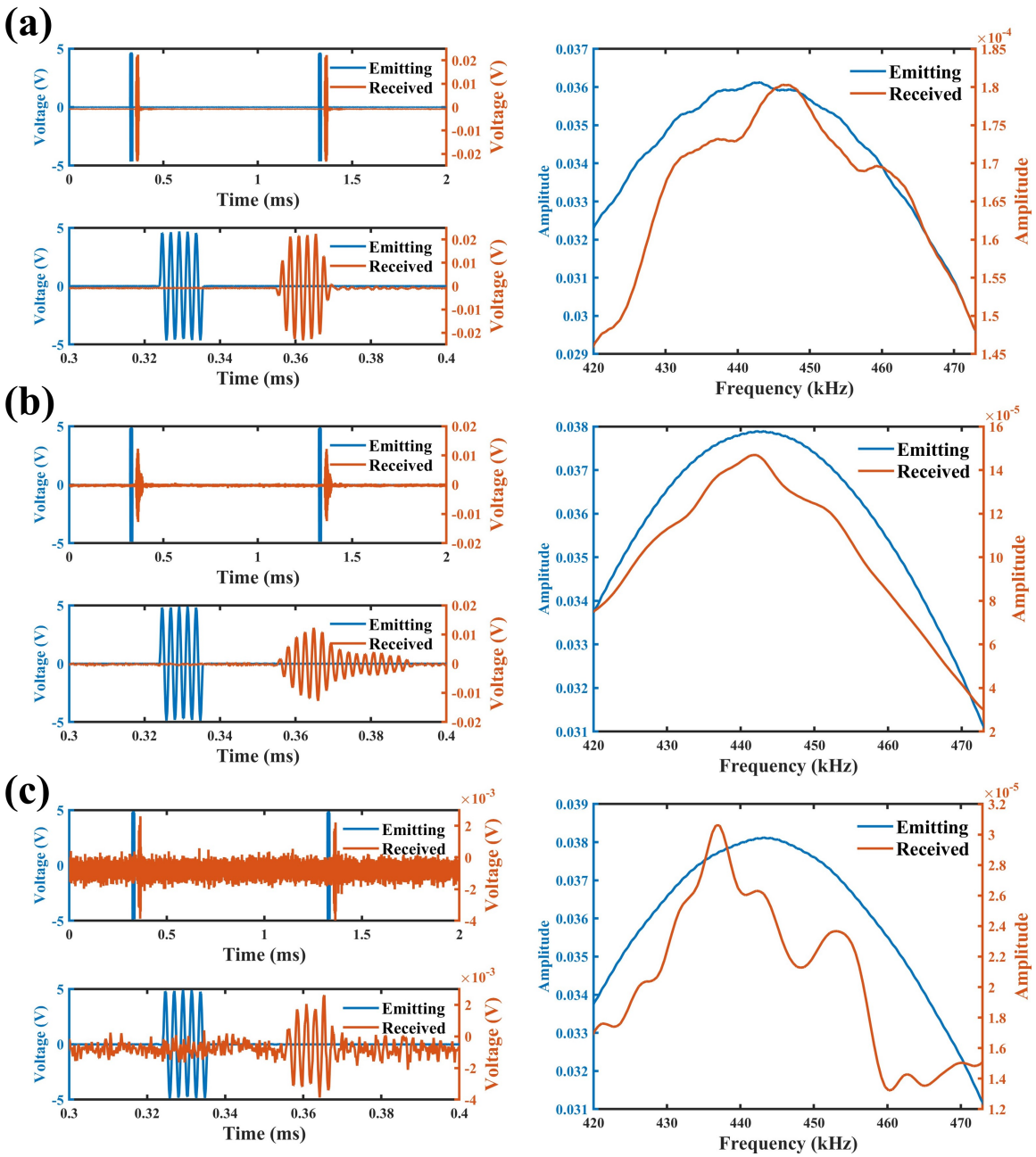

Figure 5.13. The measured emitting and received signals in the time domain (left column) and frequency domain (right column) for three cases: (a) "No plate", (b) "Plate w/ AMM", and (c) "Plate w/o AMM". For time signals, the top panel displays two periods of the burst and the bottom panel displays the zoomed-in signals.

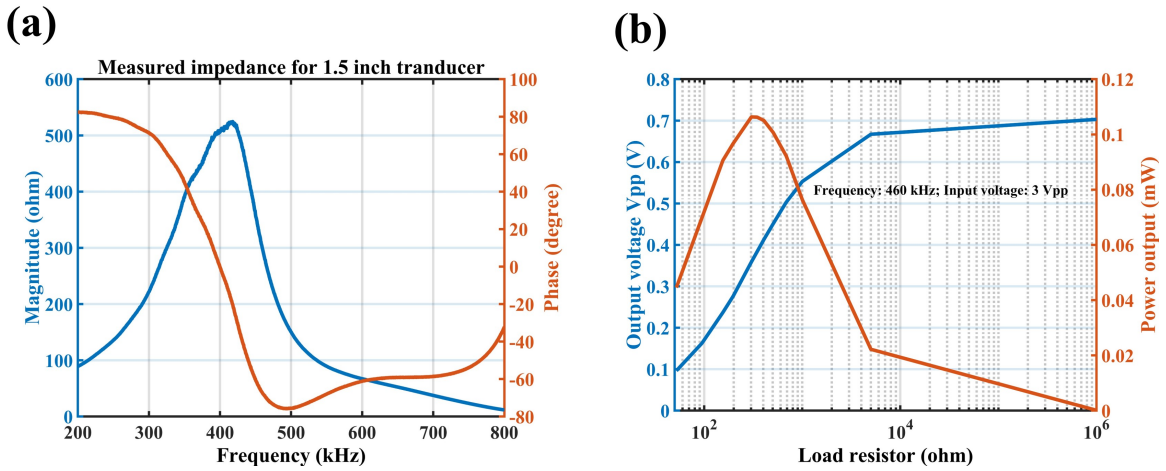

Figure 5.14. (a) The measured impedance of the receiver. (b) The output voltage and power from the receiver to a series-connected resistive load, respectively, showing an optimal output power at 325 Ω.

5.5.10 Design of the energy harvesting circuit

In this work, a circuit has been designed for energy harvesting. The schematic diagram of the circuit is depicted in **Fig. 5.15**. It is implemented on a two-layer printed circuit board (PCB). The traces of the top and bottom layers are shown in **Fig. 5.16**(a) and (c), respectively. The 3D rendering of the PCB and a top-view photo are presented in **Fig. 5.16**(b) and (d), respectively. As shown in **Fig. 5.16**, the PCB can be divided into several functional sections. The top of the PCB houses 9 relays (HUI KE HK19F-DC9V-SHG) that are utilized to switch the wiring for capacitors. Additionally, the middle of the PCB has 10 slots for 220 μF through-hole capacitors. Below the slots is a full bridge rectifier comprising of 4 Schottky diodes (1N5711), and a through-hole red LED is located below the rectifier. The right side of the PCB is equipped with two BNC connectors; the one labeled "INPUT" is connected to the receiving transducer, while the other labeled "OUTPUT" is connected to an oscilloscope. On the left side of the PCB, there is a DC power barrel jack that provides power to the relays. Three switches are located at the bottom left of the PCB. The "SW_WIRING" switch is utilized for switching the wiring of capacitors, the "SW_CHARGE" switch is used for toggling the charging process, and the "SW_LED" switch is used for powering the LED. The designed circuit facilities a more convenient experiment implementation of the energy harvesting compared to existing circuits (e.g., [172]).

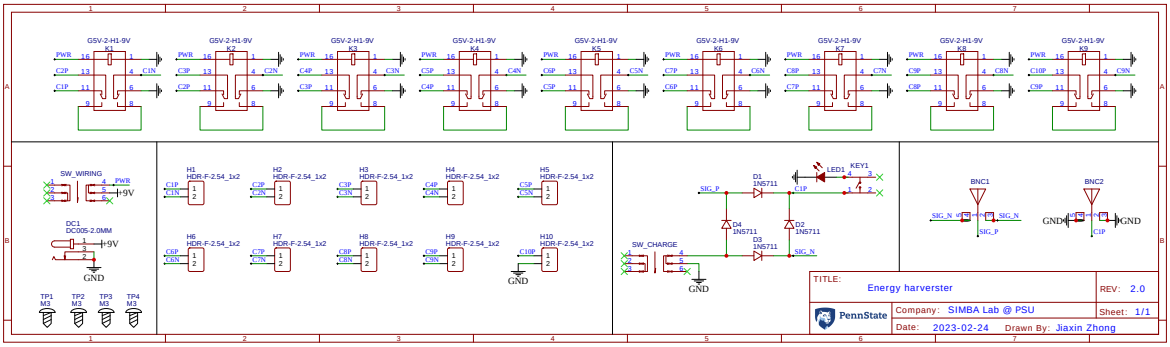

Figure 5.15. Schematic diagram for the energy harvesting circuit.

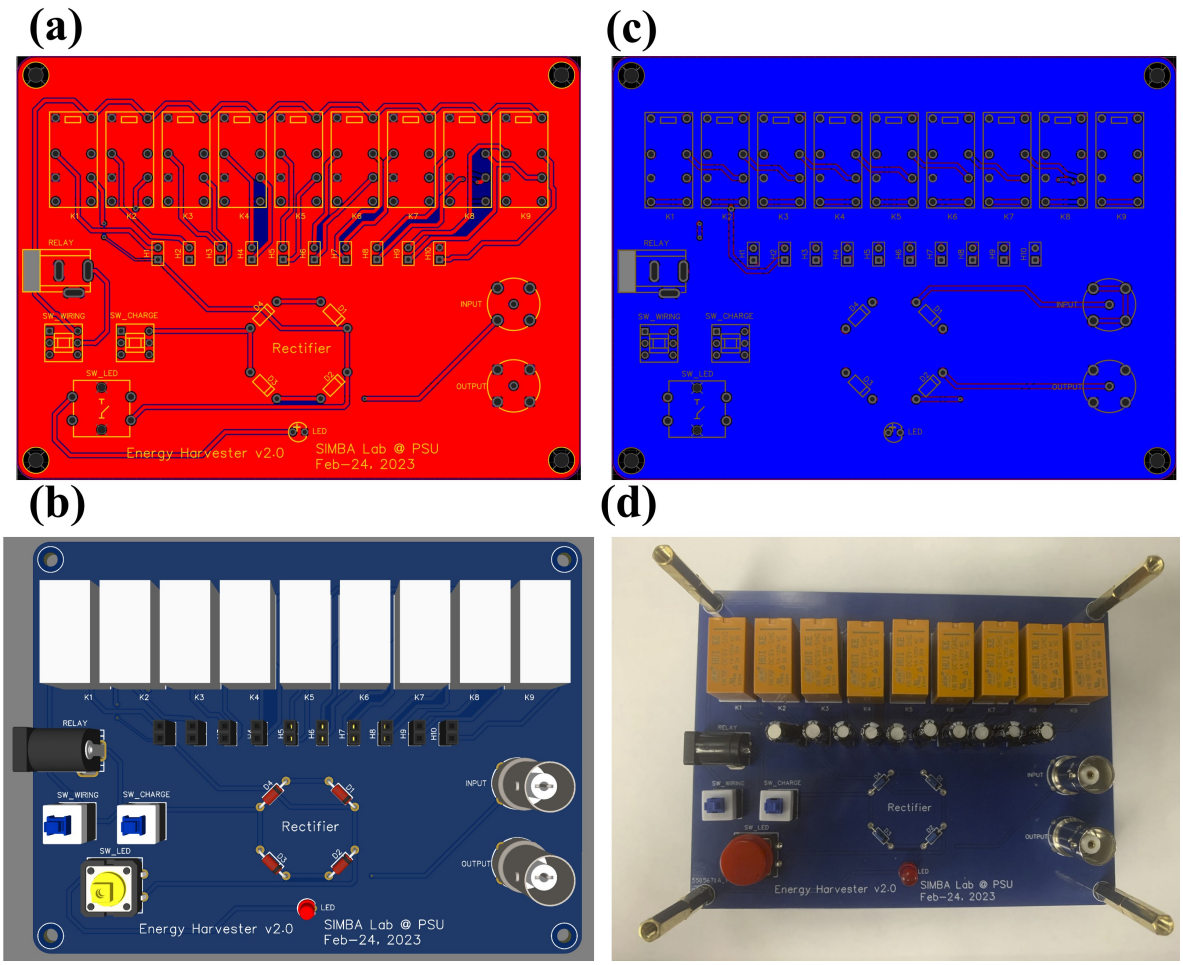

Figure 5.16. The traces of the circuit on (a) the top layer and (b) the bottom layer of the PCB. (c) 3D rendering and (d) the photo of the PCB.

5.6 Methods

5.6.1 Numerical Simulations

The numerical simulations of were performed using the commercial finite element analysis software COMSOL Multiphysics V6.0. The background medium is water(air) with the density and speed of sound being 1,000 (1.21) kg/m^3 and 1,500 (343) m/s, respectively. The metallic plate and acoustic metamaterial are SUS316L with the density ρ_s, Young's modulus E_s, and Poisson's ratio ν_s being 7,910 kg/m^3, 153 GPa, and 0.34, respectively. The equivalent longitudinal speed of sound of SUS316L is $c_l = \sqrt{\frac{K_s+4G_s/3}{\rho_s}} = 5,456\text{m/s}$, where bulk modulus $K_s = E_s/(3(1-2\nu_s))$ and shear modulus $G_s = 0.5E_s/(1+\nu_s)$. The band structure was performed using Solid Mechanics and Pressure Acoustics module where the background medium of water is considered. Plane wave radiation boundary condition is applied at both incoming and outgoing planes so that a complex-valued band structure is obtained. Transmission analysis was performed using Pressure Acoustics and Solid Mechanics modules.

5.6.2 Sample Fabrications

The sample was fabricated using a commercial 3D printer (Metal 3D Printer ProX™ DMP300) and was based on Selective Laser Sintering (SLS) technology. The printing material is SUS316L, with a nominal resolution of 0.15 mm.

5.6.3 Experimental Measurements

In the experiment, a 15 in × 23 in × 14 in water tank was used. It was equipped with LC series 3 axes linear stages and a 3 axes stepper motor controller (Newmark Systems, Inc.), travel range 400 mm × 400 mm × 400 mm. The stages were automatically controlled through the programmed code to scan the space. The tank was filled with approximately 7 gallons of deionized water (DI water) and degassed using a water pump and vacuum pump to remove any air bubbles. Unfocused transducers (with a diameter of 1 in and 1.5 in) centered at approximately 500 kHz (Olympus) were used as a transmitter and a receiver. To map the acoustic power distribution, a needle hydrophone (Onda Corps. HNR 0500) with a diameter of 2.5 mm and frequency range of 0.25-10 MHz was used. The transmitter was connected to the arbitrary waveform generator (Agilent 33250A). The receiver and hydrophone were connected to the oscilloscope (Tektronics MDO 3024

Mixed Domain Oscilloscope) to acquire and process the signals. To minimize unwanted reflections and echoes, an anechoic absorbing layer of Aptflex F28 from Acoustic Polymers Ltd was attached to the back wall and the post where the hydrophone mounted to. Aptflex F28 is a pre-cast polyurethane sheet that is micro-bubble filled, with density and wave speed similar to that of water. It exhibits high transmission loss ($>$ 30dB/cm/MHz) and High echo-reduction ($>$ 42dB at 1 MHz). The alignment between a source, sample, and receiver was achieved by a laser alignment.

For WC-UPT shown in the video, the transmitter was connected to the function generator Agilent 33250A, and the AC signals on the transmitter and receiver were measured by the oscilloscope. The multi-meter was used to monitor the DC voltage on the capacitors. The actual voltage applied to the transmitter is twice of the value indicated on the screen of the function generator. This is because the function generator assumes a loading impedance of $50\,\Omega$, whereas the impedance of the transmitter far surpasses the internal impedance of the function generator ($50\,\Omega$). All capacitors were connected in parallel and charged when the "SW_CHARGE" switch button was pressed down, while the "SW_WIRING" switch button was not pressed. Once the capacitors were fully charged, the "SW_CHARGE" switch was released to stop the charging process. By pressing down the "SW_WIRING" switch, all capacitors were wired in series. Finally, the "SW_LED" switch button was pressed down to power the LED. More details about the buttons on the circuit board are referred to **Section 5.5.10**.

For WC-UDT, the discrete time-domain signal with ASK modulation was first generated in MATLAB and then imported into the arbitrary waveform generator (AWG) interface of PicoScope 5442D in order to be fed into the transmitting transducer. The AC signals on the transmitter and receiver were measured by the same oscilloscope.

5.7 Conclusions

In summary, we have proposed a pillar-based acoustic metamaterial that enables wireless and contactless ultrasound power transfer and data transmission through a metallic plate without any openings. A deterministic method based on band structure theory and transmission analyses is utilized to guide the design procedure. The proposed design is numerically and experimentally verified when the ambient medium is water. Our work not only expands applications for acoustic metamaterial research and 3D metal printing technology, but also sets the direction for the development of next generation of through-metal-wall ultrasonic power transfer and data transmission.

Chapter 6
Conclusions and Future Directions

6.1 Research Conclusions

While the majority of the research in acoustic metamaterials and metasurfaces are curiosity-driven and have shown promising progress in overcoming the fundamental physical limitations of acoustics, there has been a scarcity of acoustic metamaterials research that can have a direct and immediate impact on real-world applications.

This thesis makes contributions to the fields of acoustic metamaterials by examining the challenges of some real-world applications at audio and ultrasound frequencies and putting forward novel metamaterial-based acoustic devices that overcome these limitations. To be more specific, the contributions of this thesis are summarized in a chapter-chapter manner:

- In chapter 2, we tackled the ultra-low frequency (below 100 Hz) sound absorption problem, which is a long-standing issue in room acoustics. We demonstrated a low-frequency broadband, high absorption, near-omnidirectional acoustic metasurface absorber at a deep subwavelenth thickness guided by the causality limit.

- In chapter 3, we extended the sound absorption in room acoustics to HVAC system, fundamentally from a one-port system without acoustic transmission to a two-ports system with acoustic transmission. We demonstrated that a near-perfect absorption (99% absorption) can be realized when the spatial period of monopole-dipole resonators is close to one working wavelength (95% of the wavelength). The condition for perfect absorption is to render degenerate monopole-dipole resonators critically coupled.

- In chapter 4, we studied the radiation problem of acoustic transducers, which is another challenging issue at low audio frequency band. We achieved a 3–7 dB broadband sound pressure level (SPL) improvement of acoustic radiation in the

bass range (50–700 Hz), by leveraging the resonant coupling effect between the transducer and metamaterial resonances,

- In chapter 5, we shifted from airborne acoustics at low audio frequency to underwater applications at ultrasound frequency. One of the application challenges along this direction is the weak ultrasound transmission through a metallic wall due to the significant impedance mismatch between water and the wall, which impedes wireless ultrasonic power transfer and data transmission in aeronautic and aerospace engineering and nuclear engineering. We designed a pillar-based acoustic metamaterial which enables wireless and contactless ultrasonic power transfer and data transmission through a metallic wall, by leveraging the pillar's vertical elongation mode.

6.2 Future Work

The work in the dissertation leads to several potential future research directions.

- In chapter 2, acoustic metasurfaces have made it possible to achieve high-efficiency, deep-subwavelength, broadband absorbers. However, there are multiple directions to explore in the projects. First, the experimental validation of absorption performance is only conducted for the normal incidence in an impedance tube. The experimental validation for the oblique angle of incidence has been scarce in the field of acoustic metamaterial, which could be done in a reverberation chamber. Second, the enhanced absorption due to the coupling between different resonators relied on optimization algorithms. A deterministic method based on coupled-mode theory [85] could be used to systematically study how the coupling can further improve the absorption and its bandwidth. Third, recent studies have shown that acoustic soft boundaries in sound-absorbing materials can achieve novel absorption performance that cannot be realized by that with acoustically hard backings [173]. Further explorations in this direction shows promise for innovative sound-absorbing materials.

- In chapter 3, a near-perfect absorption (99% absorption) has been numerically demonstrated at the sparseness limit (i.e., the spatial period of monopole-dipole resonators is close to one working wavelength). A experimental demonstration is expected for a design less sensitive to angle of incidence. One could use rigid walls as a special kind of periodic condition instead of the Floquet periodic boundary

condition, which is what we are using now in the numerical model. This would render the problem an absorption problem in a waveguide with only a few propagation modes, i.e., discrete incident wave components. In addition, porous materials with high dissipation loss could be used to broaden the absorption bandwidth to make the design less sensitive to the incident angle. Coupling multiple different monopole-dipole resonators could be helpful to make it a broadband absorption.

- In chapter 4, the input voltage has been set small to ensure the whole model is linear. In real scenario, a large input voltage may induce nonlinear effect, which should be studied to ensure the metamaterial design can still lead to a broadband radiation enhancement. In addition, more detailed comparison with other folded horn/transmission line/waveguide designs (e.g., Bose's Acoustic Waveguide speaker technology) will be helpful to distinguish our resonances-coupling design from existing folded acoustic designs.

- In chapter 5, the wireless and contactless ultrasonic power transfer and data transmission through a metallic wall has been demonstrated in water. It would be more challenging yet exciting to demonstrate that in air, where the impedance mismatch between air and metal is much larger. It has been shown in our preliminary study that unlike the waterborne case, the power transmission rate for the airborne case is inherently ultra-sensitive to the loss factor of the constituent material. A careful selection of the printing material with a tiny loss is crucial to the experimentally measurable power transmission enhancement in air. A potential type of material is cermet, which is a composite material composed of ceramic (very small loss) and metal materials. In addition to that, our pillar-based acoustic metamaterial can be combined with additional layers of metasurface to demonstrate more advanced functionalities such as through-metal-wall acoustic hologram/levitation/haptics/tweezers/distributed sensor networks.

Bibliography

[1] Cummer, S. A., J. Christensen, and A. Alù (2016) "Controlling sound with acoustic metamaterials," *Nature Reviews Materials*, **1**(3), pp. 1–13.

[2] Yablonovitch, E. and T. Gmitter (1989) "Photonic band structure: The face-centered-cubic case," *Physical Review Letters*, **63**(18), p. 1950.

[3] Kushwaha, M. S., P. Halevi, L. Dobrzynski, and B. Djafari-Rouhani (1993) "Acoustic band structure of periodic elastic composites," *Physical review letters*, **71**(13), p. 2022.

[4] Yablonovitch, E. (1987) "Inhibited spontaneous emission in solid-state physics and electronics," *Physical review letters*, **58**(20), p. 2059.

[5] Sigalas, M. and E. N. Economou (1993) "Band structure of elastic waves in two dimensional systems," *Solid state communications*, **86**(3), pp. 141–143.

[6] Martínez-Sala, R., J. Sancho, J. V. Sánchez, V. Gómez, J. Llinares, and F. Meseguer (1995) "Sound attenuation by sculpture," *nature*, **378**(6554), pp. 241–241.

[7] De Espinosa, F. M., E. Jimenez, and M. Torres (1998) "Ultrasonic band gap in a periodic two-dimensional composite," *Physical Review Letters*, **80**(6), p. 1208.

[8] Ma, G. and P. Sheng (2016) "Acoustic metamaterials: From local resonances to broad horizons," *Science advances*, **2**(2), p. e1501595.

[9] Pendry, J. B., A. Holden, W. Stewart, and I. Youngs (1996) "Extremely low frequency plasmons in metallic mesostructures," *Physical review letters*, **76**(25), p. 4773.

[10] Shelby, R. A., D. R. Smith, and S. Schultz (2001) "Experimental verification of a negative index of refraction," *science*, **292**(5514), pp. 77–79.

[11] Liu, Z., X. Zhang, Y. Mao, Y. Zhu, Z. Yang, C. T. Chan, and P. Sheng (2000) "Locally resonant sonic materials," *science*, **289**(5485), pp. 1734–1736.

[12] Li, J. and C. T. Chan (2004) "Double-negative acoustic metamaterial," *Physical Review E*, **70**(5), p. 055602.

[13] Fok, L. and X. Zhang (2011) "Negative acoustic index metamaterial," *Physical Review B*, **83**(21), p. 214304.

[14] Lee, S. H., C. M. Park, Y. M. Seo, Z. G. Wang, and C. K. Kim (2010) "Composite acoustic medium with simultaneously negative density and modulus," *Physical review letters*, **104**(5), p. 054301.

[15] Chen, H. and C. T. Chan (2007) "Acoustic cloaking in three dimensions using acoustic metamaterials," *Applied physics letters*, **91**(18).

[16] Cummer, S. A., B.-I. Popa, D. Schurig, D. R. Smith, J. Pendry, M. Rahm, and A. Starr (2008) "Scattering theory derivation of a 3D acoustic cloaking shell," *Physical review letters*, **100**(2), p. 024301.

[17] Li, J., L. Fok, X. Yin, G. Bartal, and X. Zhang (2009) "Experimental demonstration of an acoustic magnifying hyperlens," *Nature materials*, **8**(12), pp. 931–934.

[18] Kaina, N., F. Lemoult, M. Fink, and G. Lerosey (2015) "Negative refractive index and acoustic superlens from multiple scattering in single negative metamaterials," *Nature*, **525**(7567), pp. 77–81.

[19] Haberman, M. R. and M. D. Guild (2016) "Acoustic metamaterials," *Physics Today*, **69**(6), pp. 42–48.

[20] Mangulis, V. (1964) "Kramers-Kronig or Dispersion Relations in Acoustics," *The Journal of the Acoustical Society of America*, **36**(1), pp. 211–212.

[21] Popa, B.-I., L. Zigoneanu, and S. A. Cummer (2013) "Tunable active acoustic metamaterials," *Physical Review B*, **88**(2), p. 024303.

[22] Willatzen, M. and J. Christensen (2014) "Acoustic gain in piezoelectric semiconductors at ϵ-near-zero response," *Physical Review B*, **89**(4), p. 041201.

[23] Fleury, R., D. Sounas, and A. Alù (2015) "An invisible acoustic sensor based on parity-time symmetry," *Nature communications*, **6**(1), p. 5905.

[24] Bender, C. M. (2007) "Making sense of non-Hermitian Hamiltonians," *Reports on Progress in Physics*, **70**(6), p. 947.

[25] Zhu, X., H. Ramezani, C. Shi, J. Zhu, and X. Zhang (2014) "P t-symmetric acoustics," *Physical Review X*, **4**(3), p. 031042.

[26] Fleury, R., D. L. Sounas, C. F. Sieck, M. R. Haberman, and A. Alù (2014) "Sound isolation and giant linear nonreciprocity in a compact acoustic circulator," *Science*, **343**(6170), pp. 516–519.

[27] Fleury, R., D. L. Sounas, and A. Alù (2015) "Subwavelength ultrasonic circulator based on spatiotemporal modulation," *Physical Review B*, **91**(17), p. 174306.

[28] Liang, B., B. Yuan, and J.-c. Cheng (2009) "Acoustic diode: Rectification of acoustic energy flux in one-dimensional systems," *Physical review letters*, **103**(10), p. 104301.

[29] Liang, B., X. Guo, J. Tu, D. Zhang, and J. Cheng (2010) "An acoustic rectifier," *Nature materials*, **9**(12), pp. 989–992.

[30] Assouar, B., B. Liang, Y. Wu, Y. Li, J.-C. Cheng, and Y. Jing (2018) "Acoustic metasurfaces," *Nature Reviews Materials*, **3**(12), pp. 460–472.

[31] Yu, N., P. Genevet, M. A. Kats, F. Aieta, J.-P. Tetienne, F. Capasso, and Z. Gaburro (2011) "Light propagation with phase discontinuities: generalized laws of reflection and refraction," *science*, **334**(6054), pp. 333–337.

[32] Xie, Y., W. Wang, H. Chen, A. Konneker, B.-I. Popa, and S. A. Cummer (2014) "Wavefront modulation and subwavelength diffractive acoustics with an acoustic metasurface," *Nature communications*, **5**(1), p. 5553.

[33] Li, Y., X. Jiang, B. Liang, J.-c. Cheng, and L. Zhang (2015) "Metascreen-based acoustic passive phased array," *Physical Review Applied*, **4**(2), p. 024003.

[34] Zhu, J., J. Christensen, J. Jung, L. Martin-Moreno, X. Yin, L. Fok, X. Zhang, and F. Garcia-Vidal (2011) "A holey-structured metamaterial for acoustic deep-subwavelength imaging," *Nature physics*, **7**(1), pp. 52–55.

[35] Liang, Z. and J. Li (2012) "Extreme acoustic metamaterial by coiling up space," *Physical review letters*, **108**(11), p. 114301.

[36] Li, Y., C. Shen, Y. Xie, J. Li, W. Wang, S. A. Cummer, and Y. Jing (2017) "Tunable asymmetric transmission via lossy acoustic metasurfaces," *Physical review letters*, **119**(3), p. 035501.

[37] Wang, X., X. Fang, D. Mao, Y. Jing, and Y. Li (2019) "Extremely asymmetrical acoustic metasurface mirror at the exceptional point," *Physical review letters*, **123**(21), p. 214302.

[38] Ma, G., M. Yang, S. Xiao, Z. Yang, and P. Sheng (2014) "Acoustic metasurface with hybrid resonances," *Nature materials*, **13**(9), pp. 873–878.

[39] Yang, M., S. Chen, C. Fu, and P. Sheng (2017) "Optimal sound-absorbing structures," *Materials Horizons*, **4**(4), pp. 673–680.

[40] Yang, M., C. Meng, C. Fu, Y. Li, Z. Yang, and P. Sheng (2015) "Subwavelength total acoustic absorption with degenerate resonators," *Applied Physics Letters*, **107**(10).

[41] Zhu, Y. and B. Assouar (2019) "Multifunctional acoustic metasurface based on an array of Helmholtz resonators," *Physical review B*, **99**(17), p. 174109.

[42] Cox, T. J. and P. D'antonio (2009) *Acoustic absorbers and diffusers: theory, design and application*, Crc Press.

[43] Nark, D. M., M. G. Jones, and D. L. Sutliff (2018) "Broadband inlet liner design for the DGEN aero-propulsion research turbofan," in *2018 AIAA/CEAS Aeroacoustics Conference*, p. 3608.

[44] Fuchs, H., X. Zha, X. Zhou, and H. Drotleff (2001) "Creating low-noise environments in communication rooms," *Applied Acoustics*, **62**(12), pp. 1375–1396.

[45] Błaszak, M. (2008) "Acoustic design of small rectangular rooms: Normal frequency statistics," *Applied Acoustics*, **69**(12), pp. 1356–1360.

[46] Rivet, E., R. Boulandet, H. Lissek, and I. Rigas (2012) "Study on room modal equalization at low frequencies with electroacoustic absorbers," in *Acoustics 2012*.

[47] Lau, S.-K. and E. A. Powell (2018) "Effects of absorption placement on sound field of a rectangular room: A statistical approach," *Journal of Low Frequency Noise, Vibration and Active Control*, **37**(2), pp. 394–406.

[48] Yang, M. and P. Sheng (2017) "Sound absorption structures: From porous media to acoustic metamaterials," *Annual Review of Materials Research*, **47**, pp. 83–114.

[49] Ge, H., M. Yang, C. Ma, M.-H. Lu, Y.-F. Chen, N. Fang, and P. Sheng (2018) "Breaking the barriers: Advances in acoustic functional materials," *National Science Review*, **5**(2), pp. 159–182.

[50] Gerard, N. J. and Y. Jing (2020) "Loss in acoustic metasurfaces: a blessing in disguise," *MRS Communications*, **10**(1), pp. 32–41.

[51] Mei, J., G. Ma, M. Yang, Z. Yang, W. Wen, and P. Sheng (2012) "Dark acoustic metamaterials as super absorbers for low-frequency sound," *Nature communications*, **3**(1), p. 756.

[52] Maa, D.-Y. (1998) "Potential of microperforated panel absorber," *the Journal of the Acoustical Society of America*, **104**(5), pp. 2861–2866.

[53] Cai, X., Q. Guo, G. Hu, and J. Yang (2014) "Ultrathin low-frequency sound absorbing panels based on coplanar spiral tubes or coplanar Helmholtz resonators," *Applied Physics Letters*, **105**(12).

[54] Li, Y. and B. M. Assouar (2016) "Acoustic metasurface-based perfect absorber with deep subwavelength thickness," *Applied Physics Letters*, **108**(6).

[55] Huang, S., X. Fang, X. Wang, B. Assouar, Q. Cheng, and Y. Li (2018) "Acoustic perfect absorbers via spiral metasurfaces with embedded apertures," *Applied Physics Letters*, **113**(23).

[56] ——— (2019) "Acoustic perfect absorbers via Helmholtz resonators with embedded apertures," *The Journal of the Acoustical Society of America*, **145**(1), pp. 254–262.

[57] Simon, F. (2018) "Long elastic open neck acoustic resonator for low frequency absorption," *Journal of Sound and Vibration*, **421**, pp. 1–16.

[58] Donda, K., Y. Zhu, S.-W. Fan, L. Cao, Y. Li, and B. Assouar (2019) "Extreme low-frequency ultrathin acoustic absorbing metasurface," *Applied Physics Letters*, **115**(17).

[59] Romero-García, V., G. Theocharis, O. Richoux, and V. Pagneux (2016) "Use of complex frequency plane to design broadband and sub-wavelength absorbers," *The Journal of the Acoustical Society of America*, **139**(6), pp. 3395–3403.

[60] Romero-García, V., G. Theocharis, O. Richoux, A. Merkel, V. Tournat, and V. Pagneux (2016) "Perfect and broadband acoustic absorption by critically coupled sub-wavelength resonators," *Scientific reports*, **6**(1), p. 19519.

[61] Leroy, V., A. Strybulevych, M. Lanoy, F. Lemoult, A. Tourin, and J. H. Page (2015) "Superabsorption of acoustic waves with bubble metascreens," *Physical Review B*, **91**(2), p. 020301.

[62] Lee, T. and H. Iizuka (2018) "Heavily overdamped resonance structurally engineered in a grating metasurface for ultra-broadband acoustic absorption," *Applied Physics Letters*, **113**(10).

[63] Peng, X., J. Ji, and Y. Jing (2018) "Composite honeycomb metasurface panel for broadband sound absorption," *The Journal of the Acoustical Society of America*, **144**(4), pp. EL255–EL261.

[64] Wang, C. and L. Huang (2011) "On the acoustic properties of parallel arrangement of multiple micro-perforated panel absorbers with different cavity depths," *The Journal of the Acoustical Society of America*, **130**(1), pp. 208–218.

[65] Huang, S., Z. Zhou, D. Li, T. Liu, X. Wang, J. Zhu, and Y. Li (2020) "Compact broadband acoustic sink with coherently coupled weak resonances," *Science Bulletin*, **65**(5), pp. 373–379.

[66] Kim, S., Y.-H. Kim, and J.-H. Jang (2006) "A theoretical model to predict the low-frequency sound absorption of a Helmholtz resonator array," *The Journal of the Acoustical Society of America*, **119**(4), pp. 1933–1936.

[67] Mosa, A. I., A. Putra, R. Ramlan, I. Prasetiyo, and A.-A. Esraa (2019) "Theoretical model of absorption coefficient of an inhomogeneous MPP absorber with multi-cavity depths," *Applied Acoustics*, **146**, pp. 409–419.

[68] Li, J., W. Wang, Y. Xie, B.-I. Popa, and S. A. Cummer (2016) "A sound absorbing metasurface with coupled resonators," *Applied Physics Letters*, **109**(9).

[69] Jiménez, N., V. Romero-García, V. Pagneux, and J.-P. Groby (2017) "Rainbow-trapping absorbers: Broadband, perfect and asymmetric sound absorption by subwavelength panels for transmission problems," *Scientific reports*, **7**(1), p. 13595.

[70] Zhu, Y., K. Donda, S. Fan, L. Cao, and B. Assouar (2019) "Broadband ultra-thin acoustic metasurface absorber with coiled structure," *Applied Physics Express*, **12**(11), p. 114002.

[71] Liu, C. R., J. H. Wu, X. Chen, and F. Ma (2019) "A thin low-frequency broadband metasurface with multi-order sound absorption," *Journal of Physics D: Applied Physics*, **52**(10), p. 105302.

[72] Kim, Y.-H. (2010) *Sound propagation: an impedance based approach*, John Wiley & Sons.

[73] Sui, N. (2017) *Sound-proof sandwich panel design via metamaterial concept*, North Carolina State University.

[74] Lepetit, T. and B. Kanté (2014) "Controlling multipolar radiation with symmetries for electromagnetic bound states in the continuum," *Physical Review B*, **90**(24), p. 241103.

[75] Verslegers, L., Z. Yu, Z. Ruan, P. B. Catrysse, and S. Fan (2012) "From electromagnetically induced transparency to superscattering with a single structure: a coupled-mode theory for doubly resonant structures," *Physical review letters*, **108**(8), p. 083902.

[76] Suh, W., Z. Wang, and S. Fan (2004) "Temporal coupled-mode theory and the presence of non-orthogonal modes in lossless multimode cavities," *IEEE Journal of Quantum Electronics*, **40**(10), pp. 1511–1518.

[77] Stinson, M. R. and E. Shaw (1985) "Acoustic impedance of small, circular orifices in thin plates," *The Journal of the Acoustical Society of America*, **77**(6), pp. 2039–2042.

[78] Stinson, M. R. (1991) "The propagation of plane sound waves in narrow and wide circular tubes, and generalization to uniform tubes of arbitrary cross-sectional shape," *The Journal of the Acoustical Society of America*, **89**(2), pp. 550–558.

[79] Panton, R. L. and J. M. Miller (1975) "Resonant frequencies of cylindrical Helmholtz resonators," *The Journal of the Acoustical Society of America*, **57**(6), pp. 1533–1535.

[80] Weston, D. (1953) "The theory of the propagation of plane sound waves in tubes," *Proceedings of the Physical Society. Section B*, **66**(8), p. 695.

[81] Zwikker, C. and C. W. Kosten (1949) "Sound absorbing materials," *(No Title)*.

[82] Ingard, U. (2009) *Noise reduction analysis*, Jones & Bartlett Publishers.

[83] Wang, C., L. Huang, and Y. Zhang (2014) "Oblique incidence sound absorption of parallel arrangement of multiple micro-perforated panel absorbers in a periodic pattern," *Journal of Sound and Vibration*, **333**(25), pp. 6828–6842.

[84] Lee, T. and H. Iizuka (2019) "Acoustic resonance coupling for directional wave control: from angle-dependent absorption to asymmetric transmission," *New Journal of Physics*, **21**(4), p. 043030.

[85] Ding, K., G. Ma, M. Xiao, Z. Zhang, and C. T. Chan (2016) "Emergence, coalescence, and topological properties of multiple exceptional points and their experimental realization," *Physical Review X*, **6**(2), p. 021007.

[86] Huang, S., T. Liu, Z. Zhou, X. Wang, J. Zhu, and Y. Li (2020) "Extreme sound confinement from quasibound states in the continuum," *Physical Review Applied*, **14**(2), p. 021001.

[87] Dong, R., M. Sun, F. Mo, D. Mao, X. Wang, and Y. Li (2021) "Recent advances in acoustic ventilation barriers," *Journal of Physics D: Applied Physics*, **54**(40), p. 403002.

[88] Wang, C., L. Cheng, and L. Huang (2008) "Realization of a broadband low-frequency plate silencer using sandwich plates," *Journal of sound and vibration*, **318**(4-5), pp. 792–808.

[89] Ge, Y., H.-x. Sun, S.-q. Yuan, and Y. Lai (2019) "Switchable omnidirectional acoustic insulation through open window structures with ultrathin metasurfaces," *Physical Review Materials*, **3**(6), p. 065203.

[90] Cheng, Y., C. Zhou, B. Yuan, D. Wu, Q. Wei, and X. Liu (2015) "Ultra-sparse metasurface for high reflection of low-frequency sound based on artificial Mie resonances," *Nature materials*, **14**(10), pp. 1013–1019.

[91] He, J., Z. Zhou, C. Zhang, Y. Zheng, Y. Li, Y. Li, X. Jiang, and D. Ta (2022) "Ultrasparse and omnidirectional acoustic ventilated meta-barrier," *Applied Physics Letters*, **120**(19).

[92] Sun, M., X. Fang, D. Mao, X. Wang, and Y. Li (2020) "Broadband acoustic ventilation barriers," *Physical Review Applied*, **13**(4), p. 044028.

[93] Dong, R., D. Mao, X. Wang, and Y. Li (2021) "Ultrabroadband acoustic ventilation barriers via hybrid-functional metasurfaces," *Physical Review Applied*, **15**(2), p. 024044.

[94] Liu, C., J. Shi, W. Zhao, X. Zhou, C. Ma, R. Peng, M. Wang, Z. H. Hang, X. Liu, J. Christensen, et al. (2021) "Three-dimensional soundproof acoustic metacage," *Physical Review Letters*, **127**(8), p. 084301.

[95] Long, H., Y. Zhu, Y. Gu, Y. Cheng, and X. Liu (2022) "Inverse design of an ultrasparse dissipated-sound metacage by using a genetic algorithm," *Physical Review Applied*, **18**(4), p. 044032.

[96] Shen, C., Y. Xie, J. Li, S. A. Cummer, and Y. Jing (2018) "Acoustic metacages for sound shielding with steady air flow," *Journal of Applied Physics*, **123**(12).

[97] Astley, R. and A. Cummings (1987) "A finite element scheme for attenuation in ducts lined with porous material: comparison with experiment," *Journal of Sound and Vibration*, **116**(2), pp. 239–263.

[98] Yu, X., L. Cheng, and X. You (2015) "Hybrid silencers with micro-perforated panels and internal partitions," *The Journal of the Acoustical Society of America*, **137**(2), pp. 951–962.

[99] Yu, X., S.-K. Lau, L. Cheng, and F. Cui (2017) "A numerical investigation on the sound insulation of ventilation windows," *Applied Acoustics*, **117**, pp. 113–121.

[100] Lee, I., A. Selamet, and N. T. Huff (2006) "Impact of perforation impedance on the transmission loss of reactive and dissipative silencers," *The Journal of the Acoustical Society of America*, **120**(6), pp. 3706–3713.

[101] Badreddine, A., B. Liang, Y. Wu, Y. Li, J. Cheng, and Y. Jing (2018) "Acoustic metasurfaces," *Nat. Rev. Mater.*, **3**(12), pp. 460–472.

[102] Li, L.-j., B. Zheng, L.-m. Zhong, J. Yang, B. Liang, and J.-c. Cheng (2018) "Broadband compact acoustic absorber with high-efficiency ventilation performance," *Applied Physics Letters*, **113**(10).

[103] Fu, C., X. Zhang, M. Yang, S. Xiao, and Z. Yang (2017) "Hybrid membrane resonators for multiple frequency asymmetric absorption and reflection in large waveguide," *Applied Physics Letters*, **110**(2).

[104] Xiang, X., X. Wu, X. Li, P. Wu, H. He, Q. Mu, S. Wang, Y. Huang, and W. Wen (2020) "Ultra-open ventilated metamaterial absorbers for sound-silencing applications in environment with free air flows," *Extreme Mechanics Letters*, **39**, p. 100786.

[105] Xiang, X., H. Tian, Y. Huang, X. Wu, and W. Wen (2021) "Manually tunable ventilated metamaterial absorbers," *Applied Physics Letters*, **118**(5).

[106] Lapin, A. (2003) "Monopole-dipole type resonator in a narrow pipe," *Acoustical Physics*, **49**(6), pp. 731–732.

[107] Long, H., Y. Cheng, and X. Liu (2017) "Asymmetric absorber with multiband and broadband for low-frequency sound," *Applied Physics Letters*, **111**(14).

[108] Lee, T., T. Nomura, E. M. Dede, and H. Iizuka (2020) "Asymmetric loss-induced perfect sound absorption in duct silencers," *Applied Physics Letters*, **116**(21).

[109] ——— (2019) "Ultrasparse acoustic absorbers enabling fluid flow and visible-light controls," *Physical Review Applied*, **11**(2), p. 024022.

[110] Su, X. and D. Banerjee (2020) "Extraordinary sound isolation using an ultrasparse array of degenerate anisotropic scatterers," *Physical Review Applied*, **13**(6), p. 064047.

[111] Lapin, A. (2005) "Sound absorption by monopole-dipole resonators in a multimode waveguide," *Acoustical Physics*, **51**(3), pp. 362–364.

[112] Piper, J. R., V. Liu, and S. Fan (2014) "Total absorption by degenerate critical coupling," *Applied Physics Letters*, **104**(25).

[113] Yang, M., Y. Li, C. Meng, C. Fu, J. Mei, Z. Yang, and P. Sheng (2015) "Sound absorption by subwavelength membrane structures: A geometric perspective," *Comptes Rendus Mécanique*, **343**(12), pp. 635–644.

[114] Huang, S., S. Xie, H. Gao, T. Hao, S. Zhang, T. Liu, Y. Li, and J. Zhu (2022) "Acoustic Purcell effect induced by quasibound state in the continuum," *Fundamental Research*.

[115] Motti, V. G. and V. G. Motti (2020) "Introduction to wearable computers," *Wearable interaction*, pp. 1–39.

[116] Bohil, C. J., B. Alicea, and F. A. Biocca (2011) "Virtual reality in neuroscience research and therapy," *Nature reviews neuroscience*, **12**(12), pp. 752–762.

[117] Thompson, M. M., A. Wang, D. Roy, and E. Klopfer (2018) "Authenticity, interactivity, and collaboration in VR learning games," *Frontiers in Robotics and AI*, **5**, p. 133.

[118] Hove, M. J., P. Vuust, and J. Stupacher (2019) "Increased levels of bass in popular music recordings 1955–2016 and their relation to loudness," *The Journal of the Acoustical Society of America*, **145**(4), pp. 2247–2253.

[119] Byrne, D., H. Dillon, K. Tran, S. Arlinger, K. Wilbraham, R. Cox, B. Hagerman, R. Hetu, J. Kei, C. Lui, et al. (1994) "An international comparison of long-term average speech spectra," *The journal of the acoustical society of America*, **96**(4), pp. 2108–2120.

[120] Small, R. H. (1973) "Closed-box loudspeaker systems-part 2: Synthesis," *Journal of the Audio Engineering Society*, **21**(1), pp. 11–18.

[121] ——— (1973) "Vented-box loudspeaker systems–part 1: Small-signal analysis," *Journal of the Audio Engineering Society*, **21**(5), pp. 363–372.

[122] Lemaitre, G., B. Letinturier, and B. Gazengel (2008) "Model and estimation method for predicting the sound radiated by a horn loudspeaker–With application to a car horn," *Applied acoustics*, **69**(1), pp. 47–59.

[123] Backman, J. (2007) "Refinements of transmission line loudspeaker models," in *Audio Engineering Society Convention 122*, Audio Engineering Society.

[124] Hipperson, J., J. Angus, and J. Hargreaves (2018) "A Fast And Efficient Model for Transmission Line Loudspeakers," in *Audio Engineering Society Convention 144*, Audio Engineering Society.

[125] Kim, J., G.-T. Lee, and J. Kim (2011) "A Computational Model of Vented Band-Pass Enclosure Using Transmission Line Enclosure Modeling," in *Audio Engineering Society Convention 131*, Audio Engineering Society.

[126] Chang, J.-R. and C. Wang (2019) "Bass Extension of Microspeaker System on Mobile Device," *Journal of Mechanics*, **35**(4), pp. 487–498.

[127] Cummer, S. A. and D. Schurig (2007) "One path to acoustic cloaking," *New journal of physics*, **9**(3), p. 45.

[128] Norris, A. N. (2008) "Acoustic cloaking theory," *Proceedings of the Royal Society A: Mathematical, Physical and Engineering Sciences*, **464**(2097), pp. 2411–2434.

[129] Zhu, J., Y. Chen, X. Zhu, F. J. Garcia-Vidal, X. Yin, W. Zhang, and X. Zhang (2013) "Acoustic rainbow trapping," *Scientific reports*, **3**(1), p. 1728.

[130] Shi, C., M. Dubois, Y. Chen, L. Cheng, H. Ramezani, Y. Wang, and X. Zhang (2016) "Accessing the exceptional points of parity-time symmetric acoustics," *Nature communications*, **7**(1), p. 11110.

[131] Degraeve, S. and J. Oclee-Brown (2020) "Metamaterial absorber for loudspeaker enclosures," in *Audio Engineering Society Convention 148*, Audio Engineering Society.

[132] Landi, M., J. Zhao, W. E. Prather, Y. Wu, and L. Zhang (2018) "Acoustic Purcell effect for enhanced emission," *Physical review letters*, **120**(11), p. 114301.

[133] Zhang, J., W. Rui, C. Ma, Y. Cheng, X. Liu, and J. Christensen (2021) "Remote whispering metamaterial for non-radiative transceiving of ultra-weak sound," *Nature Communications*, **12**(1), p. 3670.

[134] Mei, J. and Y. Wu (2019) "Subwavelength acoustic monopole source emission enhancement through dual gratings," *Scientific Reports*, **9**(1), p. 11659.

[135] Jia, Y., Y. Luo, D. Wu, Q. Wei, and X. Liu (2020) "Enhanced Low-Frequency Monopole and Dipole Acoustic Antennas Based on a Subwavelength Bianisotropic Structure," *Advanced Materials Technologies*, **5**(4), p. 1900970.

[136] Zhang, J., Y. Cheng, and X. Liu (2018) "Tunable directional subwavelength acoustic antenna based on Mie resonance," *Scientific reports*, **8**(1), p. 10049.

[137] Lei, Y., J. H. Wu, and S. Yang (2021) "Broadband monopole emission enhancement using a dual acoustic grating," *Physics Letters A*, **408**, p. 127486.

[138] Fan, X.-D., Y.-F. Zhu, B. Liang, J.-c. Cheng, and L. Zhang (2018) "Converting a monopole emission into a dipole using a subwavelength structure," *Physical Review Applied*, **9**(3), p. 034035.

[139] Rasmussen, C. and A. Alù (2021) "Non-Foster acoustic radiation from an active piezoelectric transducer," *Proceedings of the National Academy of Sciences*, **118**(30), p. e2024984118.

[140] Oishi, T., C. Zhao, and G. Rios (2020), "High compliance microspeakers for vibration mitigation in a personal audio device," US Patent 10,812,896.

[141] Bai, M. R. and C.-M. Huang (2009) "Expert diagnostic system for moving-coil loudspeakers using nonlinear modeling," *The Journal of the Acoustical Society of America*, **125**(2), pp. 819–830.

[142] Rothauser, E. (1969) "IEEE recommended practice for speech quality measurements," *IEEE Transactions on Audio and Electroacoustics*, **17**(3), pp. 225–246.

[143] Wheeler, W. E. (2016), "Dynamic acoustic waveguide," US Patent 9,432,764.

[144] Yang, D.-X., Z. Hu, H. Zhao, H.-F. Hu, Y.-Z. Sun, and B.-J. Hou (2015) "Through-metal-wall power delivery and data transmission for enclosed sensors: A review," *Sensors*, **15**(12), pp. 31581–31605.

[145] Awal, M. R., M. Jusoh, T. Sabapathy, M. R. Kamarudin, and R. A. Rahim (2016) "State-of-the-art developments of acoustic energy transfer," *International Journal of Antennas and Propagation*, **2016**.

[146] Roes, M. G., J. L. Duarte, M. A. Hendrix, and E. A. Lomonova (2012) "Acoustic energy transfer: A review," *IEEE Transactions on Industrial Electronics*, **60**(1), pp. 242–248.

[147] Sherrit, S., M. Badescu, X. Bao, Y. Bar-Cohen, and Z. Chang (2005) "Efficient electromechanical network model for wireless acoustic-electric feed-throughs," in *Smart Structures and Materials 2005: Smart Sensor Technology and Measurement Systems*, vol. 5758, SPIE, pp. 362–372.

[148] Sherrit, S., B. Doty, M. Badescu, X. Bao, Y. Bar-Cohen, J. Aldrich, and Z. Chang (2006) "Studies of acoustic-electric feed-throughs for power transmission through structures," in *Smart Structures and Materials 2006: Industrial and Commercial Applications of Smart Structures Technologies*, vol. 6171, SPIE, pp. 8–15.

[149] Fu, H., J. Rao, M. S. Harb, and S. Theodossiades (2021) "Ultrasonic wireless power links for battery-free condition monitoring in metallic enclosures," *Ultrasonics*, **114**, p. 106395.

[150] Sun, K., Y. Wu, F. Qian, H. Jung, S. Kaluvan, H. Huijin, C. Zhang, F. K. Reed, M. N. Ericson, H. Zhang, et al. (2022) "Self-powered Through-wall communication for dry cask storage monitoring," *Annals of Nuclear Energy*, **177**, p. 109306.

[151] Fleury, R. and A. Alù (2013) "Extraordinary sound transmission through density-near-zero ultranarrow channels," *Physical review letters*, **111**(5), p. 055501.

[152] Park, J. J., K. Lee, O. B. Wright, M. K. Jung, and S. H. Lee (2013) "Giant acoustic concentration by extraordinary transmission in zero-mass metamaterials," *Physical review letters*, **110**(24), p. 244302.

[153] Zhou, Y., M.-H. Lu, L. Feng, X. Ni, Y.-F. Chen, Y.-Y. Zhu, S.-N. Zhu, and N.-B. Ming (2010) "Acoustic surface evanescent wave and its dominant contribution to extraordinary acoustic transmission and collimation of sound," *Physical review letters*, **104**(16), p. 164301.

[154] Estrada, H., P. Candelas, A. Uris, F. Belmar, F. G. De Abajo, and F. Meseguer (2008) "Extraordinary sound screening in perforated plates," *Physical review letters*, **101**(8), p. 084302.

[155] Christensen, J., L. Martin-Moreno, and F. J. Garcia-Vidal (2008) "Theory of resonant acoustic transmission through subwavelength apertures," *Physical review letters*, **101**(1), p. 014301.

[156] Lu, M.-H., X.-K. Liu, L. Feng, J. Li, C.-P. Huang, Y.-F. Chen, Y.-Y. Zhu, S.-N. Zhu, and N.-B. Ming (2007) "Extraordinary acoustic transmission through a 1D grating with very narrow apertures," *Physical review letters*, **99**(17), p. 174301.

[157] Shen, C., J. Xu, N. X. Fang, and Y. Jing (2014) "Anisotropic complementary acoustic metamaterial for canceling out aberrating layers," *Physical Review X*, **4**(4), p. 041033.

[158] Craig, S. R., P. J. Welch, and C. Shi (2019) "Non-Hermitian complementary acoustic metamaterials for lossy barriers," *Applied Physics Letters*, **115**(5), p. 051903.

[159] Park, C. I., C. Piao, H. Lee, and Y. Y. Kim (2021) "Elastic complementary meta-layer for ultrasound penetration through solid/liquid/gas barriers," *International Journal of Mechanical Sciences*, **206**, p. 106619.

[160] Wang, J., F. Allein, N. Boechler, J. Friend, and O. Vazquez-Mena (2021) "Design and fabrication of negative-refractive-index metamaterial unit cells for near-megahertz enhanced acoustic transmission in biomedical ultrasound applications," *Physical Review Applied*, **15**(2), p. 024025.

[161] Li, L., Y. Diao, H. Wu, and W. Jiang (2022) "Complementary Acoustic Metamaterial for Penetrating Aberration Layers," *ACS Applied Materials & Interfaces*, **14**(25), pp. 28604–28614.

[162] Gao, H., Z. Gu, S. Liang, T. Liu, J. Zhu, and Z. Su (2022) "Enhancing ultrasound transmission and focusing through a stiff plate with inversely optimized auxiliary meta-lens," *Applied Physics Letters*, **120**(11), p. 111701.

[163] Assouar, B., M. Oudich, and X. Zhou (2016) "Acoustic metamaterials for sound mitigation," *Comptes Rendus Physique*, **17**(5), pp. 524–532.

[164] Oudich, M., X. Zhou, and M. Badreddine Assouar (2014) "General analytical approach for sound transmission loss analysis through a thick metamaterial plate," *Journal of Applied Physics*, **116**(19), p. 193509.

[165] Oudich, M., B. Djafari-Rouhani, Y. Pennec, M. B. Assouar, and B. Bonello (2014) "Negative effective mass density of acoustic metamaterial plate decorated with low frequency resonant pillars," *Journal of Applied Physics*, **116**(18), p. 184504.

[166] Oudich, M., Y. Li, B. M. Assouar, and Z. Hou (2010) "A sonic band gap based on the locally resonant phononic plates with stubs," *New Journal of Physics*, **12**(8), p. 083049.

[167] Ashby, M. F. (1989) "Overview No. 80: On the engineering properties of materials," *Acta metallurgica*, **37**(5), pp. 1273–1293.

[168] Kinsler, L. E., A. R. Frey, A. B. Coppens, and J. V. Sanders (2000) *Fundamentals of acoustics*, John wiley & sons.

[169] Agarwal, K., R. Jegadeesan, Y.-X. Guo, and N. V. Thakor (2017) "Wireless power transfer strategies for implantable bioelectronics," *IEEE reviews in biomedical engineering*, **10**, pp. 136–161.

[170] Qi, S., M. Oudich, Y. Li, and B. Assouar (2016) "Acoustic energy harvesting based on a planar acoustic metamaterial," *Applied Physics Letters*, **108**(26), p. 263501.

[171] Oudich, M. and Y. Li (2017) "Tunable sub-wavelength acoustic energy harvesting with a metamaterial plate," *Journal of Physics D: Applied Physics*, **50**(31), p. 315104.

[172] Jiang, L., Y. Yang, R. Chen, G. Lu, R. Li, J. Xing, K. K. Shung, M. S. Humayun, J. Zhu, Y. Chen, et al. (2019) "Ultrasound-induced wireless energy harvesting for potential retinal electrical stimulation application," *Advanced Functional Materials*, **29**(33), p. 1902522.

[173] Mak, H. Y., X. Zhang, Z. Dong, S. Miura, T. Iwata, and P. Sheng (2021) "Going beyond the causal limit in acoustic absorption," *Physical Review Applied*, **16**(4), p. 044062.

Vita

Jun Ji

Jun Ji is currently a Ph.D. candidate in the Graduate Program in Acoustics at Pennsylvania State University, where he is working with Dr. Yun Jing on acoustic metamaterials and acoustic metasurfaces. He received his B.Eng. in Energy and Power Engineering from Jiangsu University, China in 2018. During his Ph.D., he has published 8 articles in peer-reviewed scientific journals, including 4 first-author papers in journals such as Physical Review Applied, Advanced Materials Technologies, and the Journal of Acoustical Society of America.

List of publications: Bold author: self. "+": equal contributions. "*": corresponding authors.

- **Jun Ji**$^{+}$, Hyeonu Heo^{+}, Jiaxin Zhong^{+}, Mourad Oudich*, and Yun Jing*, "Metamaterial-enabled wireless and contactless ultrasonic power transfer and data transmission through a metallic wall," Physical Review Applied. 21 (1), 014059 (2024).
- **Jun Ji**, Chuming Zhao*, Frank Yao , Tetsuro Oishi, John Stewart, and Yun Jing, "Metamaterial-Augmented head-mounted audio module," Advanced Material Technology. 2300834 (2023).
- **Jun Ji**, Junfei Li, Steven A. Cummer and Yun Jing*, "Ultra-sparse near-perfect sound absorbers," J. Acoust. Soc. Am. Express Lett 3, 034001 (2023).
- **Jun Ji**$^{+}$, Dongting Li^{+}, Yong Li, and Yun Jing*, "Low-frequency broadband acoustic metasurface absorbing panels," Frontier in Mechanical Engineering. 6, 586249 (2020).
- **Jun Ji**$^{+}$, Xiuyuan Peng^{+}, Junfei Li*, Nikhil JRK Gerard, Hyeonu Heo, Steven A. Cummer, and Yun Jing*, "Chirality selective transmission of acoustic orbital angular momentum through lossy metasurfaces," In Preparation.
- Jiaxin Zhong^{+}, **Jun Ji**$^{+}$, and Yun Jing*, "Deep Sub-wavelength Remote Whispering Enabled by Local-nonlinear Interactions of Self-bending Acoustic Beams," In Preparation.
- Jiaxin Zhong^{+}, Chengbo Hu^{+}, Kangkang Wang, **Jun Ji**, Tao Zhuang, Haishan Zou, Jing Lu, Hyeonu Heo, Bin Liang*, Yun Jing*, and Jian-Chun Cheng* "Local-nonlinearity-enabled Deep Sub-diffraction Control of Acoustic Waves," Physical Review Letters. 131 (23), 234001 (2023).
- Dongyi Wang^{+}, Yuanchen Deng^{+}, **Jun Ji**, Mourad Oudich, Wladimir A. Benalcazar*, Guancong Ma*, and Yun Jing*, "Realization of a Z-classified chiral symmetric higher-order topological insulator in a coupling-inverted acoustic crystal," Physical Review Letters. 131 (14), 157201 (2023).
- Yuanchen Deng^{+}, Mourad Oudich^{+}, Nikhil JRK Gerard, **Jun Ji**, Minghui Lu, and Yun Jing*, "Magic-angle bilayer phononic graphene," Physical Review B. 102 (18), 180304 (2020).
- Xiuyuan Peng, **Jun Ji**, and Yun Jing*, "Composite honeycomb metasurface panel for broadband sound absorption," J. Acoust. Soc. Am. 144, EL255–EL261 (2018)